New Tools for Controlling Strontium Atoms with High Spectral and Spatial Resolution

Florian Wallner

München 2020

Neue Werkzeuge zur Kontrolle von Strontiumatomen mit Hoher Spektraler und Räumlicher Auflösung

Masterarbeit am Physik Department
Technische Universität München
Max Planck Institut für Quantenoptik

vorgelegt von

Florian Wallner

München, den 15. Dezember 2020

Erstgutachter: Prof. Frank Pollmann
Zweitgutachter: Prof. Immanuel Bloch
Weitere Prüfungskommissionsmitglieder: Dr. Sebastian Blatt

Zusammenfassung

In dieser Masterarbeit berichten wir über die Charakterizierung zweier Mikroskopobjektive für das Abbilden und Adressieren einzeln aufgelöster, ultrakalter Strontiumatome in optischen Gittern. Die Punktspreizfunktionen der Objektive werden für drei verschiedene Wellenlängen bei 461 nm, 689 nm und 698 nm bestimmt. Die gemessene Auflösung beider Objektive ist für alle Wellenlängen nahezu beugungslimitiert. Außerdem beschreiben wir eine Methode um interferometrisch die Verzerrung der Wellenfront durch ein Objektiv zu messen.
Für das einzeln aufgelöste Adressieren von Strontiumatomen auf dem extrem schmalen Uhrenübergang berichten wir über die Entwicklung un den Aufbau zweier Lasersysteme. Durch das Stabilisieren zweier Lasern auf zwei verschiedene optische Resonatoren mit hoher Finesse erreichen wir eine relative Linienbreite unter 4(1) Hz.

Abstract

In this thesis we report on the characterization of two microscope objectives for single-site imaging and addressing of ultracold strontium atoms in optical lattices. The point-spread functions of both objectives are measured for three different wavelengths at 461 nm, 689 nm and 698 nm. We found close to diffraction-limited resolution for all wavelengths for both objectives. Furthermore, we describe a method for interferometrically measuring the wavefront distortion induced by a microscope objective.
For single-site addressing of ultracold strontium atoms on the ultranarrow clock transition we designed and built two laser systems. By locking two lasers to two different high-finesse optical cavities we achieved a relative linewidth below 4(1) Hz.

Contents

1 Introduction **1**

2 Strontium Quantum Gas Microscope **3**
2.1 Strontium . . . 3
2.2 The Magic of Strontium . . . 4
2.3 Optical Lattices . . . 7
2.4 Optical Cavities . . . 8
2.5 Quantum Gas Microscopes . . . 10
2.6 Single-Site Addressing . . . 12

3 Ultra-Stable Laser System for Narrow-line Excitation **15**
3.1 Linear external cavity diode lasers . . . 15
3.2 Electronic Adapter Board . . . 17
3.3 Laser Characterization . . . 18
3.4 Optical Setup . . . 20
3.5 Ultralow Expansion Cavities . . . 22
3.6 Pound-Drever-Hall Lock . . . 23
3.7 Linewidth Measurement . . . 25
3.8 Injection Lock . . . 30
3.9 Outlook . . . 31

4 Optical Imaging Theory **33**
4.1 Point-Spread Function . . . 33
4.2 Depth of Focus . . . 37
4.3 Spatial Resolution Limits . . . 39
4.4 Optical Aberrations . . . 40
4.5 Outlook . . . 43

5 Microscope Objective Characterization **45**
5.1 The Objective . . . 45
5.2 Reflection and Transmission . . . 47
5.3 Characterization setup . . . 50
5.4 Point-Spread Functions . . . 52
5.5 Comparison . . . 55
5.6 Outlook . . . 56

6 Interferometric Characterization of Wavefront Distortion **59**
6.1 Interferometry . . . 59

6.2 Tuneable Coherence Length 60
6.3 Low NA Fizeau Interferometer 62
6.4 Microscope Interferometry 62
6.5 Phase Map and Objective Aberrations 65
6.6 Outlook 69

7 Conclusion and Outlook **71**

8 Appendix **73**

References **75**

Acknowledgements **81**

List of Tables

5.1 Reflection and Transmission of the objectives 50

List of Figures

2.1 Energy level structure of strontium . . . 4
2.2 Dipole trap and optical lattices . . . 5
2.3 Dynamic polarizability and state-dependent potentials . . . 6
2.4 Optical Cavities . . . 9
2.5 Science Cavity and Slicing . . . 10
2.6 Quantum Gas Microscope . . . 11
2.7 Single-site Addressing . . . 13

3.1 External Cavity Diode Laser . . . 16
3.2 Electronic adapter board . . . 18
3.3 Output power and mode profiles . . . 19
3.4 Mode hop-free tuning range . . . 20
3.5 Optical setup for the clock lasers . . . 21
3.6 ULE cavities . . . 22
3.7 PDH-locking scheme . . . 24
3.8 PDH-lock setup at cavity . . . 26
3.9 Linewidth measurement . . . 28
3.10 Drift measurement . . . 29
3.11 Injection lock . . . 30

4.1 Theoretical imaging system . . . 34
4.2 Radial point-spread function . . . 37
4.3 Axial point-spread function . . . 38
4.4 Resolution criteria . . . 39
4.5 PSF on lattice . . . 41
4.6 Optical aberrations . . . 42

5.1 Microscope Objective . . . 46
5.2 Specified point spread functions and focal shift . . . 47
5.3 Scratches and repaired objective . . . 48
5.4 Reflection and transmission setup . . . 49
5.5 Characterization setup . . . 51
5.6 Point-spread functions of objective I . . . 53
5.7 Point-spread functions of objective II . . . 54
5.8 Comparison of Quantum Gas Microscopes . . . 56

6.1 Interferometer . . . 60
6.2 Michelson interferometer . . . 61

6.3 Output power and Coherence length 63
6.4 Low NA test setup 64
6.5 Microscope interferometer 65
6.6 Phase map 66
6.7 Phase map cut 67

8.1 Adapter Board Circuit 73

Chapter 1

Introduction

SIMULATING the behavior of many quantum particles requires tremendous computational power on classical computers [1]. For a full simulation of these quantum systems it is essential to keep track of all *superpositions* in the system. To work around the intrinsic limitations of classical computers in performing these simulations, Richard Feynman proposed his famous idea of a *quantum simulator* [2]. His proposal was based on taking a well-controlled quantum system to simulate the essential ingredients of another quantum system. In the last 30 years since Feynman first presented his idea, many technical breakthroughs have been made and quantum simulators have been proposed to simulate problems in fields ranging from *high-T_c superconductivity* [3] to *quantum chemistry* [4].

Building a well-controlled quantum system is not a straightforward endeavor. The system needs to be well-isolated from the environment to preserve coherence and the simulation parameters need to be controlled. Nevertheless, in the last decades different candidates for a quantum simulator including *neutral cold atoms and molecules* [5], *trapped ions* [6], *nitrogen-vacancy centers in diamonds* [7], *photonic systems* [8], and *superconducting circuits* [9] have been developed. Key to all those systems is a precise control and read out of the quantum state of a large number of individual particles.

Cold neutral atoms are a strong candidate for a large scale quantum simulator [5]. They excel through high controllability of system parameters and scalability to multiple hundred particles [10]. With the invention of *quantum gas microscopes* a whole new set of tools for local control became available in neutral atom systems [11, 12]. In these microscopes a sample of multiple hundred ultracold atoms is held in a pattern of interfering laser beams, known as an *optical lattice*. Trapped at individual lattice sites, the atoms can be made to scatter laser light, which can then be collected in a high resolution imaging system to enable single-site-resolved imaging. This technique allows probing of correlation functions between individual particles, which can be used to characterize the underlying quantum state of the system [13]. Shortly after the first demonstration of imaging it became possible to address individual sites through the microscope, and to control the state of an individual quantum particle [14, 15].

Due to the favorable electronic structure of alkaline metals for laser cooling, most early neutral atom experiments were done with these elements [16]. However, a much richer internal structure can be found in *alkaline earth(-like)* atoms such as *strontium* and *ytterbium*. The two valence electrons in these atoms result in the formation of singlet and triplet states and extremely narrow optical transitions with milihertz linewidths [17].

This ultranarrow linewidth enables precise optical control and makes these transitions well suited for *quantum metrology*. Indeed, inspired by this electronic structure a new generation of *optical atomic clocks* was built, which can reach unprecedented precisions on the order of 10^{-18} over one hour of averaging time [18]. This precision is achieved by trapping a degenerate Fermi gas of ultracold strontium atoms in a 3D optical lattice and probing the system on the ultranarrow optical transition, called the *clock transition* [19].

In our experiment we aim to combine the unique detection and manipulation techniques offered by a quantum gas microscope with the high level of precision of optical atomic clocks. To realize this, we are building a *strontium quantum gas microscope* [20]. We will also explore state-dependent potentials, which can be realized for the clock states [21]. This state-dependent control was proposed to enable simulations of *nanophotonics* [22] and problems in *quantum chemistry* [4].
Due to the short lattice spacings that come with these state-dependent traps, harsh criteria are set on the resolution capabilities of the microscope objective for our quantum gas microscope. Furthermore, for coherent single-site addressing of multiple atoms on the clock transition, a flat wavefront in the focal plane is required. Otherwise atoms will dephase quickly and coherence is lost. Manipulating the extremely narrow clock transition on the single particle level already demands a special laser system. To coherently drive the atoms on the transition over several 100 ms the driving laser needs a linewidth on the Hz-level. As we will show, such a stability requires a well-isolated light source and locking the laser to a high finesse optical cavity.

In this work we present an ultrastable laser system for addressing strontium atoms on the extremely narrow clock transition. We designed and built a new laser that is well-isolated from environmental noise. For linewidth narrowing, two lasers are locked to two different high-finesse optical cavities. The resulting stability is analyzed with a heterodyne beat measurement. To enable single-site imaging and addressing in our quantum gas microscope we characterize two microscope objectives. The resolution capabilities of both objectives are compared with a point-like target source. In addition, we describe a method to measure the wavefront distortion induced by a high-resolution objective. This information can be used to manipulate the wavefront with adaptive optics and to achieve arbitrary single-site addressing of strontium atoms on the clock transition.

In Ch. 2 we give an overview of strontium and an introduction into quantum gas microscopy. We then move on to a description of our ultrastable laser system for driving the clock transition and discuss our results in Ch. 3. Having treated the laser component of this project, we focus on building a theoretical framework in Ch. 4 for analyzing the resolution of the microscope objectives. We follow with a report and a comparison of the experimentally measured resolution in Ch. 5. Finally in Ch. 6 we explain our method for determining the wavefront distortion induced by a microscope objective.

Chapter 2

Strontium Quantum Gas Microscope

In our experiment we aim to combine the benefits of the rich electronic structure of strontium with the possibility of detecting and manipulating individual trapped atoms. This new toolbox should enable a substantial increase in the control of many quantum particles and makes new types of *quantum simulation* possible [23]. The main experiment has evolved to a complex machine, since it was started five years ago. In the following we therefore only cover the essential parts for this thesis and refer the reader to Ref. [20] for a more detailed description of the setup.
In this chapter, we will at first focus on the detailed electronic structure of strontium. We discuss how the dipole force can be used to trap cold atoms. We will then see how state dependent potentials can be engineered by combining the electronic states with the dipole force. Further, we explain the working principle of optical lattices and optical cavities, before we continue with an introduction to quantum gas microscopes. Finally, we will focus on single-site addressing of strontium atoms in optical lattices.

2.1 Strontium

As an alkaline earth metal strontium has two valence electrons. These allow for the formation of singlet and triplet states as shown in Fig. 2.1. The resulting energy level structure offers multiple transitions with linewidths ranging from the MHz to the mHz regime.
The ground state for strontium is the $^1\mathrm{S}_0$ state [Fig. 2.1]. From there a broad blue transition connects to the $^1\mathrm{P}_0$ excited state with a linewidth of $\Gamma_{^1\mathrm{P}_1} = 2\pi \times 30.41(9)$ MHz [21]. The large momentum transfer on this transition makes it an ideal candidate for a first laser cooling stage or when high scattering rates are needed, e.g for imaging. Additionally, there exists another red $^1\mathrm{S}_0 \rightarrow {}^3\mathrm{P}_1$ transition coupling the singlet to the triplet states. Due to the dipole forbidden spin flip, necessary to reach the triplet, this transition has a narrow linewidth of $\Gamma_{^3\mathrm{P}_1} = 2\pi \times 7.423(7)$ kHz. This narrow linewidth makes it well-suited for a second laser cooling stage [32] and allows for highly efficient sideband cooling in deep optical traps [23]. The transition which caused a lot of excitement in the recent years is the doubly forbidden $^1\mathrm{S}_0 \rightarrow {}^3\mathrm{P}_0$ line [17]. Its natural linewidth was recently measured to be 1.35(3) mHz with an equivalent natural lifetime of $\tau = 118(3)$ s for the excited state [27]. The long atom-light coherence time on this transition makes it a primary candidate for building optical atomic clocks that can achieve record uncer-

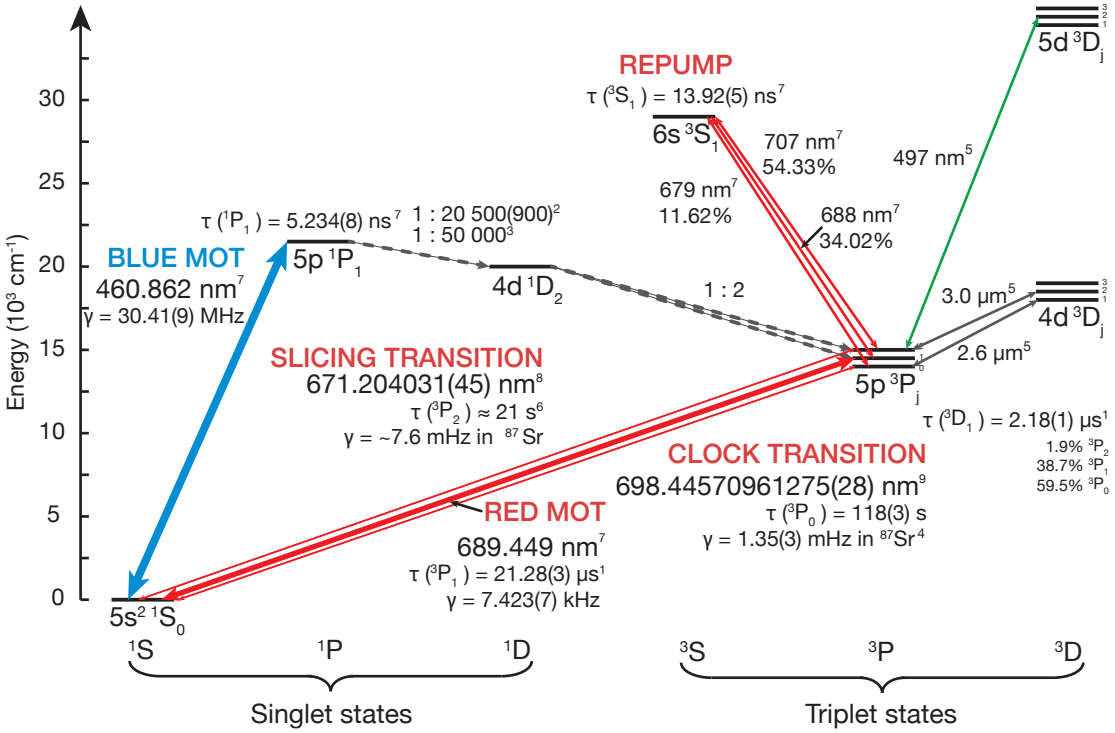

Fig. 2.1 Energy level structure of strontium. Relevant transitions for our experiment including lifetime and branching ratios. Data taken from Refs. [1][24] [2][25] [3][26] [4][27] [5][28] [6][29] [7][20] [8][30] [9][31].

tainties of 2.0×10^{-18} [18]. For this reason, the transition is called the *clock transition*. It is in principle doubly forbidden and is only possible due to hyperfine mixing of $^1\mathrm{P}_1$ into the pure $^3\mathrm{P}_0$ state [33]. Therefore, the transition requires a net nuclear spin and is consequently only possible in fermionic ^{87}Sr. In the bosonic isotopes, e.g. ^{88}Sr, it can be induced by applying a very strong magnetic field [23]. There exists another similar doubly forbidden transition to the $^3\mathrm{P}_2$ state, which in comparison to the clock transition is $\sim 10^4$ times more sensitive to magnetic fields. Thus, it can be manipulated much more easily. This excited state has a lifetime of ~ 21 s in ^{87}Sr [34] while it can persist for several minutes in ^{88}Sr [29].

2.2 The Magic of Strontium

To explain how optical beams can trap atoms we have to take a closer look at the light-matter interactions. The induced dipole moment $\mathbf{d}(\mathbf{r}, t)$ experienced by an atom at position $\mathbf{r}$ and time t due to an external electric field $\mathbf{E}(\mathbf{r}, t)$ can be expressed as [35]

$$\mathbf{d}(\mathbf{r}, t) = \alpha(\omega)\, \mathbf{E}(\mathbf{r}, t), \tag{2.1}$$

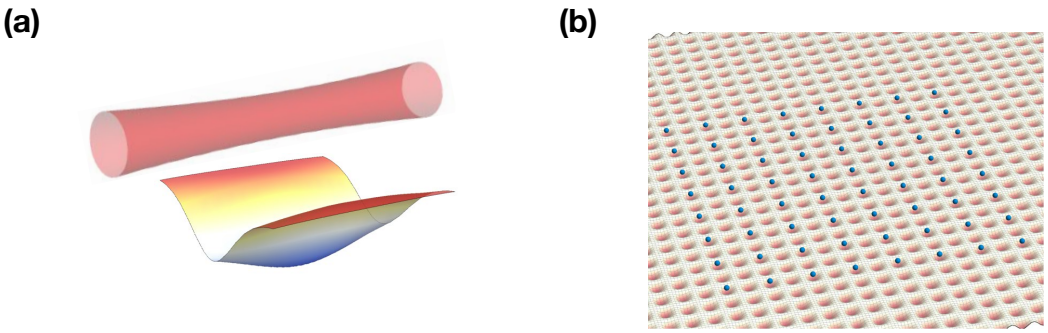

Fig. 2.2 Dipole trap and optical lattices. (a) A Gaussian beam with the resulting Gaussian trapping potential is shown. **(b)** A 2D plane of a 3D optical lattice is displayed. For very shallow lattice depths atoms can freely tunnel. In a deep potential the atoms are localized at a specific lattice site.

where $\alpha(\omega)$ is the dynamic dipole polarizability. Here, $\omega = 2\pi c/\lambda$ stands for the angular optical frequency with the speed of light c and the wavelength λ of the light [36]. In a Lorentz-oscillator model, $\alpha(\omega)$ is calculated from a semi-classical approach. This method takes all transitions j into account, that are reachable from the initial state k with linewidth Γ_{jk}. By introducing the Einstein coefficients $A_j = 1/\tau_j$, determined form the lifetime τ_j of the corresponding state with transition frequency ω_j, we find [36]

$$\alpha_k(\omega) = 6\pi\epsilon_0 c^3 \sum_j \frac{\Gamma_{jk}}{\omega_j^2(\omega_j^2 - \omega^2 - iA_j\frac{\omega^3}{\omega_j^2})}. \tag{2.2}$$

Here, ϵ_0 is the vacuum permittivity. A much more sophisticated calculation for the $^1\mathrm{S}_0 = |g\rangle$ ground and the $^3\mathrm{P}_0 = |e\rangle$ clock state in ^{87}Sr is depicted in Fig. 2.3 (a). Time-averaging over the induced dipole moment $\mathbf{d}(\mathbf{r},t)$ and the electric field $\mathbf{E}(\mathbf{r},t)$ gives the resulting trapping potential [36]

$$V_{\mathrm{dip}}(\mathbf{r}) = -\frac{1}{2}\langle \mathbf{d}(\mathbf{r},t)\mathbf{E}(\mathbf{r},t)\rangle = -\frac{1}{2\epsilon_0 c}\mathrm{Re}[\alpha(\omega)]I(\mathbf{r}). \tag{2.3}$$

We see, that the depth of the trapping potential is given by the real part of $\alpha(\omega)$ and the intensity profile of the electric field $I(\mathbf{r})$. Laser beams typically have a Gaussian intensity profile of the form

$$I(r,z) = I_0 \frac{1}{1+\left(\frac{z}{z_R}\right)^2} \exp\left(-\frac{2r^2}{w_0^2\left(1+\left(\frac{z}{z_R}\right)^2\right)}\right) \tag{2.4}$$

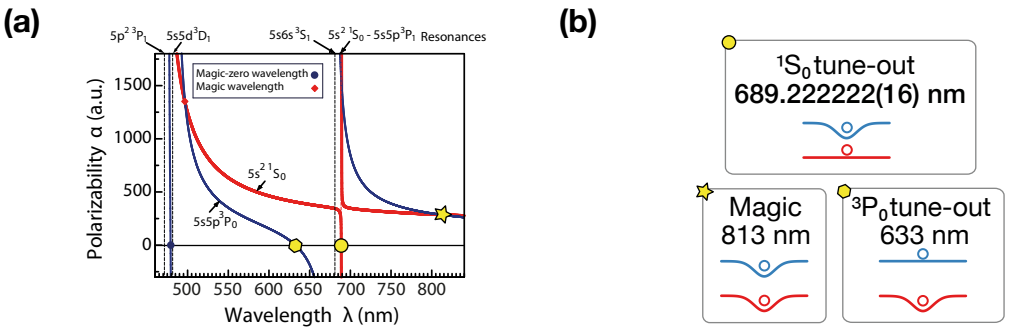

Fig. 2.3 Dynamic polarizability and state-dependent potentials. (a) Atomic structure calculation for $^1\mathrm{S}_0$ and $^3\mathrm{P}_0$ states in Strontium. Taken from Ref. [35]. **(a)** At the magic-wavelength both states experience a similar potential. The tune-out wavelengths enable full differential control of different electronic states. Adapted from [21].

with $I_0 = \frac{1}{2}cn\epsilon_0|E_0|^2$ and $z_R = \frac{\pi w_0^2}{\lambda}$. Here, n stands for the refractive index and w_0 for the waist of the beam at the focus. The expression is formulated in terms of the radial coordinate r and the positioning along the optical axis z. This intensity profile results in the same Gaussian shape for the trapping potential [Fig. 2.2(a)].
Since the polarizability $\alpha(\omega)$ is state- and wavelength-dependent, Eq. (2.3) also indicates a strong dependence of the trap depth on these parameters. It turns out that by choosing an appropriate wavelength for the trapping laser one can engineer the trap depth of these potentials for one specific electronic state relative to another state.

At first this behavior was explored in the context of optical lattice clocks to first order eliminate the frequency shift induced by the trapping light on the clock transition [37]. This is achieved by choosing a wavelength for the trap where the $|g\rangle$ and $|e\rangle$ states have the same polarizability. The optical trap will then shift both states by exactly the same amount and leave the frequency difference between both states unchanged. For the strontium $^1\mathrm{S}_0 \rightarrow {}^3\mathrm{P}_0$ transition one of these so called *magic-wavelengths* lies at 813 nm [Fig. 2.3]. This magic condition can also be found for the $^1\mathrm{S}_0 \rightarrow {}^3\mathrm{P}_1$ line at 914 nm [35]. Another interesting wavelengths are so-called *tuneout-wavelengths* [Fig. 2.3 (b)]. At these particular wavelengths the dynamic polarizability for one state vanishes, which in turn means the state hardly sees any potential [20]. Around 633 nm, only the $|g\rangle$ state experiences a confinement, while the $|e\rangle$ state is unaffected [35]. The opposite situation occurs close to the red $^1\mathrm{S}_0 \rightarrow {}^3\mathrm{P}_1$ transition. The ground state tuneout-wavelength at 689.222222(16) nm for strontium was measured in our experiment for the first time with modulation spectroscopy [21].

2.3 Optical Lattices

For trapping atoms we can not only use a single beam but can also make use of interference patterns formed by multiple laser beams to create *optical lattices*. In the simplest case, a laser is retro reflected by a mirror, forming a standing wave. This realizes a periodic potential of the form

$$V(z) = -\frac{1}{2\epsilon_0}\mathrm{Re}\left[\alpha(\omega)\right] I(z) = -V_x \cos^2(kz), \tag{2.5}$$

in one spatial dimension (1D). Here, $k = 2\pi/\lambda$ stands for the wave vector of the trapping light. Since the potential is conservative we can add the 1D expressions to arrive at the 3D potential when laser beams are interfered from all three axes

$$V_{3\mathrm{D}}(\mathbf{r}) = V(x) + V(y) + V(z) = -\left[V_x \cos^2(kx) + V_y \cos^2(ky) + V_z \cos^2(kz)\right]. \tag{2.6}$$

For a 2D cut through the 3D potential the shape of the potential is illustrated in Fig. 2.2(b). Atoms, when loaded into these optical lattice can now fill the individual potential valleys, known as *lattice sites*. If, on the one hand the potentials are very deep, the atoms are located at one particular site [Fig. 2.2(b)]. On the other hand, if we have shallow potentials atoms can tunnel from one lattice site to another and therefore move around in the optical lattice. This behavior can be exploited for quantum simulations, since the potential the atoms see exhibits close similarities to the potentials electrons feel in solid state matter [16].
In general the laser beams that create the optical lattice, similar to the dipole trap, also have a Gaussian intensity profile. This additional Gaussian envelope alters the potentials in Eq. (2.5) and Eq. (2.6). The final potential is then

$$V(r,z) = -V_z \cos^2(kz) \exp\left(-\frac{2(x^2+y^2)}{w_0^2}\right) \tag{2.7}$$

in one spatial dimension. We see, that the Gaussian profile results in an additional bending on the optical lattice potential. This phenomena is known as *harmonic confinement* [36]. It is responsible for the maximum extent a system can have without occupation of lattice sites by two atoms. At a certain radius away from the potential center, the Gaussian envelope increases the potential energy so much that it is energetically more favorable for the system to put two atoms on the central site rather than occupying the outer sites. To keep the influence of the Gaussian envelope on the potential as low as possible it is necessary to use laser beams with high intensities over a large radial extent. It turns out, that requires beams with high optical power and a large waist. Consequently, Eq (2.6) is only valid in the center of large laser beam.
Typical maximal trap depths for optical lattices lie in the low 100 μK regime. Consequently it is necessary to laser cool the atoms before they are loaded in the lattice. In Ref. [20] the reader finds a detailed explanation on how the cooling can be realized for strontium atoms.

2.4 Optical Cavities

Another important ingredient for our experiment and in particular for this thesis are *optical cavities*. These resonators consist of a pair of highly reflective mirrors attached to an ultra-low expansion (ULE) glass spacer. Therefore we refer to the resonator as a ULE cavity. This special glass ensures a minimal length change between the mirrors.
To understand the properties of such a resonator we start with the solution of an electric field inside an 1D optical cavity given by [38]

$$E(r, k_q) = E(t)\sin(k_q r), \tag{2.8}$$

where k_q can take the values

$$k_q = \frac{\pi q}{L}, \tag{2.9}$$

in terms of an integer parameter q and the cavity length L. With the linear dispersion relation of the electric field $E(t)$ in vacuum $\nu = ck/(2\pi)$ one can derive an expression for the different resonator frequencies

$$\nu_q = q\frac{c}{2L} = q\,\nu_{\mathrm{FSR}}. \tag{2.10}$$

We see, that all resonator modes are spaced by the same frequency known as the *free spectral range* (FSR) of the cavity [Fig. 2.4(b)] [38]. Another key value for the characterization of optical resonators is the *finesse* F. It is a measure of how many times a photon can bounce between the mirrors before is is lost from the cavity. By introducing R for the intensity reflectivity of the mirrors, the finesse is

$$F = \frac{\pi\sqrt{R}}{1-R}. \tag{2.11}$$

Very high F leads to narrowing of the different cavity modes. The linewidth $\Delta\nu_{\mathrm{FWHM}}$ (full width at half maximum) of these frequency teeth can be expressed, in the regime where $F \gg 1$, as [38]

$$\Delta\nu_{\mathrm{FWHM}} \approx \frac{\nu_{\mathrm{FSR}}}{F}. \tag{2.12}$$

For finding the light intensity inside the cavity, we can approximate the resonator as a plane-parallel *Fabry-Pérot interferometer* [Fig. 2.4(a)]. The two mirrors are separated by a distance L. Each of them has a reflectivity $R_1 = R_2 = R$ and a transmission $T_1 = T_2 = T$. From one side we couple an electric field $E(r, \nu)$ into the resonator. The field propagates to the other mirror where part of the light E_{out} is transmitted with ratio T while most of the light is reflected back to the original mirror at ratio R. This process of traveling back and forth then repeats until a steady state between the reflected and transmitted light is reached. We can then obtain the intensity inside the resonator by summing up all the

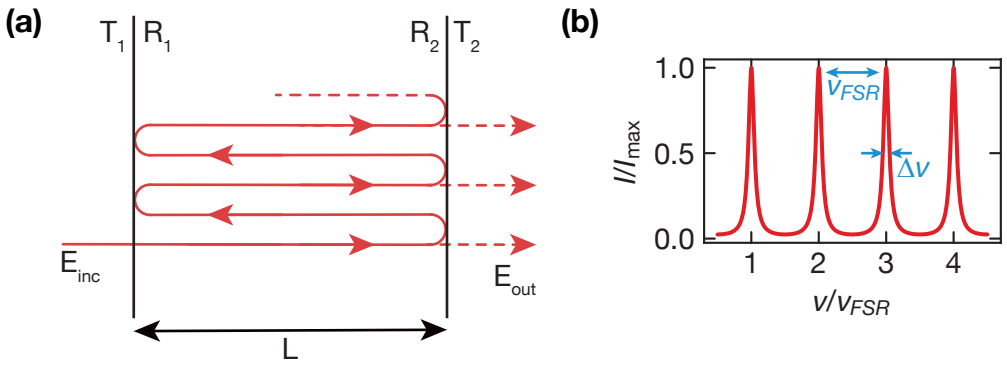

Fig. 2.4 Optical Cavities. (a) A Fabry-Pérot inferferometer. Two plane-parallel mirrors with reflectivity R_1 and R_2 and transmission T_1 and T_2 are separated by a distance L. Light is coupled into the resonator and reflected back and forth many times. At each round trip part of the light is transmitted. **(b)** Transmission spectrum of the different cavity modes. For all resonators the modes are spaced by one free spectral range (FSR). Each mode has a linewidth $\Delta\nu = \nu_{\mathrm{FSR}}/F$. The figure was taken from Ref. [39].

electric fields from the different reflections inside the cavity as [38]

$$I(\nu) = \frac{I_{\max}}{1 + (2F/\pi)^2 \sin^2(\pi\nu/\nu_{\mathrm{FSR}})}. \tag{2.13}$$

Here $I_{\max}$ stands for the maximum intensity coupled into the cavity on resonance. Furthermore, wee see that through the many round trips an electric field can be drastically amplified inside a resonator.

In our experiment we take advantage of this light amplification. As we have seen early, to suppress the harmonic confinement induced by the Gaussian beam shape as much as possible, laser beams with high power and large waists are necessary. For that reason, we amplify the lattice light with an optical cavity in our experiment [20]. The resonator also defines a large mode waist of $\sim$400 μm. In the experiment the cold atoms are loaded into two crossed optical modes formed inside a monolithic cavity. A picture of this in-vacuum resonator can be seen in Fig. 2.5(a).
With the cavity we expect to increase the particle number of the quantum simulation from multiple 100 [10] to multiple 10000. We expect a system size of roughly 200$\times$200 single-occupied sites [20].
The light amplification can also be used to generate lattice at interesting wavelengths where only little laser power is available. For example, we can create a tuneout-lattice, where only one of the clock states is trapped.

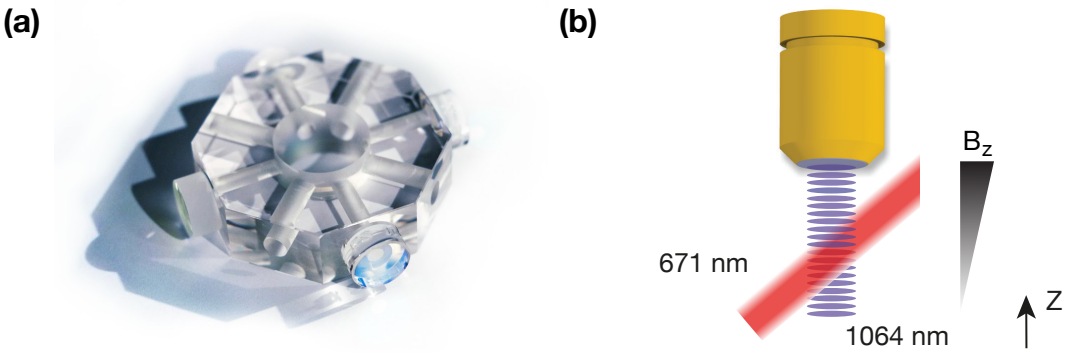

Fig. 2.5 Science Cavity and Slicing. (a) The crossed optical science cavity. Four mirrors are optically contacted to the ULE glass to minimize mode displacement and ensure maximum stability [20]. **(b)** An optical lattice retro reflected from the front surface of the objective. The 671 nm laser addresses individual layers, shifted by a magnetic field gradient, to depopulate them.

2.5 Quantum Gas Microscopes

A major game changer for quantum simulation with ultracold atoms in optical lattices was the invention of *quantum gas microscopes* [12, 11]. This technique enables a whole new way for detection and manipulation of individual particles.
The simplified working principle of such a quantum gas microscope is as follows: For every experimental run, a sample of ultracold atoms is loaded into a 3D optical lattice. Then, a 2D layer of the lattice is isolated. After that, the real physics experiment starts by decreasing the lattice depth to allow the atoms to tunnel between sites in the 2D plane. The prepared quantum state evolves over a certain time before the motion is frozen out by increasing the lattice depth again. To now measure the occupation of each lattice site, a fluorescence beam is applied. The atoms scatter photons, which are collected with a high resolution objective and are then directed onto a camera [Fig. 2.6(a)]. Since the atoms experience a recoil kick when scattering photons, they can be heated up to a point where they can tunnel again. To prevent this unwanted tunneling, additional cooling during imaging is required. In Fig. 2.6(b), a typical image of single-site resolved atoms provided by our lithium-team can be seen. Each red dot in this picture correspondents to an individual lithium atom.

The constraints set by our system differ from most quantum gas microscopes. The science cavity inside our main vacuum chamber limits the optical access we have to the atoms. Therefore, typical isolation techniques for single layer preparation do not work. Common methods like *accordion lattices* or z-lattices with large spacings need substantial optical access to the atoms, which is not possible in our setup [12, 41, 42]. In the second technique, for example, two laser beams are interfered under a small angle along the z-axis. This creates a lattice with spacing $d = \lambda/(2\sin\theta)$, where θ is the angle between the two beams. If the angle is sufficiently small the lattice spacing can be on the order of

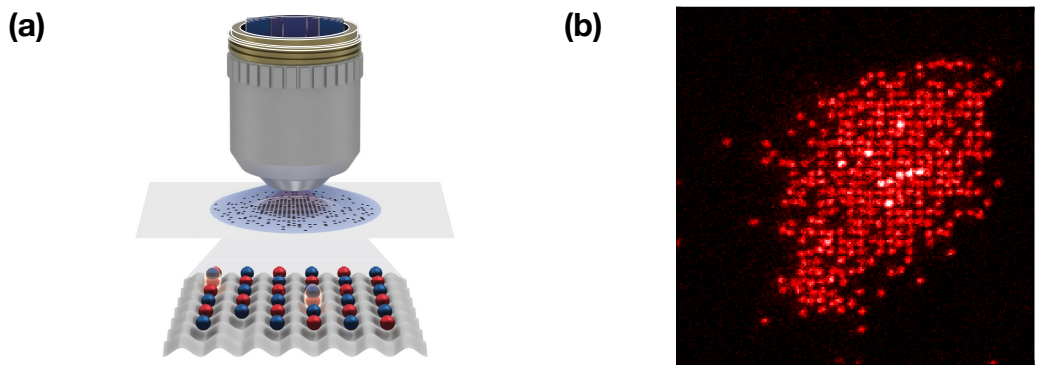

Fig. 2.6 Quantum Gas Microscope. (a) The occupation of each individual lattice site can be measured with a high resolution imaging system [40]. **(b)** Typical fluorescence picture of the atoms in the optical lattice. Unpublished image provided by our lithium team showing a single-site resolved, fermionic, lithium Mott-insulator.

a few μm. The shift between neighboring layers is then enough to only have one of the layers in the focus of the microscope.
Since isolation a 2D layer is essential to decrease possible background noise from neighboring layers during imaging, we plan to adapt a different method, that was already demonstrated in an ytterbium quantum gas microscope [43]. In this ytterbium experiment only a 1D optical lattice together with a strong magnetic field gradient was turned on along the z-direction [Fig. 2.6(b)]. The gradient shifts the optical transitions of each layer. With a laser for the $^1\mathrm{S}_0 \rightarrow {}^3\mathrm{P}_2$ transition each layer, except the desired one, is then excited to the $^3\mathrm{P}_2$ state by varying the frequency of the laser to be resonant with one layer at a time. Strong inelastic two-body collisions in this $^3\mathrm{P}_2$ state then depopulate the plane.
For the $^3\mathrm{P}_2$ state the linear Zeeman splitting in strontium is $\Delta_{\mathrm{Zeeman}} = 0.5$ MHz/G [30]. Since we can calculate the frequency splitting with $\Delta f = \Delta_{\mathrm{Zeeman}} \cdot m_f \cdot B$, the largest splitting is achieved for the transition between the $^1\mathrm{S}_0(m_F = 9/2) \rightarrow {}^3\mathrm{P}_2(m_F = 11/2)$ hyperfine states m_F. Our gradient coils can provide a maximum of $\frac{dB}{dz} = 1.09$ G/(cm A) at the location of the atoms. This is essentially limited by our vacuum chamber, because it is not possible to mount the coils closer to the atoms. For technical reasons we can also not send more than 300 A through the coils. Therefore, for a lattice spacing of 532 nm along the z-direction we calculate a maximum splitting of 36.5 kHz between the layers. To repeatably isolate the same layer and to be immune against small drifts the linewidth of the excitation laser needs to be roughly two orders of magnitude smaller than the splitting. This leaves us with a very narrow linewidth on the order of 365 Hz. This high demand on the stability of the laser sets additional technical challenges for our experiment. In Ch. 3 we describe in detail how such a narrow laser can be constructed.
Furthermore, the science cavity sets another limitation to our quantum gas microscope. To contact mirrors to its sides, the cavity spacer needs a certain height [20]. This extent limits the closest distance we can achieve between the microscope objective and the

atoms to $\sim$13.6 mm which limits the NA.
The z-component of our optical lattice will be made by retro reflecting a high power laser beam at 1064 nm from the front surface of the microscope. Thus, our objective is fabricated with a highly reflective coating for the infrared region of the optical spectrum on the first lens. In this setup the z-lattice is referenced to the microscope objective. Since horizontal drifting of the microscope objective will result in the same drifting on the horizontal lattice planes differential drifts should be minimized and the isolated layer should stay in the focus of the microscope.
As mentioned earlier, we expect our cavity to increase the system size to 200×200 sites. Resolving all these lattice sites sets harsh criteria on the objective. In a lattice with wavelength 914 nm, the field of view needs to be 100 μm to imagine all sites. The resolution quality also needs to be very high over the whole area. Ch. 5 and Ch. 6 are therefore dedicated to a detailed characterization of the microscope objective we plan to use.
We plan to image the strontium atoms on the broad blue $^1\mathrm{S}_0 \rightarrow {}^1\mathrm{P}_1$ transition. This has two advantages. First, as we will explain in detail in Ch. 4, the short wavelength of 461 nm naturally offers a very high resolution, decreasing the number of photons we need to distinguish between different lattice sites. Second, the 4000 times higher scattering rate compared to the $^1\mathrm{S}_0 \rightarrow {}^3\mathrm{P}_1$ transition results in a fast production of many fluorescence photons, reducing the imaging duration significantly. These two advantages are accompanied by a large recoil kick for each scattering event. To prevent the atoms from tunneling in the optical lattice we will use additional cooling on the narrow red $^1\mathrm{S}_0 \rightarrow {}^3\mathrm{P}_1$ transition. Since the 7.4 kHz linewidth of this transition is below typical motional excitations in a deep optical lattice we can perform efficient direct sideband cooling on the red transition [23]. Using an optical lattice at the magic wavelength of 914 nm makes this cooling method for the cooling transition even more efficient.
Once the microscope is installed many new detection possibilities emerge. First of all we could probe correlation functions to reveal hidden order in quantum phases [44, 45]. As a second tool, one can map spin or the unique electronic degrees of freedom of alkaline earth atoms onto the occupation of lattice sites to also detect ordering in these parameters [46, 47].

2.6 Single-Site Addressing

We can not only use the microscope for imaging, but also for addressing individual atoms [14]. By focusing a beam through the objective all of the light can be concentrated onto a single lattice site [Fig. 2.7(a)]. This would drastically enhance the toolbox for our platform, since most experiments to date still rely on global control of parameters only [5]. With single-site addressing a large number of new initial states for our quantum simulator could be prepared [23].
In combination with a spatial light modulator, that enables full control over the wavefront of light, we could do holographic beam shaping for our addressing laser [15, 48]. With this tool light can be focused to an arbitrary lattice site. Figure 2.7(c) shows, how this

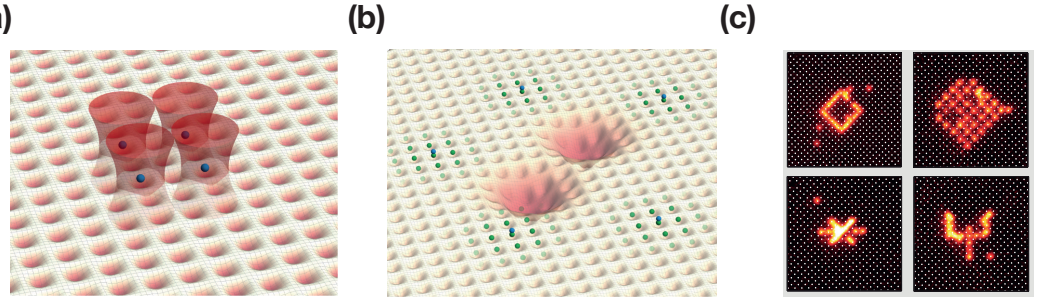

Fig. 2.7 Single-site Addressing. (a) With single-site addressing the electronic state of individual atoms can be controlled. **(b)** It is also possible to project additional potentials on top of the optical lattice. **(c)** This technique allows to cut out arbitrary shapes form a atomic Mott-insulator [14].

method can be used to cut out a predefined structure from atoms trapped in an optical lattice [14]. With this high level of control over the light field, additional potentials could also be placed on top of the optical lattice [Fig. 2.7(b)].
For alkaline earth atoms it could be very interesting to control the clock states on individual sites. Each atom can them be interpreted as an optical qubit with individual manipulation and readout. In combination with the huge system size this could dramatically increase the number of qubits, that can be individually controlled. Consequently, this technique could bring quantum gas microscopes one step closer to a *digital quantum simulator*.
Direct addressing of individual lattice sites also offers more flexibility than previous addressing techniques. In Ref. [14] a local light shift was used to shift one lattice on resonance with a global microwave field. This is enough to drive multiple atoms on a specific transition, but it is not possible to induce predefined phase shift between then. With an arbitrary control of the phase and amplitude of the driving field in the focal plane of the microscope offered by spatial light modulator the strength and the phase of the driving can be adjusted on each lattice site. The substantial increase in control with this technique was proposed to enable quantum simulations of *nano-photonics* and *quantum chemistry* problems [22, 4].

Chapter 3

Ultra-Stable Laser System for Narrow-line Excitation

To drive the ultra-narrow clock transition we require a laser with similarly narrow linewidth. Unfortunately, building a system that can provide a light wave with frequency stability of 1 mHz is technologically still out of reach. The best laser to date has a linewidth on the order of 10 mHz and a coherence time of 55 s between atoms and the laser has been demonstrated [49]. This was achieved with a complex setup involving multiple steps of stabilization for the laser including a cryogenic environment [50]. All of these breakthroughs were made in the context of strontium optical lattice clocks [18]. In contrast, our quantum simulator only requires atom-light coherence times of several 100 ms. For this reason we only need a laser with a linewidth on the order of 10 Hz.
In this chapter we report on the design and construction of a new laser system for the $^1\mathrm{S}_0 \rightarrow {}^3\mathrm{P}_0$ clock transition at 698 nm and the $^1\mathrm{S}_0 \rightarrow {}^3\mathrm{P}_2$ transition at 671 nm, with which we plan to isolate a single optical lattice plane. After a detailed description of the lasers and the accompanying optical setups, we give a brief introduction to the Pound-Drever-Hall scheme. We use this technique to stabilize two independent clock lasers to two different optical cavities. The relative linewidth of both lasers is characterized with a heterodyne beat measurement. In addition we report on an injection lock setup for high optical output power at the clock wavelength.

3.1 Linear external cavity diode lasers

Achieving a very narrow linewidth requires precise engineering of the whole setup from the beginning. Any external noise will eventually disturb the system and increase the laser linewidth. We therefore designed a new laser housing for our linear laser design [51], to achieve a better isolation from external noise sources.
The housing prevents pressure fluctuations from reaching the laser cavity. A change in pressure changes the refractive index of the air. This variation modifies the effective cavity length resulting in a frequency change of the laser. The housing also acts as a *Faraday cage*. The current for the laser diode is therefore shielded from radio-frequency signals in the lab. These signals can modulate the laser current and disturb the output frequency of the light.
The laser housing is made from aluminum and has approximately 10 mm thick walls. It consists of a lid and a bottom plate [Fig. 3.1(a,b)]. With a Viton ring in between the two parts, the box can be made air-tight when screwed together. For the laser output beam

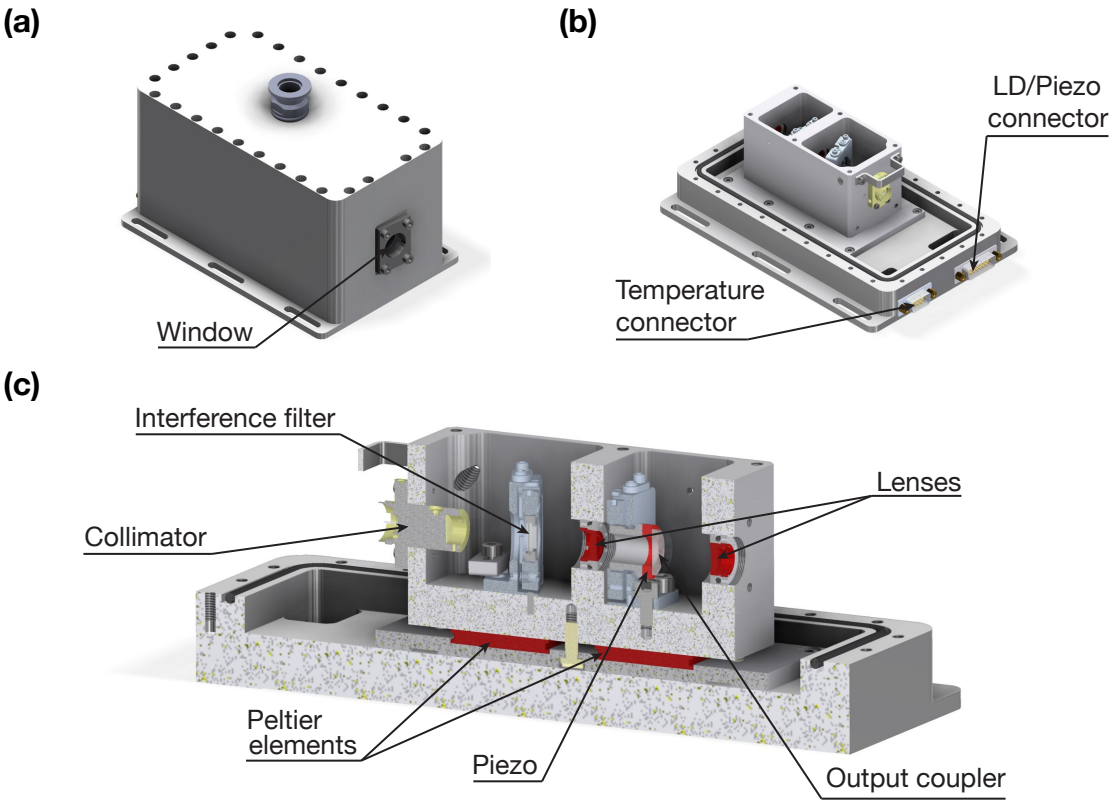

Fig. 3.1 External Cavity Diode Laser. (a) An assembled laser housing with a window for the output beam.**(b)** The laser housing has two connectors, one for the laser diode current and the piezo crystal, and the other for temperature control. **(c)** The laser body rests on two Peltier elements for temperature control. A collimator electrically isolates the diode and collimates the output beam. With the interference filter a first frequency selection is done. The laser diode together with the output coupler forms the external cavity. The length of this cavity can be tuned with the piezo ring. The first lens focuses the beam on the output coupler, while the second lens collimates the final beam.

an additional wedged window is placed at the front of the lid [Fig. 3.1(a)]. On the back end of the bottom plate two connectors are attached [Fig. 3.1(b)]. The left connector allows for controlling the temperature inside the housing. Two Peltier elements can heat and cool the inside, while a thermistor gives feedback on the actual temperature. The right connector is for a piezo voltage and the current for the laser diode. Looking at the housing from the back and counting from the upper left to the right pins 4 and 11 are used for the piezo crystal and pins 7,8 for the laser diode [Fig. 3.2(a)]. The pins 3, 5, 10 and 12 are for shielding the laser current from the high piezo voltage. Behind the two connectors on the inside we placed two pockets. After connecting all necessary cables to the connectors we sealed the pockets with *Torr Seal* glue making it air-tight. To prevent any cables form outgassing, we used *Kapton* insulated cables exclusively on the inside.

The laser body is made from a single aluminum block to ensure maximum stability [Fig. 3.1(c)]. It rests on the two Peltier elements and is connected to the bottom plate with 5 nylon screws. On the back end the collimator (*Schäfter+Kirchhoff 20C-A4.5-07*) with the laser diode is mounted. The collimation tube isolates the diode electrically and collimates the output beam. For the clock laser at 698 nm we use a laser diode from *Sacher* (*SAL-0705-020*). The laser for the $^1\mathrm{S}_0 \rightarrow {}^3\mathrm{P}_2$ transition at 671 nm is built with a diode from *Eagleyard Photonics* (EYP-RWE-0670-00703-1000-SOT02-0000). Both laser diodes are anti-reflection coated. This coating suppresses the formation of a cavity between the gain medium and the diode window. Otherwise the external and internal cavity can compete, reducing the frequency stability of the laser. For monitoring the temperature we installed a thermistor close to the collimator. The first optical element in the beam path is an interference filter. This filter enables a first rough frequency adjustment of the laser light. The next element that the beam passes is a lens. It focuses the light onto the output coupler. This coupler is a partially transmissive mirror. It reflects 30 % of the light back into the laser diode forming the external cavity. To modulate the cavity length the output coupler is glued to a piezo ring. The last element in the laser body is a second lens, which collimates the final output beam.
Since the laser body design is very similar to an older version we refer the reader to Ref. [51] for a detailed explanation on how to build such a laser.
The linear external cavity design has a couple of advantages over other laser designs. The simple linear configuration overall reduces the effects of cavity length variations. Any motion that is orthogonal to the optical axis of the cavity will not change the cavity length. The linear lasers also exhibit large tuning ranges, due to the decoupling of the wavelength selection from the optical feedback into the laser diode. The cavity length can be varied without changing the optical feedback. In contrast, in a Littman design the zeroth order of a diffraction grating is used as the feedback, while the first order is the output beam. To tune the laser wavelength the angle of the grating needs to be modified. This also changes the angle of the zeroth order resulting in a reduced optical feedback.

3.2 Electronic Adapter Board

The electronic control for all lasers described in this chapter is done with an analog rack from *Toptica* (*DC 110 19"*). The LD current and the piezo voltage are not directly fed into the housing but are sent through a custom adapter board [Fig. 3.2(a)]. The main purpose of the additional electronic board is to filter and monitor the laser diode current. Possible noise on the current will be directly modulated onto the laser light, which results in an increase of the linewidth. Different electronic components in the circuit can be exchanged to suppress or filter noise depending on the needs of the experiment.
For direct modulation of the laser diode current the board has an additional modulation circuit. This circuit can be necessary if the feedback signal from the lock picks up additional noise in the controller and consequently must be sent directly to the laser diode.
We also paid close attention in the layout to ground paths. These paths are separated as

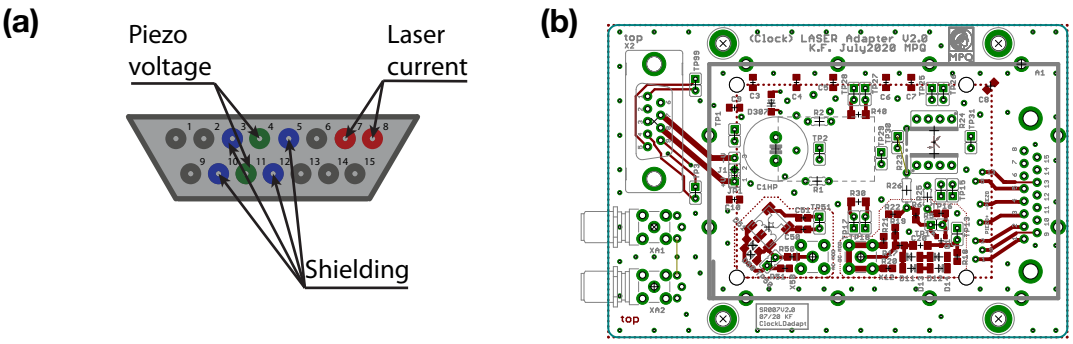

Fig. 3.2 Electronic adapter board. (a) We designed the sub D-15 pin connector, such that the laser diode current is shielded from the high piezo voltage. **(b)** Design layout for the adapter board.

much as possible to prevent unwanted galvanic coupling of ground loop currents.
The high voltage to drive the piezo crystal is sent through the same sub-D connector as the diode current. To avoid any cross talk, we keep both signals spatially separated on the board. The four pins surrounding the piezo voltage pins create a shielding cage throughout the connector. To achieve an even better shielding form radio-frequencies we designed a thin metal case around the board.

3.3 Laser Characterization

Before the construction of all necessary optical systems the properties of the laser need to be known. We characterized the output power of the 698 nm and 671 nm laser after placing an isolator with $\sim$ 91 % transmission in the beam path. The clock laser starts lasing when 24 mA are applied to the laser diode [Fig. 3.3(a)]. At the lasing threshold the light amplification in the laser diode starts to balance the losses in the external cavity and the laser starts to lase. We achieve a maximum optical output power of 37 mW at a limiting current of 90 mA. Several mode hops can be seen in Fig. 3.3(a). These jumps in power happen when the gain in the laser cavity is high enough to favor not only one but multiple modes. The laser can then jump from one lasing mode to another resulting in a frequency jump of the output light. For a stable operation the laser should run at currents where no mode hop is near by. Due to long-term thermal drifts these points can change. Therefore, an adjustment of the current over longer time scales is necessary. The 671 nm laser has a lasing threshold at 58 mA and we reach a maximum output of 35 mW at a current of 100 mA [Fig. 3.3(b)]. A clear jump in output power can be seen when the laser diode starts lasing. We find a 10 mW higher output power than specified by the company at the maximum current.

A close to Gaussian mode profile of the output light is essential for efficient fiber coupling of the laser light. Further, a mode with high aspect ratio will likely clip at optical

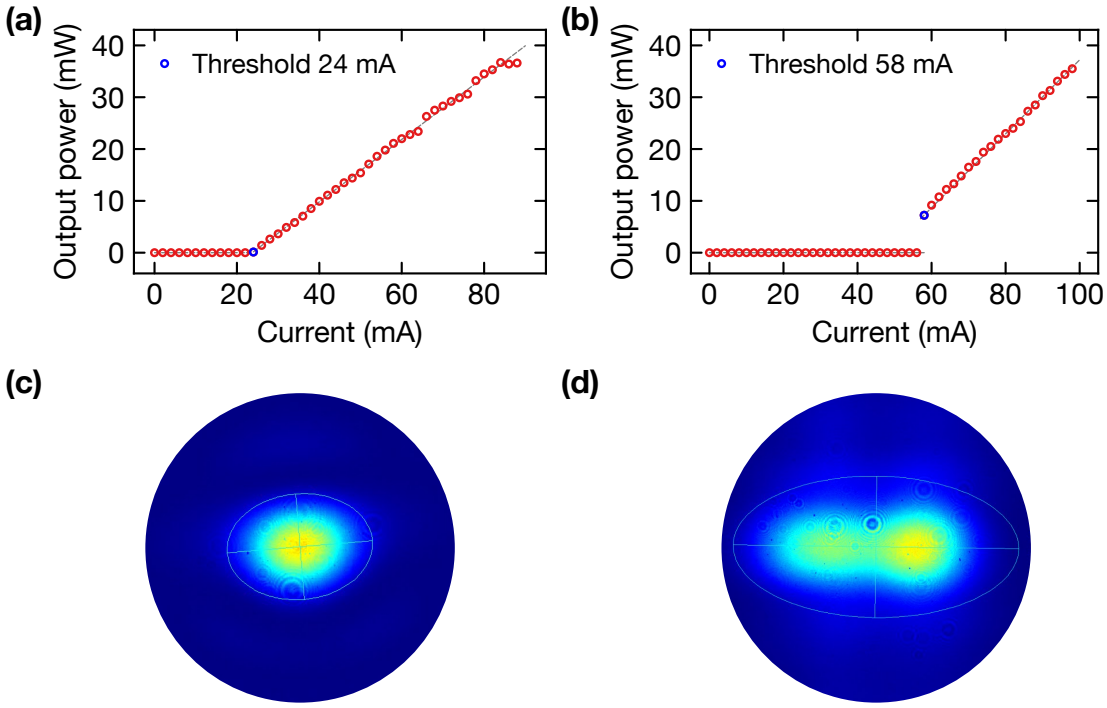

Fig. 3.3 Output power and mode profiles. (a) Output power for the clock laser. It starts lasing at 24 mA and reaches a maximum output of $\sim$ 37 mW. Additional mode hops can be seen. **(b)** Output power for the slicing laser. The sharp lasing point is at 58 mA and reaches a maximum power of $\sim$ 35 mW **(c)** Close to Gaussian mode profile for the clock laser with aspect ratio 1.22 **(d)** Double Gaussian structure of the 671 nm laser mode with aspect ratio 2.02.

elements and pick up unnecessary aberrations. Therefore, we characterized the mode profile roughly 1.5 m after the laser head for both lasers. For the clock laser we find an aspect ratio of 1.22 (1.61/1.32 mm) for the $1/e^2$ diameter of the laser output mode [Fig. 3.3(c)]. This was sufficient to couple approximately 65-70 % of the power into an optical fiber, without clipping on other optical elements in the setup.
Engineering gain materials for laser diodes at 671 nm is still challenging, since this wavelength differs considerably from the band gap of the semiconducting GaAs used as the gain medium [52]. To overcome this challenge, different compositions with other elements such as aluminum are used. It turns out that growing these compositions on a substrate with very high quality is demanding. The result of this imperfect material manufacturing is a distortion of the mode shape. Therefore the emitted mode at 671 nm can not be approximated by a Gaussian. In our case we observed a shape that can be described by two Gaussian modes aligned next to each other [Fig.3.3(d)]. Although we managed to couple 40-50 % of the original output power into an optical fiber, with an aspect ratio of 2.02 (4.30/2.13 mm) for the $1/e^2$ diameter we can not ensure that the beam is not clipping at an optical element in the setup. A cylindrical telescope should

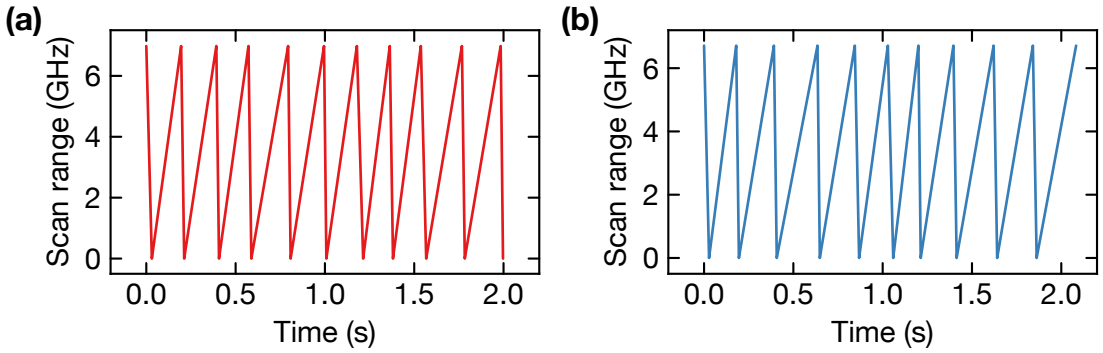

Fig. 3.4 Mode hop-free tuning range. (a) Typical scanning spectrum for the clock laser with a mode hop-free tuning range of 6.98 GHz. **(b)** Scanning plot for the slicing laser at 671 nm with a mode hop-free tuning range of 6.81 GHz.

therefore be installed after the laser housing to reduce the eccentricity significantly. Besides the laser diode, the interference filter and the actual lens in the collimator could also contribute to the mode shape. Their small size could already clip the mode profile. Further investigation is needed on this issue. One should also measure the mode profile at multiple distances after the housing to ensure a continuously Gaussian mode shape.
In experiments it is often required to ramp or modulate the laser frequency. This so called *scanning* of the laser is used e.g. to find atomic resonances. The necessary frequency change of the laser is achieved by varying the length of the external cavity. For that purpose the output coupler is glued to the piezo ring. The crystal responds to different input voltages with a length change subsequently modifying the cavity extent and the laser frequency. A large change in resonator length typically favors lasing of a different mode. Hence, we can define a maximum scanning range over which we can tune the cavity length without observing a mode hop. This is known as the *mode hop free tuning range*. Figure 3.4 shows a typical spectrum of such a scan for the 698 nm [Fig. 3.4(a)] and for the 671 nm laser [Fig. 3.4(b)]. We achieve a maximum mode hop free tuning range of 6.97 GHz at 698 nm. For the 671 nm laser a tuning range without mode hops of 6.81 GHz is measured.

3.4 Optical Setup

To use the laser light in the experiment, it needs to be controlled in all of its aspects. Several beam splitters for monitoring and locking have to be included. Furthermore, the laser light has to be frequency-shifted to the exact frequency of the atoms. We start with the explanation of the optical setup for our *Toptica DLC Pro* clock laser and follow with our homebuilt laser. Both lasers are placed on one breadboard to ensure maximum stability and avoid differential drifts.
The *Toptica* laser already has an internal isolator to protect the diode from possible dam-

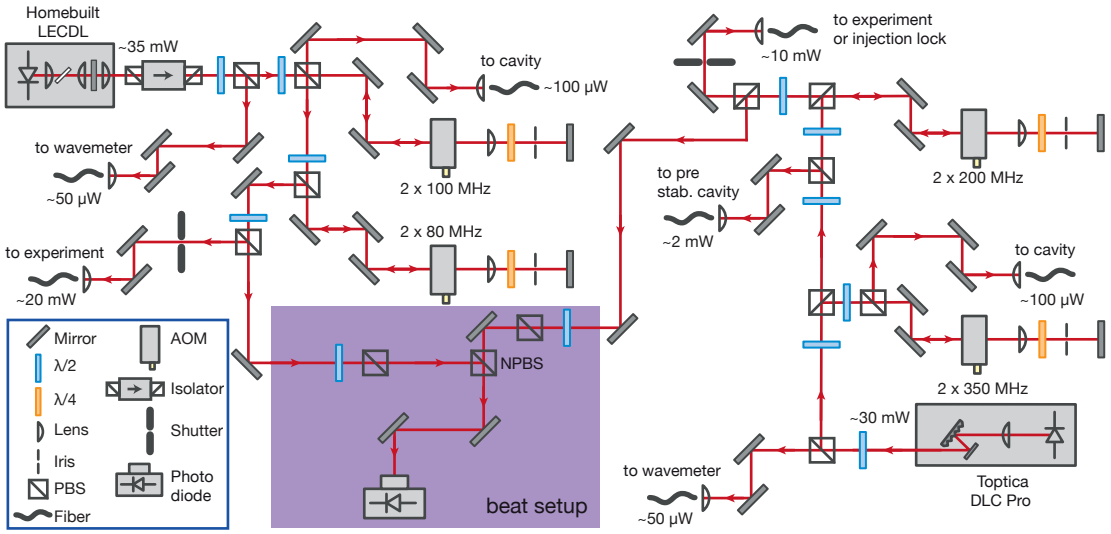

Fig. 3.5 Optical setup for the clock lasers. The *Toptica* and the homebuilt laser are frequency-shifted to the actual clock transition. Additional beam splitters for monitoring the frequency and locking to the cavity are installed. A beat measurement can been done on the bread-board without extra fiber links.

age due to back reflections. We also measured a close-to-Gaussian mode profile and therefore decided to dispense with a cylindrical telescope. The optical output power directly after the laser head is $\sim$ 30 mW. At first, we split off a minor part of the output using a polarizing beam splitter (PBS) and a $\lambda/2$-waveplate and guide $\sim$ 50 μW through an optical fiber for our wavemeter for continuous monitoring of the laser frequency. A second beam splitter directs part of the light into a double-pass acousto-optical modulator (AOM) [53] to shift the laser frequency by $\sim$2$\times$350 MHz. This shifted light is then fiber-coupled to a reference cavity (cavity II). From the remaining light another $\sim$ 2 mW beam is taken to stabilize the length of a transfer cavity for a titanium-sapphire laser in our lab. Next in line is a second double-pass AOM to shift the light by $\sim$2$\times$100 MHz. This modulator is primarily for intensity and frequency control on the main experiment, while the first 350 MHz AOM is responsible for compensating drifts of the cavity and the laser. Another 10 mW of the remaining light is then directed into a fiber port to the main experiment or to an injection lock setup. An additional mechanical shutter can completely block the light to reduce any possible light leakage to the experiment. We split off another 2 mW for a beat measurement with the other laser.
Our homebuilt laser has no internal isolation. For that reason, an optical isolator is placed directly after the housing. From the starting power of $\sim$35 mW we also guide $\sim$ 50 μW to an optical fiber to our wavemeter for monitoring the frequency. Splitting off part of the light and directing it through a double-pass AOM shifts it by $\sim 2 \times 100$ MHz. It is then fiber-coupled to our second reference cavity (cavity I). The rest of the light is, similar to the other setup, shifted with a second double-pass AOM configuration by $\sim 2 \times 80$ MHz. Afterwards it is directed through a shutter into an optical fiber to the main experiment.

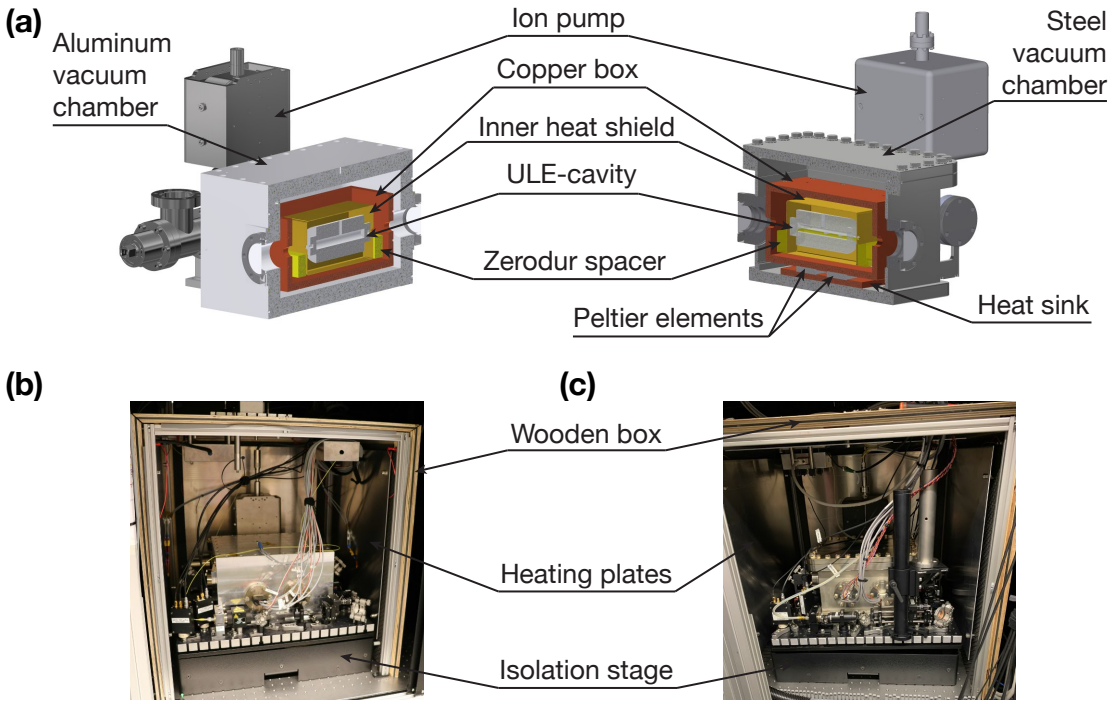

Fig. 3.6 ULE cavities. (a) Both cavities are surrounded with multiple isolation and heat shields. The inside is stabilized to the zero crossing temperature of the ULE spacer. Additional ion pumps provide a high vacuum. **(b)** Picture of cavity I placed on the vibrations isolation platform inside the wooden box. The picture is taken from [39]. **(c)** Cavity II on its vibration isolation stage inside the actively temperature stabilized wooden box.

An additional ~ 2 mW beam is also guided to the beat setup.

3.5 Ultralow Expansion Cavities

To achieve a linewidth on the Hz-scale, it is necessary to stabilize the laser frequency to an ultra stable cavity and to narrow the linewidth. This is the so called locking of the laser.
For our two ULE cavities we measured a finesse of $F \approx 280000$ at 698 nm. We obtained this value with ringdown measurements [54]. The FSR for both resonators is 1.3 GHz, resulting in a cavity linewidth of $\Delta\nu_{\mathrm{FWHM}} \approx 5$ kHz.
The construction of the cavities was the project of previous master students. Thus, we only cover the essential details here and refer the reader to Ref. [54] for the assembly of cavity I and to Ref. [39] for cavity II.
The main purpose of the cavity housing is to isolate the ULE spacer from any thermal fluctuations in the environment and to keep the inside as close as possible to the zero

crossing temperature, where the ultralow expansion glass has a minimal length change. For that reason the actual resonator is placed in vacuum on a zerodur spacer with viton pads in between [Fig. 3.6(a)]. The whole apparatus is surrounded by an inner heat shield followed by a cooper box to ensure maximum heat damping in the outer region. In addition, our new design of cavity II features two Peltier elements at the bottom connecting the copper box to a heat sink. This design enables precise stabilization of the inside to the actual zero crossing temperature at $32.75°\text{C} \pm 1°\text{C}$ for cavity spacer II [39]. Multiple thermistors throughout the box give feedback on the actual temperature distribution in the box. Unfortunately, our old design of cavity I includes heaters that may outgas, resulting in a pressure increase. Additional vacuum leakage problems with the aluminum housing of cavity I led us to use a stainless steel box for the new resonator II. In total we can reach a pressure as low as 2.1×10^{-8} mbar for the new and only 1.6×10^{-6} mbar for the old design, provided through an ion pump. By mounting everything on an isolation platform, mechanical vibrations can be largely damped [Fig. 3.6(b-c)]. A wooden box with acoustic rubber plates and heating shields surrounds the whole cavity setup. This box ensures extra suppression of environmental noise and an active homogeneous temperature stabilization around the cavity housing. In Fig. 3.6(b), a picture of the open wooden box for cavity I and in Fig. 3.6(c) for cavity II can be seen.
With all this shielding and isolation it is ensured, that the cavity length and therefore the resonance frequency is only minimally affected by day-to-day noise sources and temperature changes caused by opening the lab door or the enclosure around the optical table.

3.6 Pound-Drever-Hall Lock

The laser light, guided to the optical cavities, needs to be stabilized to the cavity resonance. For that purpose we use a *Pound-Drever-Hall* (PDH) scheme [55]. For an extensive discussion of PDH-locks we refer the reader to Ref. [55]. In the following we only cover the essential features and focus on the actual implementation on our resonators.
In Fig. 3.7 a setup of all optical and electrical components necessary for a PDH-lock can be seen. At first a laser emits light at a specific frequency ω. This light is then sent through an electro-optic modulator (EOM), where it is phase-modulated at a frequency Ω. This results in two *sidebands* at $\omega \pm \Omega$ besides the *carrier* at ω in the frequency domain. The next optical elements in the beam path are a polarizing beam splitter and a $\lambda/4$-waveplate. Afterwards, the light is coupled into the optical cavity. It is essential, that the optical resonator will only transmit light on the cavity resonance and reflects all other parts of the frequency spectrum including the sidebands. Since the backreflection passes the $\lambda/4$-waveplate twice it exhibits an orthogonal polarization to the input beam and is therefore reflected from the PBS and directed onto a photodetector. With the detector the AC-component of the signal can be measured. One finds the two sidebands at frequency Ω. If the modulation frequency of the EOM Ω is now high enough compared to the cavity linewidth $\Delta\nu_{\text{FWHM}}$ (for our cavities $\Delta\nu_{\text{FWHM}} \approx 5$ kHz) the sidebands are fully reflected. Then we demodulate the photo detector signal in a mixer with frequency Ω of the side-

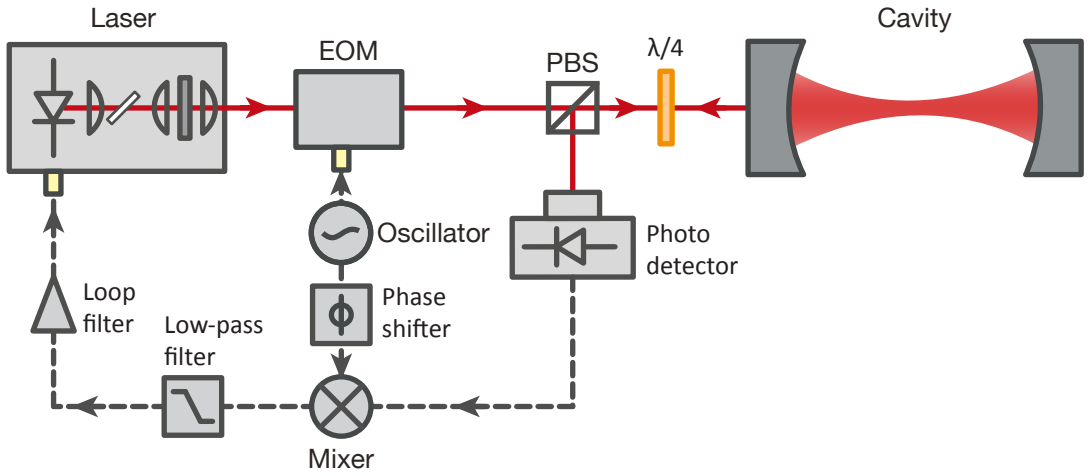

Fig. 3.7 PDH-locking scheme. An EOM modulates sidebands on the light before it is coupled to the cavity. With a PBS and a $\lambda/4$-waveplate the reflection from the cavity is measured with a photodiode. By mixing the reflection signal with the sideband frequency an error signal is generated. The final loop filter generates feedback for the diode current to stabilize the laser on the cavity.

bands. After low-pass filtering the characteristic error signal emerges [55]. It essentially depicts the deviation of the laser frequency ω from the cavity resonance $\Delta\nu_{\mathrm{FWHM}}$. Close to the cavity resonance this error signal has a linear frequency dependence and vanishes exactly on resonance. Now we can feed this signal into the loop filter, which calculates the necessary response on the laser diode current to counteract the change and stabilize the laser on the cavity resonance, and to narrow its linewidth.
In our experiment, the optical setup for both ULE cavities is essentially the same [Fig. 3.8]. The housings are mounted on a breadboard and placed on the vibration isolation stage [Fig. 3.6(c,d)]. This leaves some space around the housing to place all the optics necessary for a PDH-lock. We start by guiding the light that is fiber coupled to the cavity setup through a fiber electro-optical modulator (EOM) (Jenoptik PM705). The EOM modulates the required sidebands for the lock on the laser at a frequency of 23.777 MHz (23.771 MHz) for the Toptica (Homebuilt laser) (amplitude of 15 dBm). After that, the second fiber guides the light to the cavity setup, where it is collimated with a first lens. A telescope shapes the mode size to exactly match the one of the cavity. To prevent any backreflections from additional cavities in the beam path, the two lenses are slightly angled and an additional isolator is placed in front of the telescope (for clarity not included in Fig. 3.8). We achieve a transmission of 10 % of the input power through the cavity. To cavity II we lock not only our clock laser, but also our red MOT laser at 689 nm. Both lasers are sent from opposite sides into the resonator [Fig. 3.8]. Therefore it is necessary to split reflection and transmission signals for the different wavelengths on each side using special long- and short-pass filters.
To generate an error signal the AC-outputs of the reflection PDs are mixed with the local oscillator signal driving the fiber EOM. The mixed error signal is then sent through the

loop filter (*Toptica FALC 110*).
Achieving a very narrow linewidth requires precise optimization of the whole setup. To suppress fluctuations of the cavity length due to thermal expansion caused by the high light amplification in the resonator we decreased the optical power in front of the cavity to only $\sim 20\ \mu$W. Furthermore, we connect all electronics devices including the power supplies for the photodiodes to the same AC phase. This avoids any ground loops, which would result in electronic noise, that is then modulated onto the laser.

3.7 Linewidth Measurement

To determine the linewidth of the two locked lasers we perform a heterodyne beat measurement. A beat measurement consists of mixing light from two different lasers of the same frequency. The interference signal can then be detected on a photodiode. With this measurement we can set an upper bound for the linewidth of both lasers.
Mathematically, we can model the light from both lasers as plane waves and express them as

$$\begin{aligned} E_1(\mathbf{r},t) &= E_0 \exp[i(\mathbf{k}\cdot\mathbf{r} - \omega_1 t + \phi_1)]\mathbf{e}_1 \\ E_2(\mathbf{r},t) &= E_0 \exp[i(\mathbf{k}\cdot\mathbf{r} - \omega_2 t + \phi_2)]\mathbf{e}_2. \end{aligned} \tag{3.1}$$

Here E_0 is the amplitude, ω_i the angular light frequency, ϕ_i the phase and $\mathbf{e}_i$ the polarization vector for each laser. Summing and taking the square gives us the familiar intensity pattern of two interfering plane waves:

$$I(\mathbf{r},t) \propto \mid E_1(\mathbf{r},t) + E_2(\mathbf{r},t) \mid^2 = 2\left[E_0^2 + E_0^2 \cos\left((\omega_1 - \omega_2)t - \phi_1 - \phi_2\right)\right], \tag{3.2}$$

known as the beat signal. Since both lasers in general exhibit a Lorentzian line shape this implies that the combined signal is the convolution of the two Lorentzians. For the beat signal we then find again a Lorentzian line shape. In real systems external noise for example from pressure fluctuations in the air, is unavoidable. We therefore also have a Gaussian contribution to the overall laser shape. The final line shape then becomes a Voigt profile [56].
One of the major advantages of our system is a beating setup directly on the breadboard [Fig. 3.5] of the two lasers. There is no need for additional sending of light through an optical fiber, in which the laser linewidth through acoustic or thermal fluctuations can be broadened to the kHz regime [57]. For beating, both lasers are polarization-cleaned with a PBS and $\lambda/2$-waveplate. Then, we combine ~ 2 mW from each laser on a high-bandwidth photo detector (*Newport 818-BB-45*) using a non-polarizing beam splitter. On a spectrum analyzer we observe a beat signal at ∼2.5 GHz. Figure 3.9(a) shows a typical spectrum of the beat. We almost reach 40 dB suppression between the beat peak and the next highest feature in the spectrum. For an exact measurement of the linewidth, 10 spectra with a resolution bandwidth (RBW) of 1 Hz at a span of 1 kHz and a correspond-

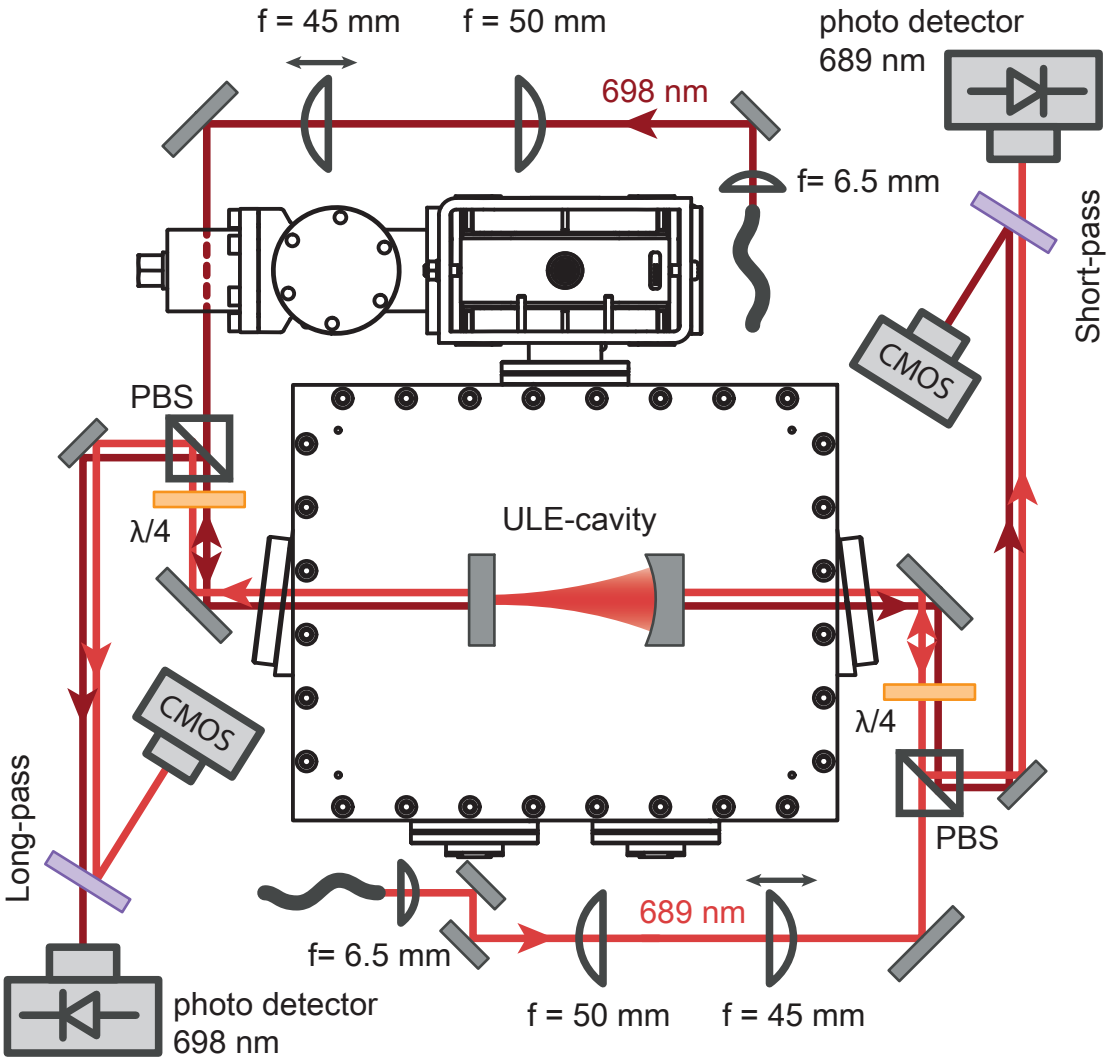

Fig. 3.8 PDH-lock setup at cavity. Optical setup of the Pound-Drever-Hall locks. In addition to the clock laser a red MOT master laser is locked to the ULE cavity. The different wavelengths are split with long- and short pass filters. Four PDs continuously monitor the transmission and reflection of each laser.

ing sweep time of 6 s are taken. We computed the FWHM of the central peak in each spectrum. The results are displayed in the inset in Fig. 3.9(a). From this measurement, we obtain a linewidth of 4(1) Hz for the beat note.
Since the RBW of our spectrum analyzer and the beat signal are of the same magnitude it limits the accuracy of our measurement. Fitting a Voigt profile to the beat note was not successful. For an improved measurement, we resolved the beat signal in the time domain. For that, we at first amplified the signal from the photo diode with two low noise amplifiers (*ZFL-1000LN (+15 dB)*) and mixed it down (*Mixer ZWL 34*) to $10-15$ Hz with a highly stable frequency generator. The resulting sine wave is observed on an oscilloscope [Fig. 3.9(b)]. Noise in the lab, like closing of the optical table, can now be observed as disturbance of the sine wave.
By fitting a regular sine to the data points we observe that the underlying signal stays in phase with an unperturbed sine wave for up to 4 s. We conclude from this, that our lasers can provide a stable wave over multiple seconds, which supports a linewidth smaller than the $4(1)$ Hz we obtained earlier by a direct heterodyne beat measurement. A limitation through the 1 Hz RBW of the spectrum analyzer in the beat setup is therefore very convincing. An additional fit to the data with a chirped sine wave reveals an oscillation frequency drift of 0.05 Hz/s.
Typical free running solid state lasers without further stabilization exhibit a linewidth on the order of 1 MHz. With our cavity lock the linewidth is narrowed down to the Hz-level. This yields a million-fold improvement on the stability of the laser.
An earlier beat measurement between two lasers locked each to one of the ULE cavities revealed a linewidth of 0.17(8) kHz [39]. To narrow the linewidth we made substantial improvements to this old setup. First of all, we used light at 698 nm not 689 nm like in the old measurement. The finesse is $\sim$5 % higher for both cavities at the clock wavelength. Therefore also the cavity linewidth at 698 nm is narrower. In the old setup the laser housing was not closed. Hence, environmental noise could also disturb the laser. In contrast, we used an air-tight 10 mm thick aluminum housing to isolate the laser from pressure fluctuations or radio-frequency noise. Moreover, a second wooden box was constructed around cavity II to reduce temperature fluctuations. For both lasers, we optimized the transmission signal to 10 %. In the earlier measurement only 5 % for the second cavity were achieved. Also the mentioned decrease of optical power sent to the cavities, to decouple the reflection signal from intensity fluctuations in the laser, contributed to the narrower linewidth. With a beat measurement on the laser breadboard to sidestep fiber noise sources we measure a factor of $\sim$45 decrease in laser linewidth.

Typical experiments in our lab are repeated multiple times. Therefore long-term changes of the apparatus need to be known exactly. To investigate the long-term behavior of the lasers and the locks we analyze the frequency drifts over multiple hours. The frequency change of the clock laser beat is displayed in Fig. 3.9(a). In the inset, a frequency measurement every minute for ten minutes is shown. From a fit we obtain a first order drift of -23.58 Hz/min and a second order drift of -0.64 Hz/s^2. Fig. 3.9(a) also shows a drift measurement over 6 h, with an average frequency drift of -1424 Hz/h and an associated

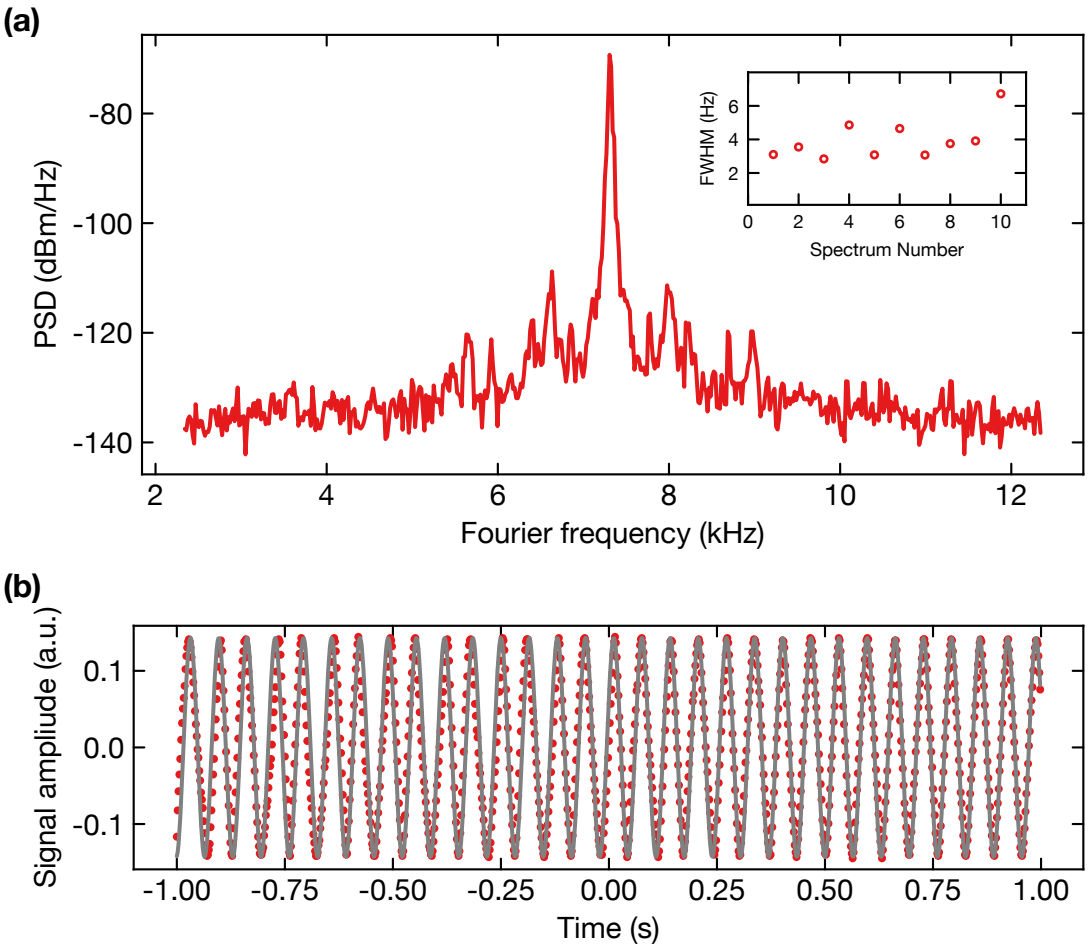

Fig. 3.9 Linewidth measurement. (a) A spectrum of the beat note. We reach up to 40 dB suppression between the beat note and next highest feature. The inset shows the resulting FWHM of the beat from 10 spectra taken with a RBW of 1 Hz and a span of 1 kHz with a sweep time of 6 s. We compute a resulting linewidth of 4(1) Hz. **(b)** Time-resolved measurement of the beat signal with pure sinusoidal fit. The laser can provide a coherent wave for multiple seconds indicating a laser linewidth lower than 4(1) Hz.

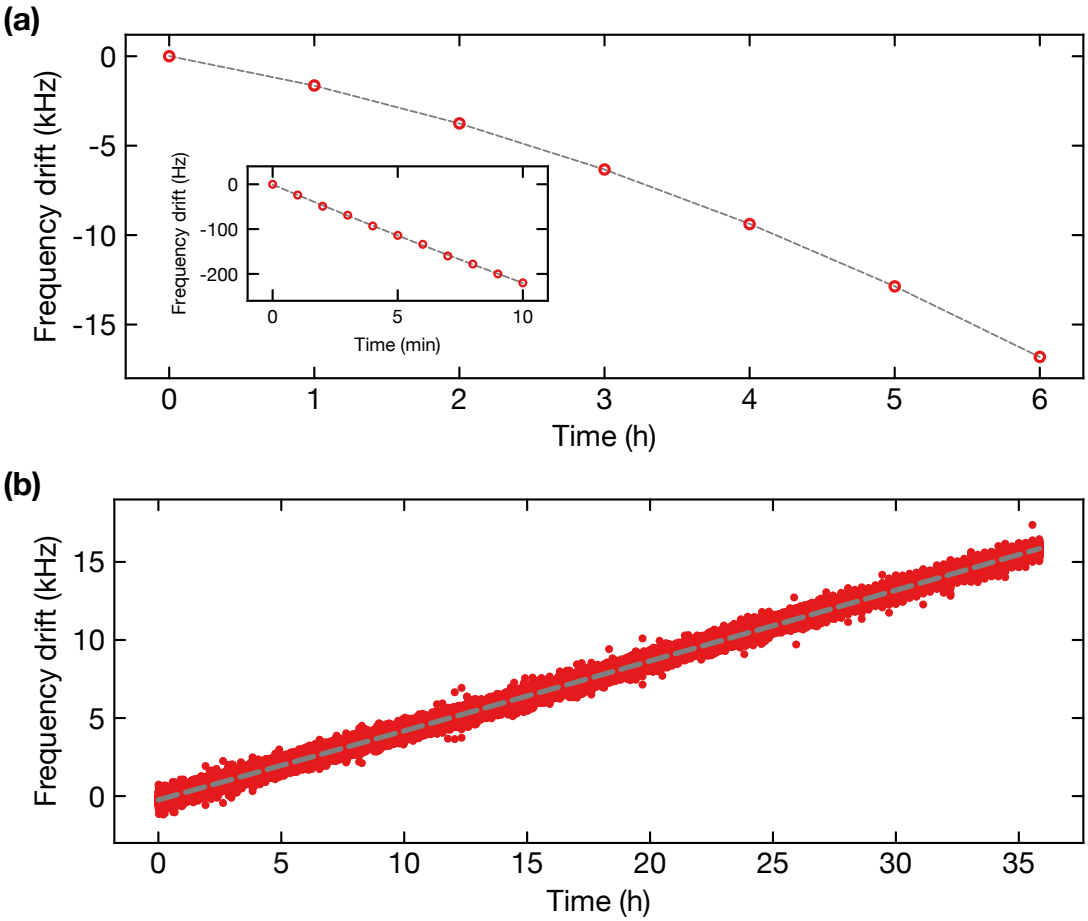

Fig. 3.10 Drift measurement. (a) Drift of the clock beat note. From a fit a first order drift of -1.424 kHz/h and an associated second order drift of -8.4 Hz/h^2 is calculated. **(b)** Frequency drift of the Toptica clock laser locked to cavity II, measured with a frequency comb. We obtain a first order drift of 439 Hz/h and a second order of -2.45 Hz/h^2

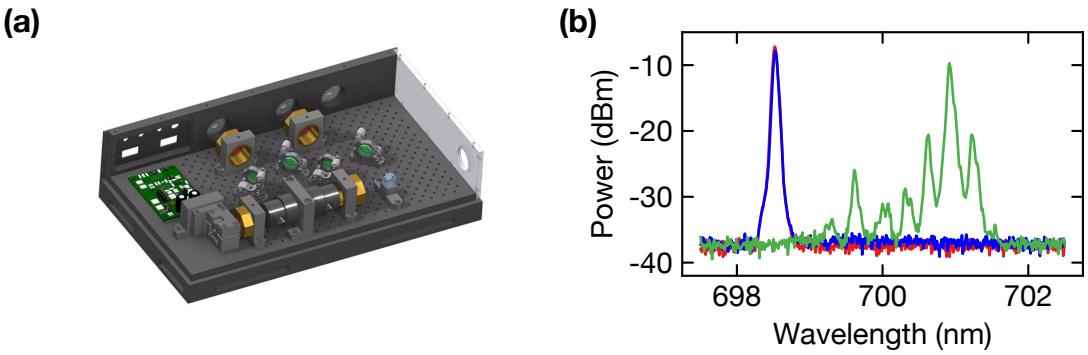

Fig. 3.11 Injection lock. (a) A module for seeding a slave diode at the master frequency. **(b)** A wavelength spectrum of the clock injection lock. The diode without (green) the seed exhibits multiple peaks. When the seed (red) is applied the slave diode (blue) starts lasing at the master frequency.

second order drift of $-8.4\ \mathrm{Hz/h^2}$. We suspect cavity I to be responsible for a large portion of the drifting. As mentioned earlier, due to the outgassing issues and the resulting vacuum problems, we can not temperature-stabilize this cavity to the zero-crossing temperature. Therefore, changes in the temperature of the lab in particular on the optical table couple to the resonator and let the cavity resonance drift in time.
To set this into perspective we also measure the bare drift of the Toptica laser locked to cavity II, which is stabilized on the zero-crossing temperature. This is done by obtaining the frequency change of the beat note between light from the locked Toptica laser and a self-referenced femtosecond *frequency comb*. An introduction to the working principle and usage of optical frequency combs can be found in Ref. [58]. For our purposes it is sufficient to approximate this tool as a ruler for light waves, with which we can measure optical frequencies. The resulting drift data over 35 h can be seen in Fig. 3.10. From a fit we get a first order frequency drift of $+439\ \mathrm{Hz/h}$ and a second order frequency drift of $-2.45\ \mathrm{Hz/h^2}$.
A comparison between the $-1424\ \mathrm{Hz/h}$ drift for the beat note and the $+439\ \mathrm{Hz/h}$ for the bare cavity II setup yields a difference that needs to be further investigated. It is also not clear if both lasers drift in the same direction or what exactly the relative drift is.

3.8 Injection Lock

After many beam splitters in the optical setup, the resulting usable optical power can be quite low. This is especially problematic for holographic beam shaping, which is inherently very power inefficient. This can be a major issue in many experiments [15]. For that reason, we built an injection lock at the clock wavelength. In an injection lock, a *slave* laser diode is injected with light from a master laser. This so-called seed light forces the slave diode to lase at the frequency of the master laser. Our setup of such a module

can be seen in Fig. 3.11. The slave diode is temperature stabilized and protected from backreflections with an isolator. By adjusting the polarization of the seed, light can pass the isolator from the other side into the slave diode. For seeding ~ 1 mW of optical power from the master laser is sufficient. After another monitoring beam splitter the beam is directed out of the module through a wedged window. Fig. 3.11(b) shows a wavelength spectrum of the diode (*Thorlabs HL 7001MG*) without any seeding light in green. By shining the seed light (red) from the master laser into the slave diode (blue), it will start lasing at the master frequency. With this method we can get up to 50 mW at 698 nm.

3.9 Outlook

The outgassing and vacuum issues of cavity I mentioned earlier require an update of the housing to our latest stainless steel version with Pelitier heaters inside. This should enable a stabilization of the ULE spacer to the zero-crossing temperature and significantly reduce long term frequency drifts of the laser. The lock for the 671 nm laser needs to be installed and optimized.
To achieve a sub-10 Hz linewidth on the main experiment an active fiber noise cancellation needs to be constructed. At first, a beat measurement after a long optical fiber should serve for benchmarking the influence of fiber noise on the laser linewidth. The proof-of-principle setup in Ref. [39] serves as a good starting point for future optimization of the circuit.
Because the injection lock is used frequently when a lot of laser power is needed at the clock wavelength, one should also measure the resulting linewidth. On the one hand, the seed light is also carried with a short optical fiber, which could make fiber noise relevant again and on the other hand, it is not clear how faithfully the linewidth of the seed light is preserved by the slave diode.

Chapter 4

Optical Imaging Theory

Optical imaging is one of the most versatile tools in the natural sciences. From early discoveries in medicine like penicillin [59] to the modern research on the origin of life [60] the possible applications span a wide range of different areas. Optical microscopy also got a rebirth at the ending of the 20st century, when *super-resolution microscopy* techniques were discovered [61–63]. With precise engineering of light modes and stochastic methods these tools offer the possibility to resolve features below the classical resolution limit for optical microscopy set by *Abbe's diffraction limit* [64]. Super-resolution microscopy can in principle enable resolution down to the low nm-scale, but relies on scattering many photons from targets that are fixed in place over a long time [65]. The atoms we like to image are trapped in an optical lattice. Since they are separated by multiple 100 nm, our resolution requirements to image them on individual sites are much lower. However, the atoms are also easily lost from the trap after taking an image, and we cannot work with the same sample over and over again. Consequently, we take a different approach by collecting the fluorescence light from the atoms with a high resolution imaging system, while simultaneously cooling the atoms. High magnification then ensures a clear differentiation between neighboring lattice sites.
In this Chapter we give an introduction to the theoretical framework necessary for describing optical microscopy. We start by discussing the emerging pattern from a single point-like emitter. We follow with an explanation of how to distinguish between multiple point emitters. The latter part focuses on the effect of imperfections in the optical system and their effect on the resolution.

4.1 Point-Spread Function

To get an understanding of optical imaging, we first have a closer look at the simple situation of a point-like source emitting light into a microscope objective. For our theoretical discussion we can approximate this objective by a single thin lens. In reality these objectives usually consist of a stack of lenses to compensate wavelength-dependent shifts and deviations from the ideal lens shape [Ch. 5]. The picture emerging from such a point-like emitter is called the *point-spread function* (PSF). In the following we discuss a derivation of this pattern for a perfect imaging system. A more detailed treatment including an introduction to the broader field of *Fourier Optics* can be found in Ref. [66].

As a starting point we imagine a setup like the one depicted in Fig 4.1. A point-like

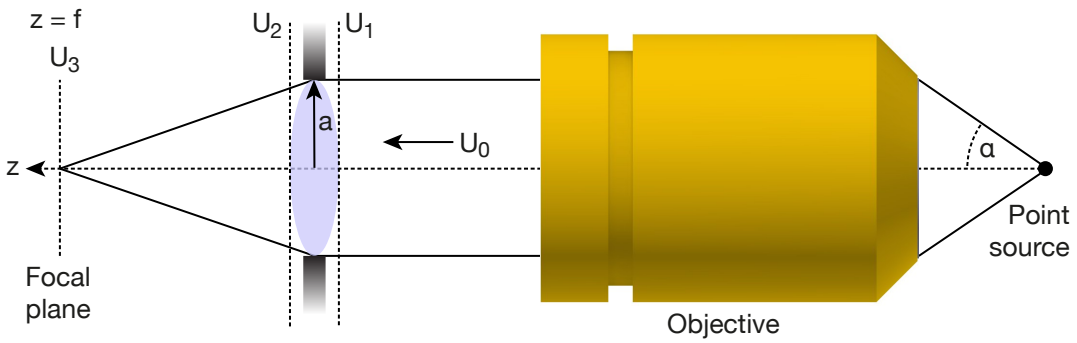

Fig. 4.1 Theoretical imaging system. A point-like source emits spherical waves, which are collected in a microscope objective up to an angle α. The objective lens converts the waves into a flat wavefront and directs them to an imaging lens with free aperture radius a. Then the light waves are focused to the final observation point in the focal plane.

source emits spherical light waves. They are collected by a microscope objective up to an angle α. The microscope objective converts the spherical waves from the emitter into a flat wavefront after the objective. Afterwards, the light is directed onto a second *ocular* lens with radius a. The finite extent of the lens defines a maximum free aperture and maximum optical beam diameter for our whole system. In practice this maximum extent is set by our objective, but for the theoretical discussion it is not important which optical element defines the aperture. The light waves passing the second lens are focused onto the focal plane. We will now calculate the image of the original point source on this final focal plane.
With the maximum angle α under which light is captured in the objective, a first characteristic value called the *numerical aperture* (NA) is defined as

$$\mathrm{NA} = n \sin(\alpha). \tag{4.1}$$

Here n is the *refractive index* of the medium in between the point source and the objective. The fraction of light collected by the imaging system is found by integrating over the solid angle covered by the objective:

$$\Omega_{\text{collected}} = \frac{1}{4\pi} \int_0^{2\pi} \int_0^{\arcsin \mathrm{NA}} \sin(\varphi)\, \mathrm{d}\varphi \mathrm{d}\vartheta = \frac{1}{2} \left(1 - \sqrt{1 - \mathrm{NA}^2}\right). \tag{4.2}$$

From Eq. (4.2) it becomes obvious that even for relatively high numerical aperture of $\mathrm{NA} = 0.66$ only 12.4 % of the light is collected by the imaging system. This manifests itself as the main photon loss mechanism in most imaging systems.
Having discussed the geometric properties of an objective we can now focus on the point spread function. We start with our point source emitting spherical waves. Once these waves pass the objective they are converted to a perfectly plane homogeneous wavefront which we can express with a constant field U_0. Consequently, our electric field $U_1(x_1, y_1)$

in front of our ocular lens is given by U_0. By introducing the *pupil function* $P(x_2, y_2)$ that defines the amplitude change in the field by the finite aperture of the lens, we can express the wavefront $U_2(x_2, y_2)$ directly after the lens as [66]

$$U_2(x_2, y_2) = U_0 P(x_2, y_2) \exp\left(\frac{ik}{2f}(x^2 + y^2)\right). \tag{4.3}$$

The complex exponent, called *phasor*, describes the quadratic phase shift a wavefront experiences when passing through a convex lens. Here, $k = 2\pi/\lambda$ is the associated wavevector of the light and f is the focal length of the ocular lens.
The field $U_3(x_3, y_3)$ in the focal plane, a distance f away from the lens, can now be calculated with the *Fresnel diffraction integral* [66]:

$$\begin{aligned} U_3(x_3, y_3, z = f) =& U_0 \frac{i \exp(ikf)}{\lambda f} \exp\left(-\frac{ik}{2f}\left(x_3^2 + y_3^2\right)\right) \\ & \iint_{\infty}^{\infty} P\left(x_2, y_2\right) \exp\left(\frac{ik}{f}\left(x_3 x_2 + y_3 y_2\right)\right) \mathrm{d}x_2 \mathrm{d}y_2. \end{aligned} \tag{4.4}$$

To solve this integral analytically, we can perform multiple transformations. Since our system has a cylindrical symmetry we can express the pupil function $P(x_2, y_2)$ in terms of polar coordinates

$$P(x_2, y_2) = P(r_2) = \begin{cases} 1, & \text{if } \leq a \text{ (Radius of lens)} \\ 0, & \text{else} \end{cases} \tag{4.5}$$

with $r_2 = \sqrt{x_2^2 + y_2^2}$. It is then convenient to express the full diffraction integral Eq. (4.4) in cylindrical coordinates [66]:

$$U_3(r_3) = U_0 \frac{i}{\lambda f} \exp(ikf) \exp\left(-\frac{i\pi r_3^2}{\lambda f}\right) \int_0^{\infty} P(r_2) J_0\left(\frac{2\pi r_2 r_3}{\lambda f}\right) 2\pi r_2 \, \mathrm{d}r_2. \tag{4.6}$$

Here we used a *Hankel transformation* to rewrite the 2D-*Fourier transfromation* in terms of polar coordinates [66]. This implies using a *Bessel function* of the first kind of order zero

$$J_0(x) = \frac{1}{2\pi} \int_0^{2\pi} \exp\left(\pm ix \cos(\varphi)\right) \, \mathrm{d}\varphi. \tag{4.7}$$

To further characterize the point spread function in all spatial directions close to the exact focal plane of the second lens, we introduce a different pupil function

$$P(r_2, z) = P(r_2) \exp\left[\frac{ikr_2^2}{2}\left(\frac{1}{f} - \frac{1}{z}\right)\right]. \tag{4.8}$$

This expression accounts for a displacement of the observation plane relative to the focal point along the optical axis. Therefore, our microscope objective will slightly defocus our optical beam at this spot and alter the PSF. We can incorporate this pupil function

back into Eq. (4.6) to calculate a quantitative change of the point spread function in the full 3-dimensional space around the focal plane of our lens. The following equation in cylindrical coordinates can then be derived:

$$U_3(r_3) = U_0 \frac{i}{\lambda f} \exp(ikf) \exp\left(-\frac{i\pi r_3^2}{\lambda f}\right) \int_0^\infty P(r_2) \exp\left(\frac{ikr_2^2}{2}\left(\frac{1}{f} - \frac{1}{z}\right)\right) J_0\left(\frac{2\pi r_2 r_3}{\lambda f}\right) 2\pi r_2 \, \mathrm{d}r_2. \tag{4.9}$$

To simplify this expression, we use the representation for the $\mathrm{NA} = n\sin(\alpha)$ defined earlier, the *Fresnel number* $N = \pi a^2/(\lambda z)$, and a normalized radius $r = r_2/a$ for the second lens. In addition, substitutions for the radial $\rho = 2\pi r_3 \,\mathrm{NA}/\lambda$ and the axial coordinates $u = 2\pi\Delta z(\mathrm{NA})^2/\lambda$ are used. In the latter case Δz represents the distance from the focal plane $z - f$.
We arrive at the final expression for the resulting electric field created by a point like source imaged trough a microscope objective

$$U_3(\rho, u) = U_0 2iN \exp(-ikf) \exp\left(\frac{i\rho^2}{4N}\right) \int_0^1 \exp\left(\frac{iur^2}{2}\right) J_0(\rho r)\, r \, \mathrm{d}r. \tag{4.10}$$

Restricting ourselves to the focal plane and subsequently setting $u = 0$ results in

$$U_3(\rho) = U_0 2iN \exp(-ikf) \exp\left(\frac{i\rho^2}{4N}\right) \int_0^1 J_0(\rho r)\, r \, \mathrm{d}r \tag{4.11}$$

for the radial distribution. Using the identity

$$\int_0^1 x_0 J_0(x_0) \, \mathrm{d}x_0 = x J_1(x) \tag{4.12}$$

derived from the Hankel transformations [66], lets us solve the integral and come up with an analytic solution for U_3:

$$U_3(\rho) = U_0 2iN \exp(-ikf) \exp\left(\frac{i\rho^2}{4N}\right) \left(\frac{2J_1(\rho)}{\rho}\right). \tag{4.13}$$

To get the final intensity distribution we take the absolute value squared and represent all the prefactors with I_0,

$$I(\rho, u = 0) = I_0 \left(\frac{2J_1(\rho)}{\rho}\right)^2. \tag{4.14}$$

This characteristic distribution is known as the *Airy pattern* [66] or in other words as the point spread function of a point like emitter. Fig. 4.2(a) shows the underlying Bessel

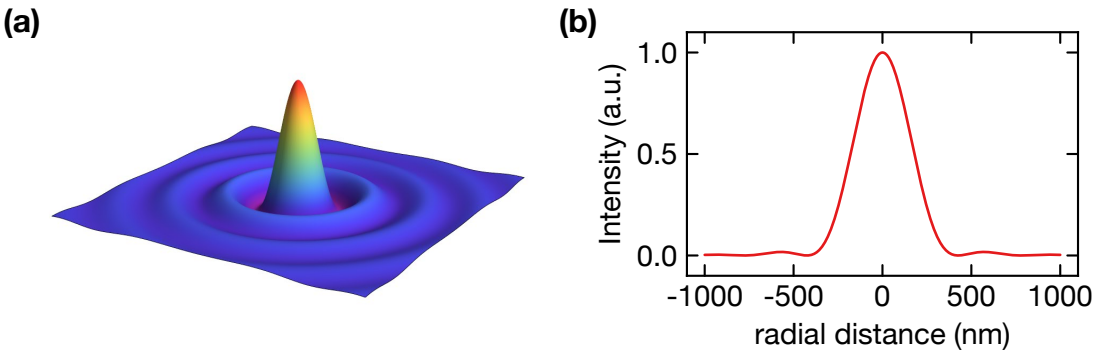

Fig. 4.2 Radial point-spread function. (a) 3D-illustration of the radial Airy function giving the PSF its characteristic shape. Besides the central peak the multiple symmetric rings are visible. **(b)** 1D-slice of the PSF along one axis in the focal plane. Plotted for a wavelength of $\lambda = 461$ nm and a $\mathrm{NA} = 0.66$.

function (not the PSF) of the first kind of order one, which gives the PSF its specific shape. Apart form the central peak the multiple radial symmetric rings are clearly visible. We can transform Eq. 4.14 back to Cartesian coordinates

$$I_{\mathrm{PSF}}(x,y) = I\left(\frac{2\pi\mathrm{NA}}{\lambda}\sqrt{x^2+y^2}\,, u=0\right) = I_0\left(\frac{2J_1\left(\frac{2\pi\mathrm{NA}}{\lambda}\sqrt{x^2+y^2}\right)}{\frac{2\pi\mathrm{NA}}{\lambda}\sqrt{x^2+y^2}}\right)^2 , \tag{4.15}$$

and plot this e.g. for a wavelength of $\lambda = 461$ nm and a $\mathrm{NA} = 0.66$ [Fig. 4.2(b)]. An important criterion for the resolution capability of the imaging system is the position of the first zero of the Airy pattern at

$$\rho_{\mathrm{zero}} = 1.22\frac{\lambda}{2\,\mathrm{NA}}\,. \tag{4.16}$$

With these expressions for the point spread function, we now have established the necessary framework to look at the axial dependence of the PSF.

4.2 Depth of Focus

The axial resolution along the optical beam, known as depth of focus (DOF), is of particular importance. It sets a limit on how far away the imaging target can be displaced from the ideal focal point on the optical axis to still be resolvable. For our particular case of a quantum gas microscope precise knowledge of the depth of focus is important. With this we can distinguish how much displacement of the atoms along the optical axis is possible to still achieve diffraction-limited resolution.
To extract the axial dependence of the PSF we can drop the radial components in Eq (4.10)

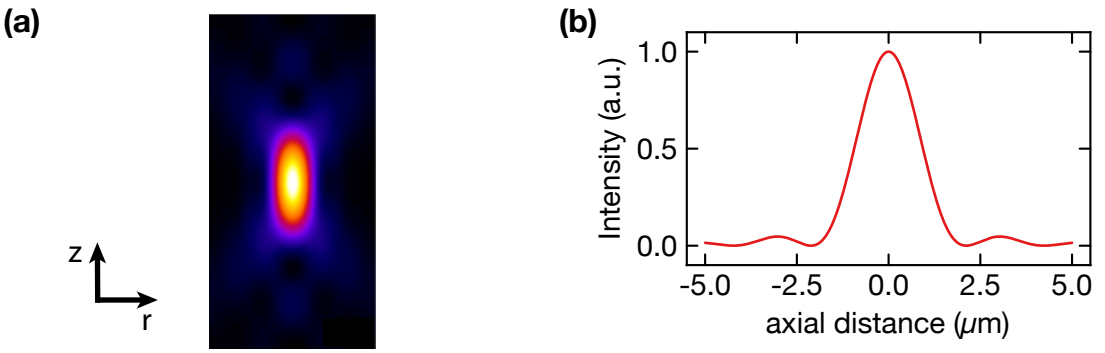

Fig. 4.3 Axial point-spread function. (a) A 2D slice along the optical axis of the point spread function [67]. **(b)** 1D slice along the optical axis. The quadratic sinc-distribution for the intensity can be seen.

and rewrite it as

$$U_3(\rho = 0, u) = U_3(u) = U_0 2iN \exp(ikf) \int_0^1 \exp\left(\frac{iur^2}{2}\right) r \, \mathrm{d}r. \tag{4.17}$$

Solving the integral and squaring the expressing leads to the intensity pattern

$$I(\rho = 0, u) = I(u) = I_0 \left(\frac{\sin(u/4)}{u/4}\right)^2 \tag{4.18}$$

along the optical axis z. We find a quadratic sinc-function, which is plotted for a wavelength of $\lambda = 461$ nm and a $\mathrm{NA} = 0.66$ in Fig. 4.3(b). The full 3D intensity shape of the point spread function is obtained by the square of Eq. (4.10). A numerical solution of this integral can be found in Fig. 4.3(a).
For a more qualitative analysis we can introduce *Rayleigh units* [66]

$$\Delta_{\mathrm{Rayleigh}} = \frac{\lambda}{n \sin(\alpha)}. \tag{4.19}$$

The quadratic sinc-behavior for the axial dependence of the PSF intensity in (Eq. 4.18) can be rewritten as

$$I(z) = I_0 \left(\frac{\sin(\pi z/(2\Delta_{\mathrm{Rayleigh}}))}{\pi z/(2\Delta_{\mathrm{Rayleigh}})}\right)^2. \tag{4.20}$$

We find a 59.5 % reduced intensity at $z = \Delta_{\mathrm{Rayleigh}}$ and the first zero in the pattern at $2z = \Delta_{\mathrm{Rayleigh}}$. The Rayleigh units offer a measure over which distance around the focus the objective still exhibits diffraction-limited performance. If we assume the refractive index for vacuum as $n = 1$, the depth of focus can be estimated with the following equation:

$$\Delta_{\mathrm{DOF}} = \frac{\lambda}{\mathrm{NA}^2}. \tag{4.21}$$

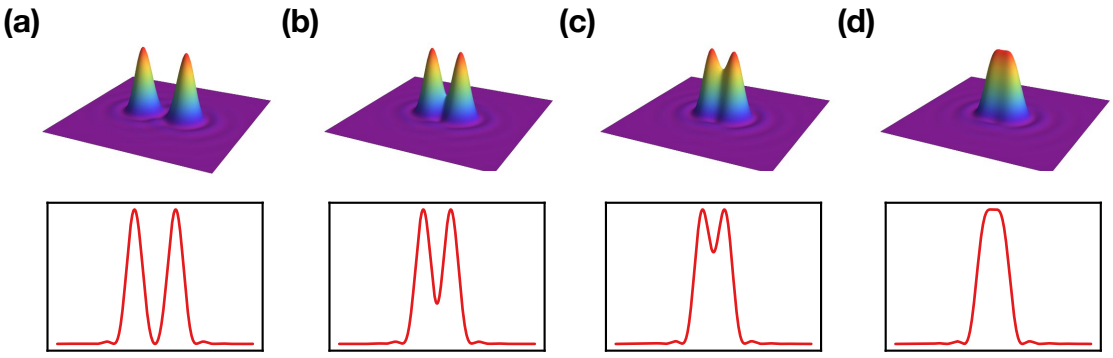

Fig. 4.4 Resolution criteria. (a) *Total resolution limit* with a contrast of $V = 1$. Both first minima of the PSFs coincide. **(b)** *Visible resolution limit* with a contrast of $V = 0.59$. **(c)** *Rayleigh resolution limit* with a contrast of $V = 0.15$. The first zero of one PSF coincides with the PSF of the other PSF. **(d)** *Sparrow resolution limit* with a contrast of $V = 0$ and vanishing curvature between the two PSFs.

4.3 Spatial Resolution Limits

Having discussed the pattern of a single emitter we will now focus on multiple emitters in close proximity. Under a microscope, each point-like source is displayed with a point spread function. Distinguishing between two different points is then essentially limited by how much their two point-spread functions overlap. Hence, the resolution depends on the physical distance of the points Δx (center of the PSFs), the imaging wavelength λ, and the numerical aperture NA of the objective. To quantify the resolution we introduce the contrast V between two point spread functions

$$V = \frac{I_{\mathrm{PSF}}(0,0) - I_{\mathrm{PSF}}(\Delta x/2, 0)}{I_{\mathrm{PSF}}(0,0) + I_{\mathrm{PSF}}(\Delta x/2, 0)}\,. \tag{4.22}$$

This contrast V characterizes the depth of the valley between the two PSFs relative to the maximum intensity. In our theoretical analysis we assume an equal intensity maximum for all point spread functions. From the contrast we can define different criteria for the resolution limit [68]. Figure 4.4 shows an overview of the different definitions. We calculate a 3D picture of the point spread functions in the respective limit and a 1D slice along the maxima. *Total resolution* [Fig. 4.4(a)] is achieved when both first minima of the point spread functions coincide. This limit yields a contrast of $V = 1$. To be above the *visible resolution limit* [Fig. 4.4(b)] the contrast needs to be larger than $V = 0.59$. The cones of the PSFs start to overlap even more for the *Rayleigh limit* [Fig. 4.4(c)]. Here the contrast is $V = 0.15$. With this contrast the first zero of one PSF coincides with the maximum of the other PSF. If the curvature of the combined intensity pattern vanishes between the individual point spread functions we are at the *Sparrow limit* [Fig. 4.4(d)]. The contrast then reduces to zero. With these criteria we now have a quantitative way of analyzing the resolution capabilities of an objective.

An essential characteristic of our experiment is the extent of the point spread function compared to the optical lattice spacing. As mentioned earlier, our primary imaging lattice will be at a wavelength of 914 nm with a spacing of 457 nm. We can now put multiple point spread functions on this lattice to simulate pictures we would expect for the quantum gas microscope.
For the blue imaging wavelength, we can clearly distinguish between different lattice sites [Fig. 4.5(a)]. With a contrast of 0.53 we are above the Rayleigh limit but are very close to the 0.59 value required for visible resolution. In Fig. 4.5(b) a typical picture of randomly distributed point spread functions on a 914 nm lattice can be seen. Here, even without any further analysis of the picture we can clearly determine the occupation of each site.
At the red imaging wavelength of 689 nm the resolution decreases. We find a contrast of 0.24. This value implies that we are also above the Rayleigh limit, but with a much lower contrast than in the blue case. If we plot the point spread function on a lattice the overlap of the central cone of the PSF between neighboring sites is visible [Fig. 4.5(c)]. A closer look at the randomly distributed point spread functions on the lattice reveals an image where it is not easily possible to measure the occupation of each site without further image processing. In Ref. [11] this issue was solved by taking the underlying lattice structure into account. Since we know that the PSF can only be at discrete points of the regular lattice a *deconvolution algorithm* can enhance the resolution [69].
In summary, imaging at the blue 461 nm transition turns out to be much more favorable for the achievable resolution and contrast without further image processing.

4.4 Optical Aberrations

Up to now we only looked into ideal systems. Any real optical system on the other hand will eventually include imperfections. We call these imperfections *optical aberrations*. Slight displacement of elements in the optical path can be one origin of these aberrations. Another reason can be a deviation of the lens shape from the ideal form. This will result in a slightly different bending of light rays, which causes imperfections. Even without an ideal lens shape different wavelengths are diffracted differently at the same lens. This results in another type of imperfection known as *chromatic aberration*.
We can interpret all global distortions as a bending of the wavefront and a change in the phase map. In a mathematical way we can express this change with *Zernike polynomials*. These functions are defined as

$$Z_n^{\pm m}(r,\phi) = R_n^m(r)\begin{cases} \cos(m\phi) & \text{for even } m \\ \sin(m\phi) & \text{for odd } m \end{cases} \tag{4.23}$$

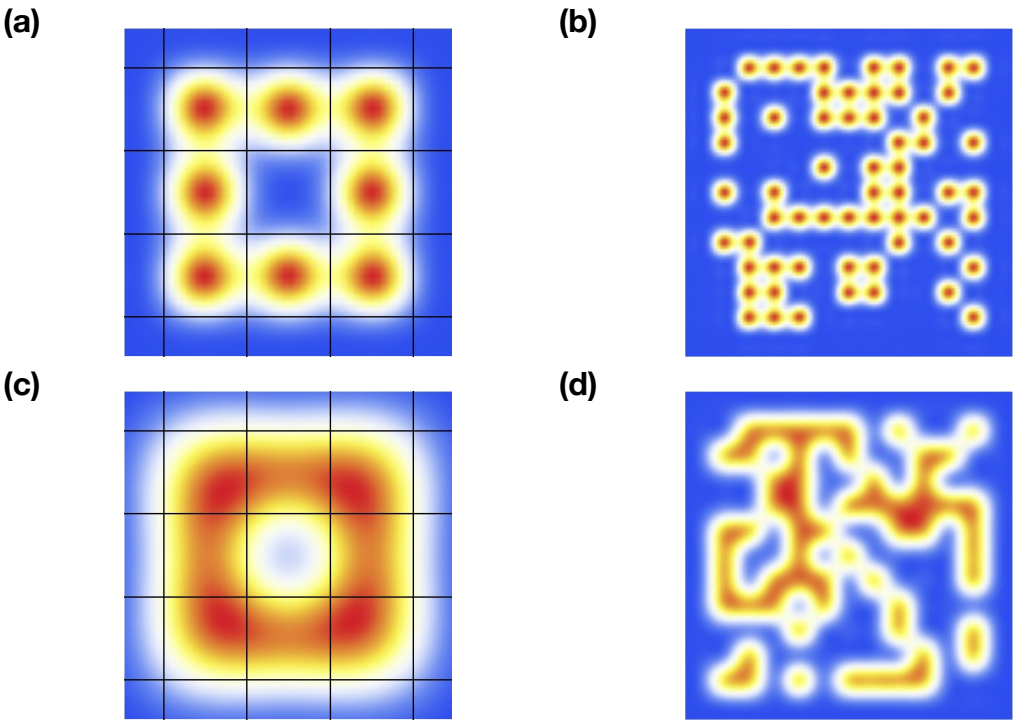

Fig. 4.5 PSF on lattice. (a,b) The point spread functions for blue light on a 914 nm lattice are clearly distinguishable. **(c,d)** For red imaging the cones of the point spread functions start to overlap strongly. For distinguishing between neighboring lattice sites additional image processing could be needed.

with the radial component being

$$R_n^m(r) = \sum_{k=0}^{(n-m)/2} \frac{(-1)^k (n-k)!}{k!((n+m)/2-k)!((n-m)/2-k)!} k^{n-2k} \,. \tag{4.24}$$

They form a complete orthogonal basis on the unit circle. We can assign a particular optical aberration to each polynomial order. In Fig. 4.6 we display the five most common distortions including their corresponding Zernike polynomials. In addition, the matching fringe map obtained by interfering the wavefront with a plane wave is shown. Furthermore, we also plot the effect on the actual PSF for an increasing amplitude of the polynomial.
It is worth mentioning, that the phase error is not directly represented by the Zernike polynomial. Instead, if we project a wavefront on a specific polynomial the projection will be proportional to the actual aberration described by the Zernike polynomial.
Certain aberrations can be also useful. Figure 4.6(a) shows e.g., that tilt does not change the shape of the point spread function. It only shifts the position with respect to the optical axis. Therefore the resolution is still the same. We can exploit this shift as a tool to

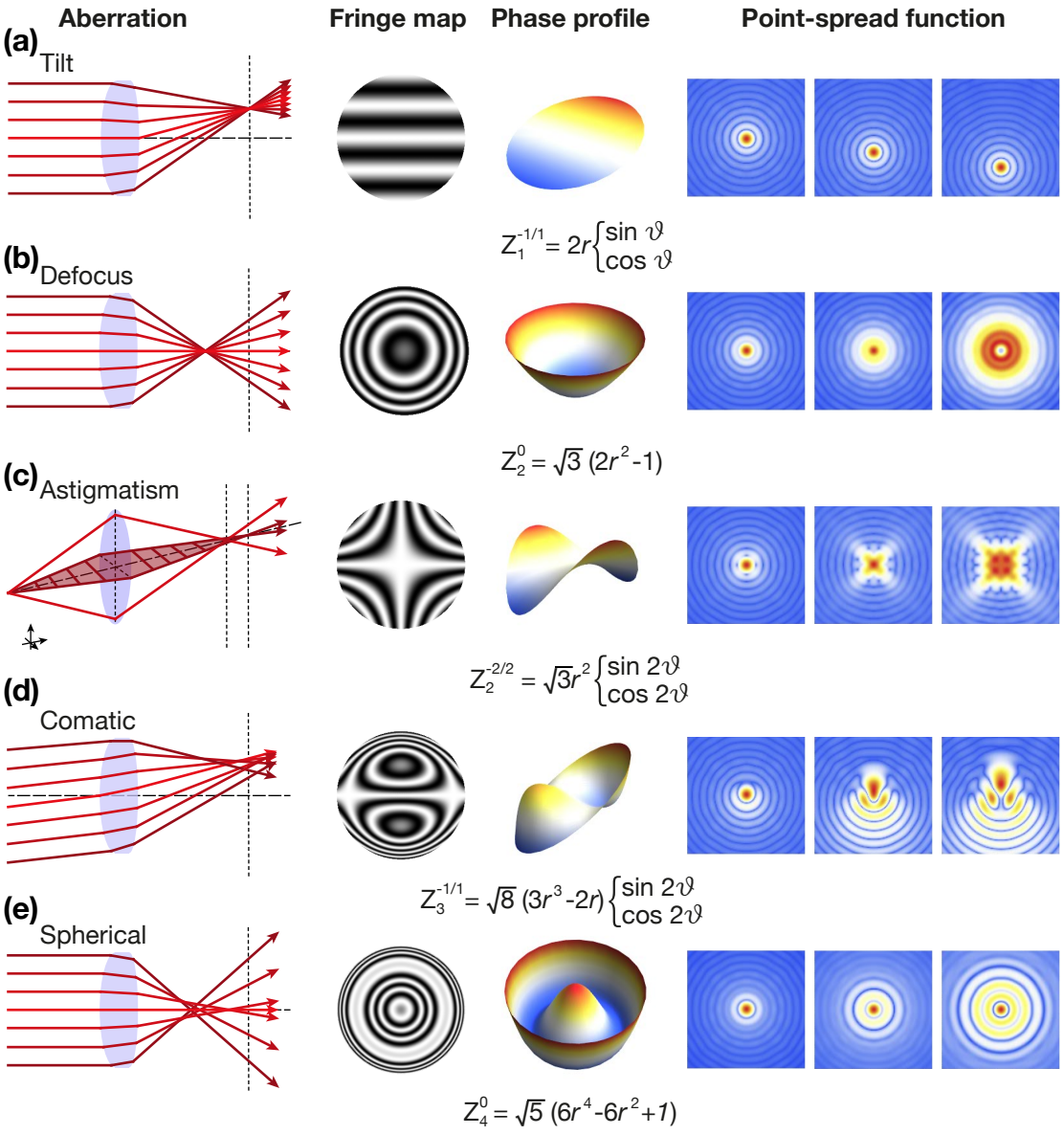

Fig. 4.6 Optical aberrations. The five most common optical aberrations with the corresponding Zernike polynomials are shown. The matching fringe map obtained by interfering the wavefront with a plane wave is depicted. For each Zernike polynomial we also plotted the effect on the actual PSF. The amplitude for the distortion increases to the right.

move the PSF in the focal plane. This technique can be useful, e.g. to address different atoms in an optical lattice.
We find, that imperfections in real optical systems cause a phase distortion in the wavefront, which we can characterize with Zernike polynomials. If the quality of a PSF for a given wavelength is not limited by system imperfections, but instead is defined purely by the numerical aperture, we call this behavior *diffraction limited*. Real microscope objectives also only exhibit diffraction limited performance over a finite region around the optical axis in the focal plane. This region is called the *field of view*.

4.5 Outlook

With the theoretical tools developed in this chapter we are now able to analyze real microscope objectives. We can characterize the point spread function and quantify the optical aberrations present in the real system.
Throughout this chapter, we approximated light as a scalar field. Since light waves have a polarization, a vector field is needed to exactly describe the full phenomena. A vectorial description of the light field reveals the effect of polarizations on the PSF. This extension also shows optical aberrations not covered by Zernike polynomials. Since our NA is moderate (below 0.7), a scalar approximation seems to be sufficient for our following characterization. A vectorial treatment of the problem can be found in Ref. [66].

Chapter 5

Microscope Objective Characterization

The main purpose of the objectives is to perform single-site imaging and addressing of atoms in optical lattices. For our quantum gas microscope we purchased two custom microscope objectives from *Special Optics*. For imaging we tested the objectives for the blue $^1\mathrm{S}_0 \rightarrow {}^1\mathrm{P}_1$ transition at 461 nm and for the red $^1\mathrm{S}_0 \rightarrow {}^3\mathrm{P}_1$ transition at 689 nm. Since addressing will be done on the $^1\mathrm{S}_0 \rightarrow {}^3\mathrm{P}_0$ clock transition we also characterize both objectives at 698 nm.
In the main experiment only one of the two objectives will be built in. Therefore one of the major goals for this characterizations is to find out which one performs better.
In this chapter we start by explaining the objectives. We take a closer look at their interior and summarize the specifications at the different wavelengths. After that, we characterize the reflection and transmission properties for both objectives. This is followed by a detailed description of the test setup for measuring the point spread functions. We present our resulting PSFs for both objectives at three different wavelengths. Finally, we compare our findings to already existing quantum gas microscopes.

5.1 The Objective

Modern microscope objectives are typically made from a stack of lenses. With multiple lenses, chromatic shifts can be corrected giving the objective similar optical performance at different wavelengths.

Our objectives consist of 6 lenses. Starting from the focal point, the location where the emitters sit, the light expands into free space over 7.5 mm. The light then passes a 5 mm thick vacuum window. Later in the main experiment, the free expansion will be in vacuum inside our science chamber. We should also note that the mount for the science cavity creates an additional $\sim$100 μm thin split between the cavity spacer and the window which increases the distance to the view port to $\sim$7.6 mm. Due to refraction, light rays are redirected when passing a glass plate. The lenses are designed to compensate for this glass plate and the corresponding spherical aberrations that result from this refraction. The objective is placed 1.08 mm after the glass plate. Inside the objective, light diffracts at the first *hemisphere* lens. This optical element ensures a maximum collection of light over the given solid angle. The following *triplet* lens compensates for chromatic shifts. An additional *meniscus* lens counteracts spherical aberrations and shortens the overall focal length. The final *rear* lens collimates the output beam, and makes the objec-

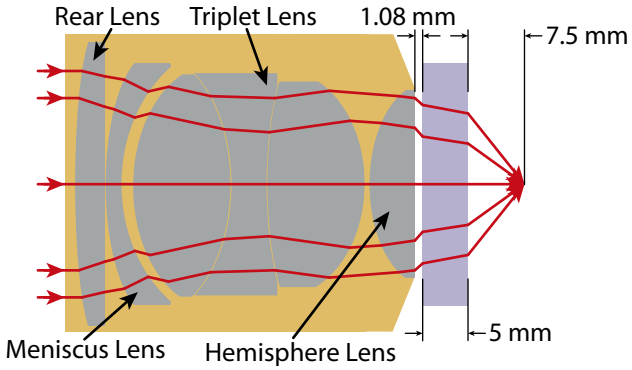

Fig. 5.1 Microscope Objective. The Objective consists of 6 lenses. It is corrected for a 5 mm thick fused silica plate. The objective is specified with an numerical aperture of $\mathrm{NA} = 0.66$ and an effective focal length of 26 mm. The field of view is 100 μm.

tive *infinity corrected*. Our objective has a maximum free aperture of 35 mm (diameter) at the back plane. The overall numerical aperture is $\mathrm{NA} = 0.66$, with an effective focal length of 26 mm. The field of view of the objective is 100 μm (diameter).

In Figure 5.2 we display the simulated point spread functions (red) for both imaging wavelengths at 461 nm [Fig. 5.2(a)] and 689 nm [Fig. 5.2(b)]. Figure 5.2(c) also shows the PSF for the addressing wavelength at 698 nm. The specified point-spread functions were obtained from a *Zemax* file the company kindly sent us. We also plotted the theoretical diffraction-limited PSF for each wavelength (blue). Diffraction-limited performance is found for all three wavelengths. In addition, a *Gaussian* fit (yellow) is included in each graph. The fit curve and the real PSF show negligible deviations at the full width half maximum. Only at the first zero of the point spread function the Gaussian does not fall to zero but rather decreases exponentially. Hence, we see that a Gaussian can be a good approximation to obtain the full width half maximum of a point-spread function.

Dispersion shifts the focal point between the different wavelengths. Fig. 5.2(d) shows this shift depending on the wavelength. We set the focal shift at 461 nm to zero. For the clock wavelength at 698 nm this shift can be as large as 2 μm. For focusing in the same plane the shift has to be taken into account when designing an optical setup. By slightly focusing or defocusing the optical beam on the objective back plane the focal shift can be compensated for.

After the delivery of the objectives we found multiple scratches on the front lens of objective I (001) [Fig. 5.3(a)]. This damaged objective was therefore sent back to the company for repair. Fig. 5.3(b) shows the front lens of the repaired objective. We found no remaining scratches.

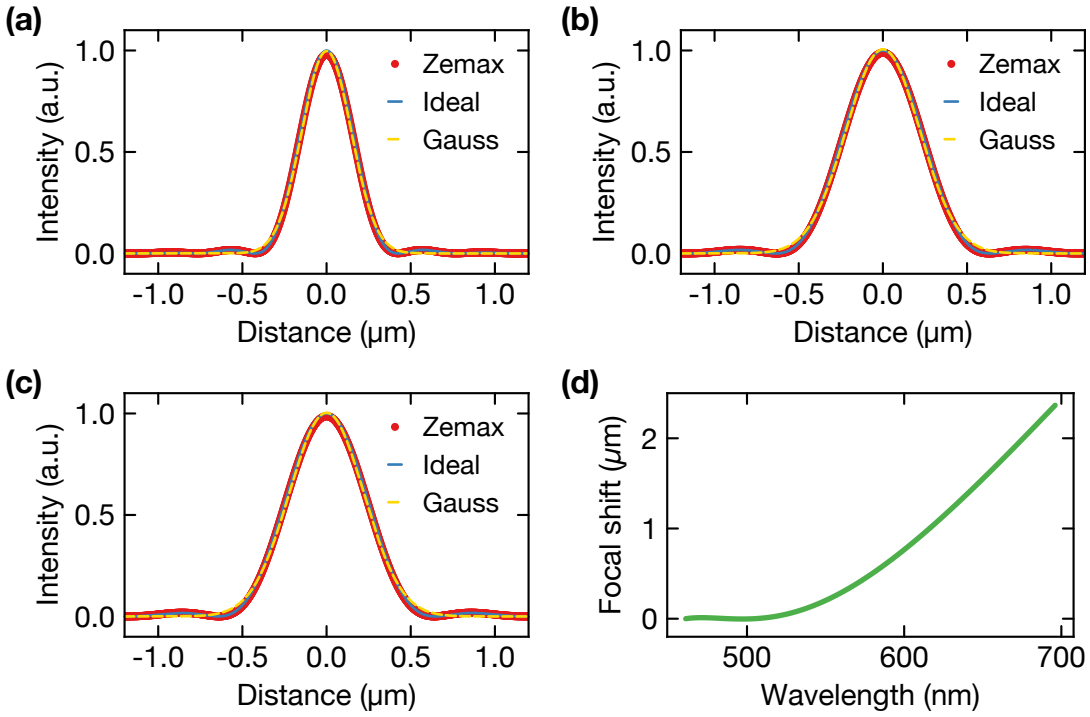

Fig. 5.2 Specified point spread functions and focal shift. The simulated (red) and the ideal (blue) PSF are plotted for 461 nm **(a)**, 689 nm **(b)** and 698 nm **(c)**. In addition a Gaussian fit (yellow) is displayed. In **(d)** the chromatic shift of the focal point depending on the wavelength for the objective is shown.

5.2 Reflection and Transmission

For imaging it is important to know the overall collection efficiency of the imaging path. It is necessary to characterize how many photons the atoms scatter and what fraction can eventually be detected on a camera. Also for sending beams through the objective onto the atoms, the transmission needs to be known to determine the intensity in the focal plane. As mentioned earlier, our z-component of the optical lattice will be made by retro reflecting a beam from the front surface of the microscope. For that reason, our objectives are manufactured with a highly reflective coating on the front lens. Consequently, the reflection coefficient of the objective is also of interest. Optical lattice beams typically carry a lot of power. By comparing the reflection and transmission we can calculate the power that is dissipated inside the objective. Too much dissipation can heat the objective which results in an expansion of the objective housing and consequently a change in distance between the lenses. This change can deteriorate the resolution quality of the objective.

We measured the transmission from both sides of the objectives (I and II) for 461 nm, 689 nm and 698 nm. The optical setup for this measurement is depicted in Fig. 5.4(a).

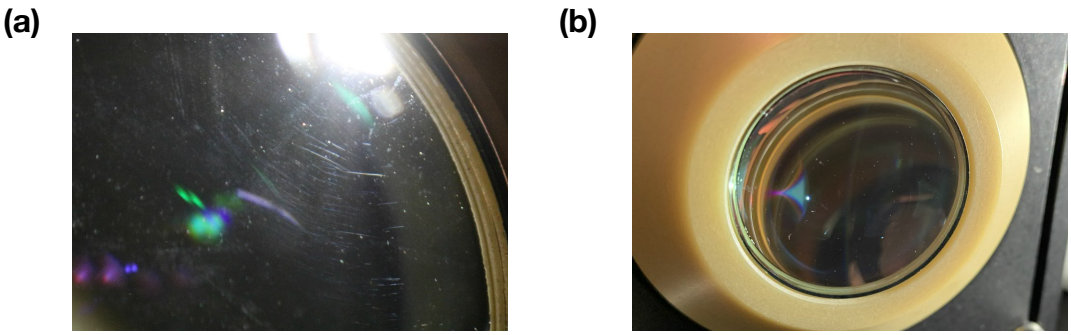

Fig. 5.3 Scratches and repaired objective. (a) Objective I was damaged with multiple scratches on the front lens. **(b)** After the repair no remaining scratches are visible.

The specific wavelength is polarization-cleaned and directed onto the objective with a beam waist of 1.32 mm. The transmission is calculated from the measured power directly before and after the objective. For measuring the transmission from the back to the front plane, the objective is flipped. We characterized the reflection from the first lens by slightly tilting the objective and redirecting the reflection onto a power meter with a D-shaped mirror. All measurements were repeated 10 times and then averaged. The results for both objectives are shown in Tab. 5.1. All values agree within 2 %. For objective I the transmission for 461 nm light is 1.1 % higher, which could be favorable for blue imaging. The second objective (II) has a 1.4 % higher transmission at 689 nm. This on the other hand benefits red imaging. For addressing on the clock transition we compare the transmission from back to front plane at 698 nm. Objective II has a 0.7 % higher transmission at this wavelength.
For measuring the reflection and transmission at the two lattice wavelengths 1064 nm and 813 nm we built a second optical setup. Since the z-lattices will be made by retro-reflecting a beam from the front surface, we need to characterize the reflections under a zero degree angle of incidence. The reflected light can then not be separated with a D-shaped mirror. As a light source for 1064 nm we use a Mephisto laser from *Coherent*. To protect the laser from any back-reflections an additional isolator is placed directly after the laser. Later in the main experiment approximately $\sim$43 W of optical power with a beam waist of $\sim$400 μm (set by the mode diameter of our science cavity) will be sent onto the front lens of the objective. To emulate these conditions we reduced the beam waist in our test setup with two lenses to $\sim$56 μm. With a power of $\sim$850 mW this yields a similar intensity on the objective. The overall damage threshold of the coating on the first lens is specified as 8-12 kW/cm^2 at a wavelength of 1064 nm and a beam waist of 1 mm. Before the light is sent onto the objective it is polarized with a $\lambda/2$ waveplate. A high-quality Brewster plate in combination with a $\lambda/4$ waveplate separates the incident from the reflected light. The Brester plate acts as a polarizing beam splitter. Light which is back-reflected from the objective passes the $\lambda/4$ waveplate twice. This shifts the polarization of the reflected light to be orthogonal to the incident beam. The reflection is

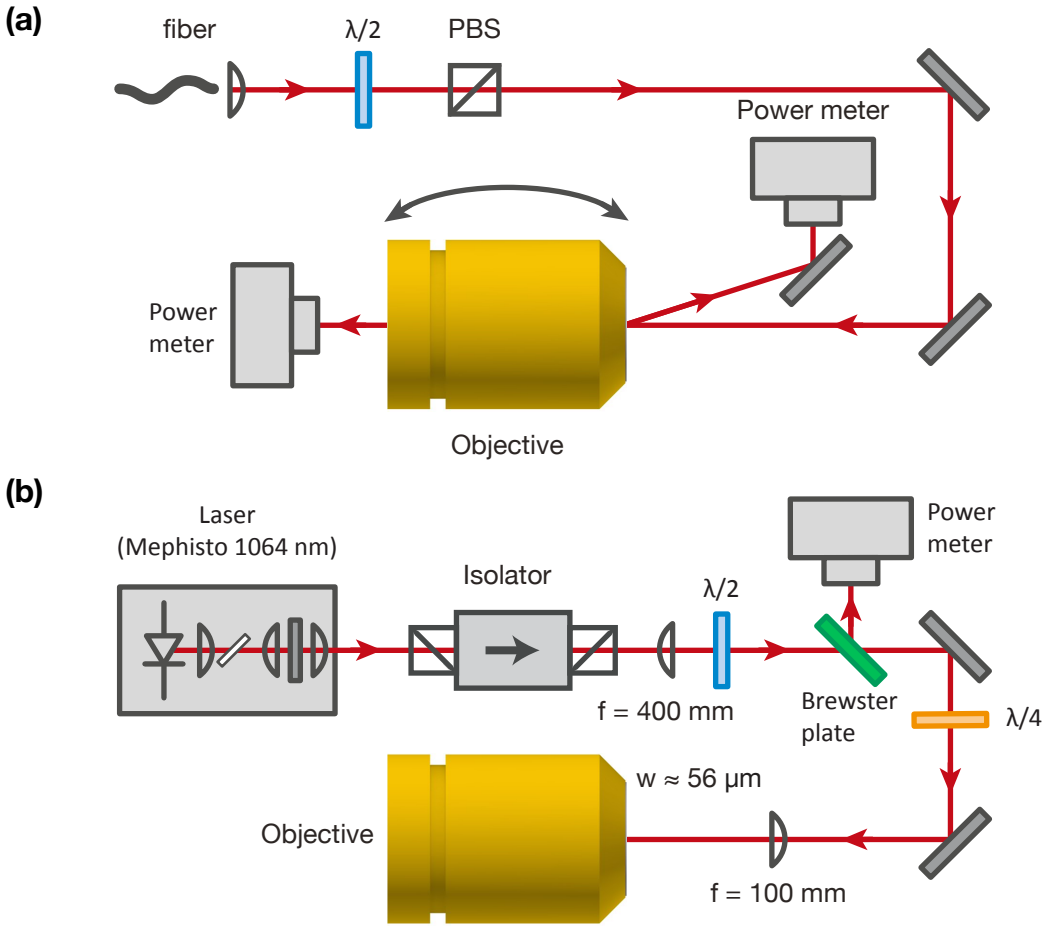

Fig. 5.4 Reflection and transmission setup. (a) Setup for measuring reflection and transmission for 461 nm, 689 nm and 698 nm. For determining the transmission from the back to the front plane the objective is rotated **(b)** Optical setup for measuring the reflection and transmission at the lattice wavelengths of 813 nm and 1064 nm. The beam waist is adjusted to have the same intensity as a real lattice beam. The objective is hit orthogonally under zero degree angle of incidence.

directed onto a power meter. For 813 nm we use light from a Titanium-Sapphire laser in a similar setup.
We find a difference of 0.5 % in the reflection coefficient at 1064 nm between both objectives [Tab. 5.1]. For a 43 W beam, this leaves $\sim$ 200 mW more power that needs to be filtered after the objective or is absorbed in it. By subtracting the reflection and transmission we obtain the dissipated power. This percentage is scattered or absorbed by the objectives. For a 43 W beam $\sim$ 100 mW are dumped in objective I and $\sim$ 280 mW in objective II. At 813 nm the first objective has a higher reflectivity of 0.5 %.
In summary, objective I is superior in the transmission of blue light and in the reflection of the lattice wavelengths. Objective II on the other hand has a higher transmission for

Tab. 5.1 Reflection and Transmission of the objectives.

		Objective I	Objective II
Blue (461 nm)	Transmission	81.5(1)%	80.4(3)%
	Reflection	1.73(2)%	3.11(2)%
	Transmission (back → front)	82.4(2)%	83.0(1)%
Red (689 nm)	Transmission	91.8(1)%	93.2(2)%
	Reflection	1.24(1)%	0.99(1)%
	Transmission (back → front)	93.0(2)%	93.1(3)%
Clock (698 nm)	Transmission	91.8(1)%	92.8(2)%
	Reflection	0.71(3)%	0.29(3)%
	Transmission (back → front)	92.9(1)%	93.6(1)%
Lattice (1064 nm)	Transmission	0.26(1)%	0.34(1)%
	Reflection	99.5(1)%	99.0(1)%
	Dissipated power	0.24(1)%	0.66(1)%
Magic Lattice (813 nm)	Transmission	0.86(1)%	1.09(1)%
	Reflection	97.9(3)%	97.4(1)%
	Dissipated power	1.24(3)%	1.51(1)%

red and clock light.

5.3 Characterization setup

The main goal of the characterization is to measure performance at different wavelengths. For that purpose we need to image point-like emitters through the microscope objectives. From the imaged patterns the PSFs can be extracted. For this reason, we built a high NA test setup [Fig. 5.5]. A major concern in this setup is the imaging target. To approximate a specific pattern as a point-like emitter, the feature needs to be substantially smaller than the wavelength of the light used for imaging.
For our purposes we need a target with an extent on the order of 100 nm. Since pin holes are typically not available at these length scales we use a custom target plate (*Sterntest*). This device is a glass plate coated with aluminum. Small defects in the coating serve as point-like light sources when illuminated from below. The size of the defects is 200 nm on average.
In the main experiment the setup will be as follows: The atoms inside the science cavity emit photons. The light then passes a custom bucket window, which has an anti-reflection coating for wavelengths from 461 nm to 1064 nm. Directly behind the window the microscope objective is installed. After the photons pass the objective, they are redirected through the imaging lens onto an EMCCD Camera.
To emulate this scenario, we place an identical bucket window in our test setup. This

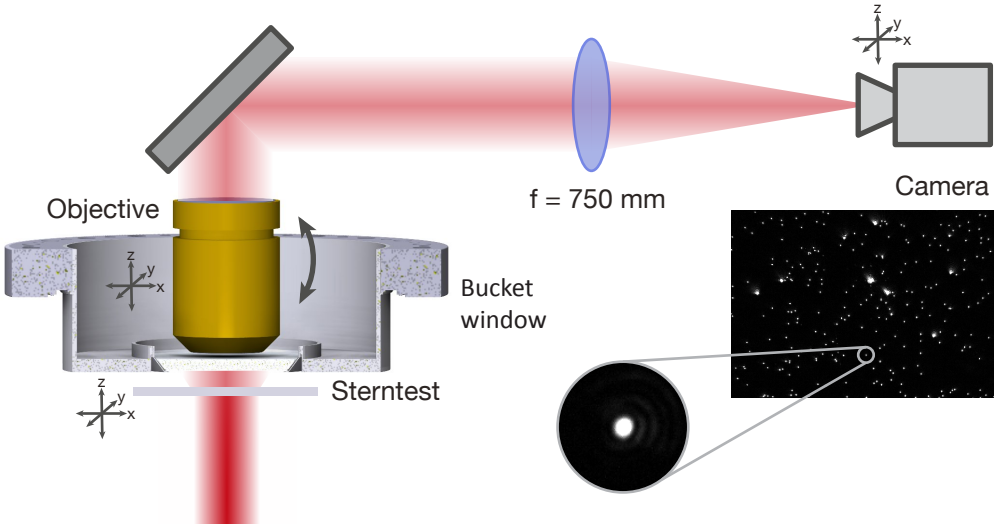

Fig. 5.5 Characterization setup. The test target (*Sterntest*) is illuminated from below. The light passes a window and the objective before it is directed with a mirror through the imaging lens. In the focal point of the imaging lens sits the camera. In the inset a typical camera image of the test target through the objective can be seen.

simulates the conditions in the main experiment as closely as possible.
A drawing of our setup is displayed in Fig. 5.5. We illuminate the target plate with light at the wavelength of interest from the bottom. To precisely adjust the positioning of the plate, we mounted it to a three-axis translation stage. The light from the point-like emitters then passes the bucket window. Afterwards, we collect the light in the microscope objective. Since fine adjustment of the objective positioning is absolutely crucial for the setup, we connected the microscope to another translation stage. This platform can move the objective in all three spatial dimensions and also allows for tilting out of the xy-plane. Behind the objective a mirror directs the light through an ocular lens with a focal length of 750 mm. In the focal point of this lens sits the final imaging camera, also mounted to a three-axis translation stage. All distances are adjusted, such that the target, objective, ocular lens and the camera resemble a 4-f imaging system. This type of imaging system projects the identical wavefront in the focal plane of the objective onto the focal plane of the ocular lens, where the camera sits [38]. The long focal length of the ocular lens ensures a large magnification of the individual point spread functions on the camera. A typical PSF from one emitter extends over 45×45 pixels, with a camera pixel size of 1.65 μm. In the inset of Figure 5.5 an over-exposed image of the illuminated target can be seen.
After construction of the test setup, the alignment turned out to be very sensitive. To suppress mechanical vibrations, we placed rubber plates under the breadboards. Since we measured two objectives multiple times, the alignment was redone and optimized on numerous occasions. For the alignment, the diameter of the illumination beam was reduced with an iris. For alignment we use a reference beam, which defines our optical

axis in the whole setup. Without the target plate and the objective in place, we centered all components in the setup on the optical axis of the beam. After this we inserted the objective. Attention was paid to the central positioning of the objective on the optical axis of the illumination beam. To ensure maximum parallelism between the window and the objective, we overlapped the back reflections of both over more than 5 m. Another method for parallel alignment is to couple both reflections back into the optical fiber of the illumination beam and to optimize the power on the other side. It turned out that this parallelism contributes the most to the quality of the point spread function. With an iris behind the objective, we also centered the back reflections of the ocular lens and the camera on the optical axis. As a last step we inserted the target pattern at the focal point of the objective.
With this high resolution imaging setup we can now test the capabilities of both objectives at different wavelengths.

5.4 Point-Spread Functions

After discussing the alignment of our test setup we are now ready to characterize the microscope resolution.
All point-spread functions are averaged over 10 data sets. We slice the resulting PSFs along the x and y- direction at the maximum. Figure 5.6 shows the results for objective I. The findings for objective II are presented in Figure 5.7. All plots include a theoretical curve for the ideal PSF.
For the blue imaging wavelength at 461 nm we find the strongest deviation between the experimental data and the theoretical optimum. We obtain a FWHM of 412 nm for objective I from a Gaussian fit with a deviation of $\sim$ 14% from the ideal value of 360 nm. Both axes show a very similar behavior [Fig. 5.6(a)]. The side peak on the right points to a comatic aberration resulting from a residual tilt in the setup. The PSF does not converge to the first zero of the ideal curve. There are two possible explanations for this increase in size. First, the target is not positioned perfectly in the focus. With the translation stage we do not have the capability to adjust the position on the 100 nm scale. A piezo-stage would enable positioning on the 10 nm scale. The second reason for the deviation can be the finite size of the target defects. With an average diameter of 200 nm, the defects are almost half the size of the imaging wavelength. Thus, the targets can no longer be approximated as point-like emitters at this wavelength. The width of the point-spread function will effectively increase with the target extent. For the second objective (II) we find a similar result for the PSF [Fig. 5.7(a)]. Here no comatic aberration is present. Consequently, we conclude that the alignment for objective II had no residual tilt. For objective II, the blue PSF is also enlarged compared to the theoretical curve. This increase supports the fact that the test targets can no longer be approximated as point sources. We find an overall FWHM of 414 nm for objective II with a deviation of $\sim$15 % from the ideal value.
The measurement for our second imaging wavelength at 689 nm agrees to a large extent

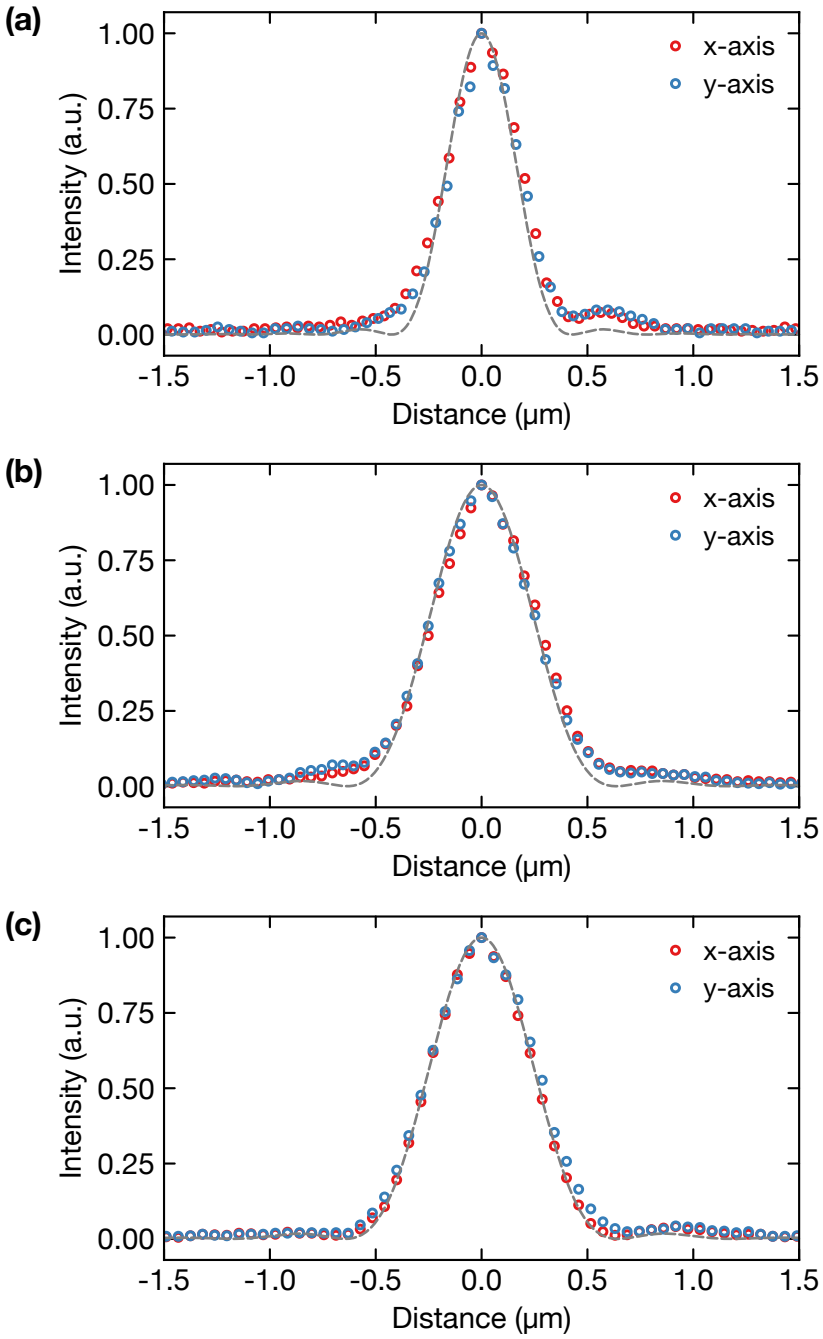

Fig. 5.6 Point-spread functions of objective I. Displayed for 461 nm **(a)**, for 689 nm **(b)** and for 698 nm **(c)**. All PSF are averaged over 10 individual points. Ideal theoretical PSFs are displayed in gray.

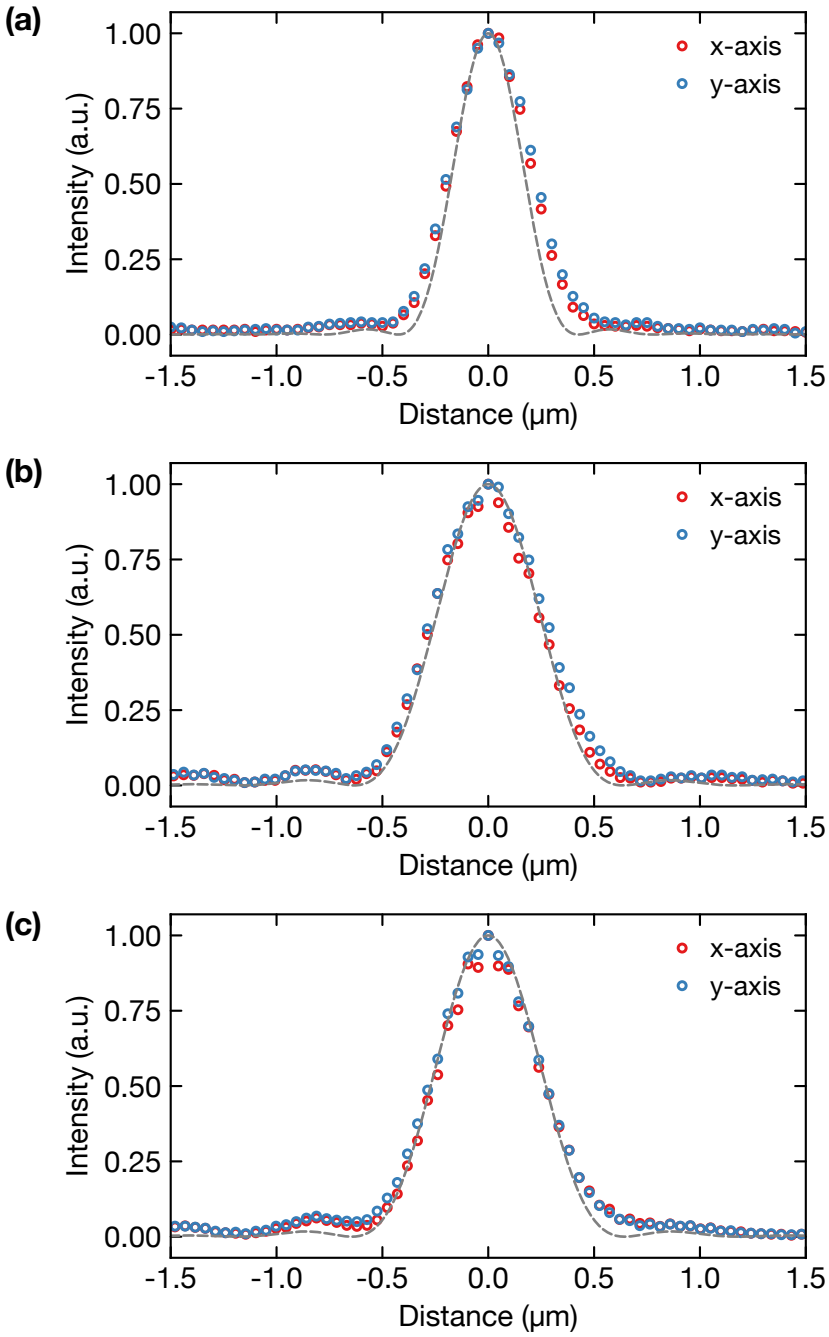

Fig. 5.7 Point-spread functions of objective II. Displayed for 461 nm **(a)**, for 689 nm **(b)** and for 698 nm **(c)**. All PSF are averaged over 10 individual points. Ideal theoretical PSFs are displayed in gray.

between both objectives. For objective I we find an increase at the first zeros [Fig. 5.6(b)]. Defocus can be the origin of the enlargement. Similar to the blue wavelengths, the positioning of the target in the focal point is not ideal. The point-spread function for objective II converges better to the theory curve, pointing to more precise adjustment of the focus [Fig. 5.7(b)]. We measure a very uniform FWHM of 564 nm for objective I and 561 nm for objective II with a deviation of $\sim$5 % from the ideal value.
For the main addressing wavelength at 698 nm we obtain a very good agreement with the theoretical predictions. The PSF for objective I shows almost no deviation from the theory curve [Fig. 5.6(c)]. We measure close to diffraction-limited performance. The FWHM for objective one is 533 nm. For the second objective we achieved a FWHM of 565 nm. We achieve a agreement with the ideal value within 4 %. This PSF includes a small defocus and a comatic artifact [Fig. 5.7(c)].
In summary, we find an agreement of better than 5 % between the ideal point spread functions and our measured resolution for the red wavelengths. Only for the short imaging wavelength at 461 nm our method seems to be limited by the finite extent of the targets. Overall, we find close to diffraction-limited performance for both objectives at all wavelengths of interest.

5.5 Comparison

Since we are building the first strontium quantum gas microscope, we can not compare our findings to an already existing experiment. But throughout the last years many new microscopes for various different species have been constructed. Figure 5.8 shows the imaging properties of some of them. At first we compare the numerical aperture [Fig. 5.8(a)]. Our NA is lower than for most quantum gas microscopes, the science cavity generating the xy-optical lattices in our experiment limits the minimal distance between the atoms and the objective. This constraint sets an upper bound on the numerical aperture in our setup. The MIT ^{40}K, Harvard ^{6}Li and Harvard ^{87}Rb experiments e.g. only have $\sim$ 100 μm between the location of the atoms and their first objective lens [12, 71, 41]. This technique enables a numerical aperture of up to 0.9.
Since strontium has an imaging wavelength at 461 nm, the FWHM for the imaging PSF is substantially lower compared to the alkali quantum gas microscopes, despite the lower NA [Fig. 5.8(b)]. Currently, only the ytterbium experiments have a shorter wavelength for imaging. The ratio between the FWHM of the ideal and measured PSF for all listed experiments is above one [Fig. 5.8(c)]. This indicates that all setups exhibit close to diffraction-limited performance for their objectives. For a more realistic picture of what resolution is required in each quantum gas microscope, we compute the achieved FWHM of the imaging wavelength and the ratio to the optical lattice spacing. Half of the displayed experiments reach a ratio lower than one. In these experiments, PSF from different lattice sites can be clearly distinguished with the microscopes. For our primary imaging lattice wavelength of 914 nm we achieve a ratio of 0.91. This value should enable single site imaging of strontium atoms in an optical lattice.

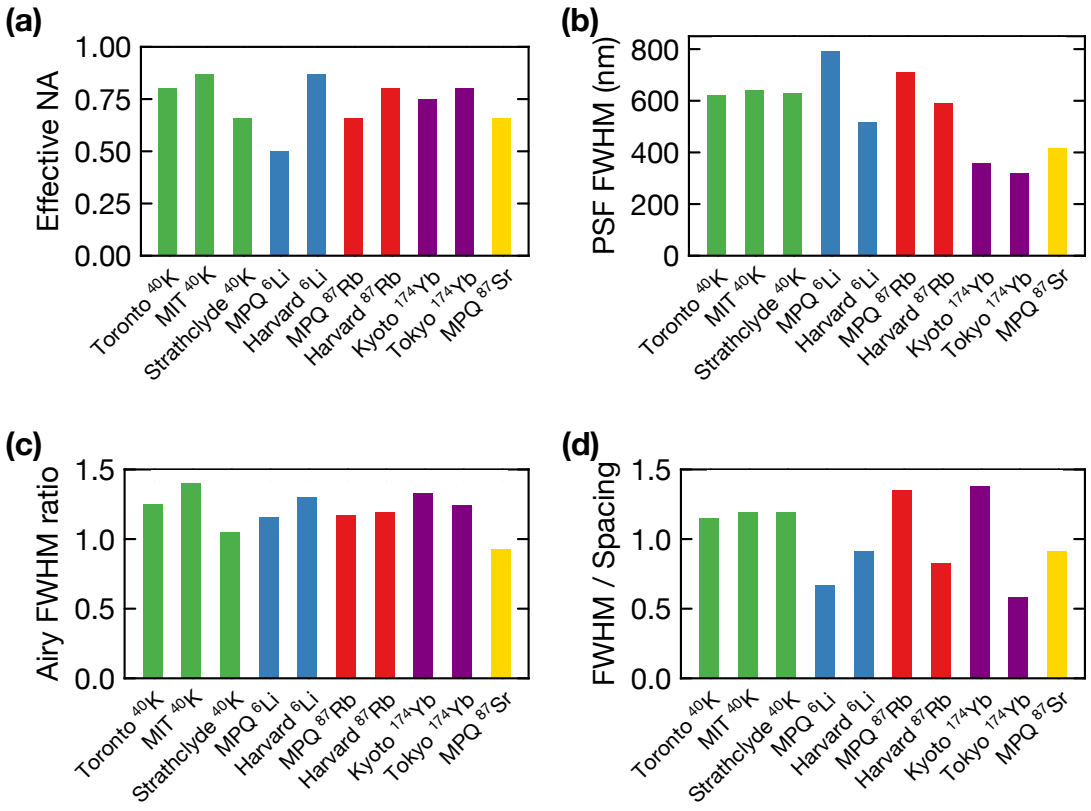

Fig. 5.8 Comparison of Quantum Gas Microscopes. **(a)** Our effective NA is lower than most quantum gas microscopes, since our science cavity limits the minimal distance between atoms and objective. **(b)** We have a lower PSF FWHM, because strontium has a short blue imaging wavelength at 461 nm. **(c)** All experiments achieve close to diffraction-limited performance for their objectives indicated by the ratio between the theoretical Airy pattern and the measured FWHM of the PSFs. **(d)** A comparison between the FWHM and the optical lattice spacing reveals a similar ratio compared to other experiments. Data taken from: Toronto $^{40}\mathrm{K}$ [70], MIT $^{40}\mathrm{K}$ [71], Strathclyde $^{40}\mathrm{K}$ [72], MPQ $^{6}\mathrm{Li}$ [42], Harvard $^{6}\mathrm{Li}$ [41], MPQ $^{87}\mathrm{Rb}$ [11], Harvard $^{87}\mathrm{Rb}$ [12], Kyoto $^{174}\mathrm{Yb}$ [73], Tokyo $^{174}\mathrm{Yb}$ [74].

5.6 Outlook

The first characterization of the objectives shows good agreement between the specified and measured data. It also matches the theoretical model to a large extent. Since microscope objective I exhibits a higher transmission of blue light and a higher reflection for the lattice wavelengths it is superior according to this test. In addition, we also find a slightly smaller point spread function for objective I at 461 nm and 698 nm. Therefore

we will use objective I for our main experiment.
Comparing with existing quantum gas microscopes we find similar imaging properties. This serves as a good starting point for designing the high resolution imaging system for single site imaging and addressing of strontium atoms.

Chapter 6

Interferometric Characterization of Wavefront Distortion

The previous characterization offers a lot of insight into the imaging properties of the objectives, but it only lets us measure the PSF locally. For imaging 200×200 lattice sites, we would like to know the continuous resolution quality over the full 100 μm field of view of the objective. Also for addressing on the ${}^1\mathrm{S}_0 \rightarrow {}^3\mathrm{P}_0$ clock transition we would like to have a flat wavefront in the focal plane. If one e.g. wants to create a coherent superposition between multiple strontium atoms at different locations, spatial phase shifts in the addressing beam need to be minimized. Otherwise the multi-particle state will dephase quickly.
Therefore we develop a method that allows us to determine the wavefront distortion over the whole field of view. This technique is based on an interferometric characterization of the wavefront distortion induced by the microscope objective.
To start this chapter we give a short introduction into interferometry. We follow with a description of a *Michelson interferometer*, which we use to characterize the coherence length of a light source. We outline our method and test it on a low NA *Fizeau interferometer*. Finally, we report on our progress in measuring the wavefront distortion of the objective. We analyze the calculated phase map and draw conclusions for the remaining optical aberrations present in the objective.

6.1 Interferometry

In spite of interferometry being a very old tool [75], it is still an actively used technique. Today, km-long interferometers can measure the distortion of space induced by a gravitational wave. This change in length is on the order of 1/1000 of the radius of a proton. There are many different types of interferometers but the working principle is always the same. A light wave is split into two waves at a beam splitter [Fig. 6.1(b)]. Each wave travels over a fixed distance before it is are redirected to a beam splitter where both waves are recombined into one wave again. Mathematically, we can express the two waves as

$$U_1 = \sqrt{I_0}\exp(-ikz), \tag{6.1}$$

$$U_2 = \sqrt{I_0}\exp(-ik(z-d)). \tag{6.2}$$

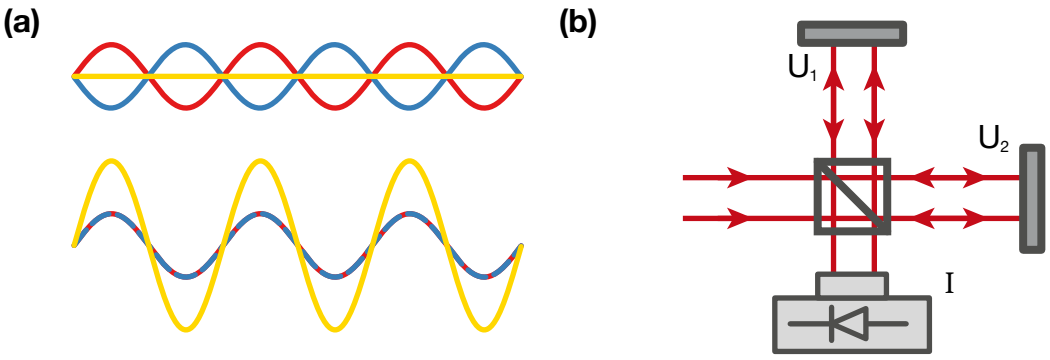

Fig. 6.1 Interferometer. (a) When two light waves have a π-phase shift they interfere destructively. If the waves are in phase the interfere constructively. **(b)** Simplified setup of an interferometer.

We assumed both interferometer arms have the same intensity I_0. Here $k = 2\pi/\lambda$ stands for the wavevector of the light and d for the path difference between the two arms. For the resulting intensity pattern after recombination we find

$$I = 2I_0 \left[1 + \cos\left(2\pi \frac{d}{\lambda}\right)\right]. \tag{6.3}$$

In addition, we write the phase difference between the two light waves as $\varphi = kd = 2\pi d/\lambda$. Since d/λ can be easily on the order of 10^7 a tiny change in d can already result in a detectable phase shift. Equation (6.3) recreates the familiar behavior of constructive and destructive interference [Fig. 6.1(a)]. For a path difference of odd-multiples of half the wavelength $(2\mathrm{m}+1)\lambda/2$ we find destructive interference, and for even-multiples $(2\mathrm{m})\lambda/2$ constructive interference can be observed.
With this basic introduction into interferometry we can now focus on the real implementation to measure our wavefront distortion.

6.2 Tuneable Coherence Length

For the distortion measurement, we are interested in characterizing the interference between a reference beam and a specific surface of the objective. Since the objective has six different lenses inside, there are 12 surfaces where light can interfere. A common strategy to suppress these unwanted interferences is to use a light source with a small *coherence length*. The coherence length is defined as the distance, over which a light source exhibits a perfect sine wave. Two light waves in an interferometer can now only interfere when the path difference is smaller than their coherence length. For our purposes we therefore need a light source with a coherence length below the typical surface distance of ~ 1 mm in our objective. This can eliminate the additional interference between the

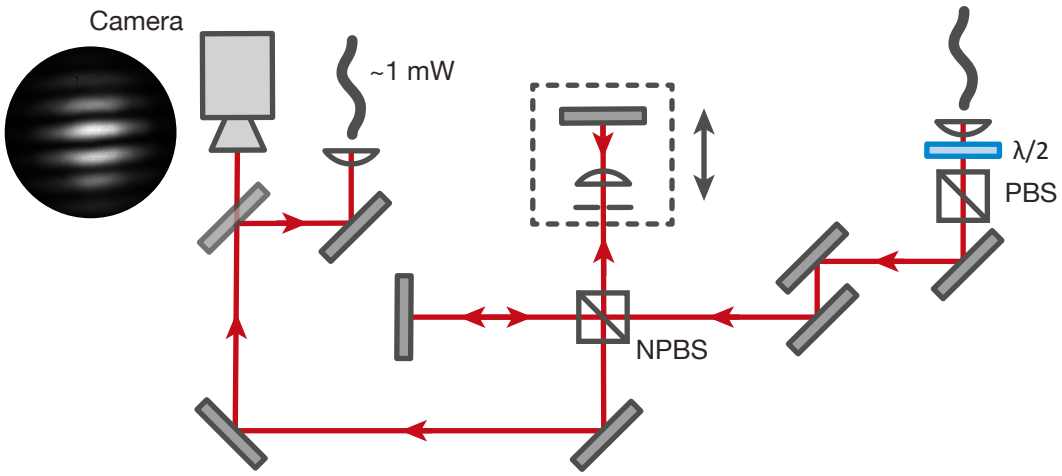

Fig. 6.2 Michelson interferometer. The interferometer creates a delay line, with which we can measure the coherence length of the light source. We can also use this setup as a delay line that creates a tuneable coherence revival in the outgoing beam.

lenses. We can also relate the coherence length L_c to the spectral width (linewidth) $\Delta\nu$ of the light source

$$\frac{L_c}{c} = \frac{1}{\Delta\nu}. \tag{6.4}$$

Here c is the speed of light in vacuum. It turns out that a typical solid state laser with a linewidth of ∼1 MHz already has a coherence length of ∼300 m. Therefore we have built an incoherent light source. It consists of an injection lock module [Fig. 3.11(a)] and an anti-reflection coated diode. We applied no seed light to the injection lock to prevent the diode from lasing. Since anti-reflection coated diodes are optimized to suppress the internal cavity in the diode, the light source should not lase. We therefore should observe a broad emission spectrum also at high diode currents. Fig. 6.3(a) shows our characterization of the optical output power. In contrast to the laser described in Ch. 3, the output power exhibits no sharp threshold. Fig. 6.3(a) displays a rather smooth increase in power. we conclude, that our anti-reflection coated diode does not lase at high currents.

To quantify the resulting coherence length of our light source, we send the light into a Michelson interferometer [Fig. 6.2]. The light is first polarization-cleaned and is then split into the two interferometer arms at an non polarizing beam splitter (NPBS). We can vary the optical path length of one of the arms with a translation stage. After the two light waves are recombined at the NPBS we direct the combined wave either to a camera or into an optical fiber. For the coherence length measurement, we observe fringes on the camera [Fig. 6.2]. By varying the path length of the second arm we change the path difference. We measure the distance over which we can identify a fringe pattern on the camera for different diode currents. The results are shown in Fig. 6.3(b-f) (second values for L_c). Around 60 mA, when the optical power increases, we can tune the coherence

length on the 100 μm scale. In the low current regime L_c is too short to observe fringes over any significant change in the path length. At very high currents the coherence length becomes long enough, such that other optical components in the interferometer start to interfere.
To confirm our findings we also measured the optical spectrum of the diode at each current with an optical spectrum analyzer. From a Lorentzian fit we can determine the spectral width $\Delta\nu$ at different currents. With Eq. (6.4) we calculate the equivalent coherence length. For lower currents, the directly measured and the value obtained from the spectrum agree within a few μm. At higher currents additional peaks appear in the spectrum. The fit can not fully account for them and the calculated coherence length therefore starts to deviate from the direct measurement. For all following experiments we run the diode at 60 mA with a coherence length of 150 μm.
With this measurement we characterized a light source that can provide light with low enough coherence length to suppress unwanted inteference between different surfaces in the objective.

6.3 Low NA Fizeau Interferometer

Before we measure the actual wavefront distortion of the real objective we test our method with a simplified test setup [Fig. 6.4]. This setup is arranged in a Fizeau-type interferometer. We now couple the light from the Michelson interferometer into an optical fiber and transport it to the Fizeau setup. There the light is polarization-cleaned. A *pellicle* beam splitter splits the light into two waves. One of the waves is dumped in a beam dump. The other is sent through two wedged windows before it is also dumped. The windows are placed a distance d apart from each other. The back-reflections from both windows are sent back to the pellicle and recombined on a camera. Since each wedged window has two surfaces we see in total 4 reflections on the camera. By compensating the optical path difference between the windows with the path delay in the Michelson interferometer we observe a fringe pattern between two back reflections over the coherence length of the light source [Fig. 6.4]. Depending on which reflections should interfere the increase in path length through the 5 mm thick window glass needs to accounted for.
We clearly see that by tuning the path difference in the Michelson interferometer we create a delay line, with which we can scan through the interference of different surfaces in a Fizeau interferometer.

6.4 Microscope Interferometry

The final optical setup to determine the wavefront distortion of the microscope objective is a *Twyman-Green interferometer*. Similar to the test setup we guide the light from the Michelson interferometer with an optical fiber to the microscope setup [Fig. 6.5]. At first

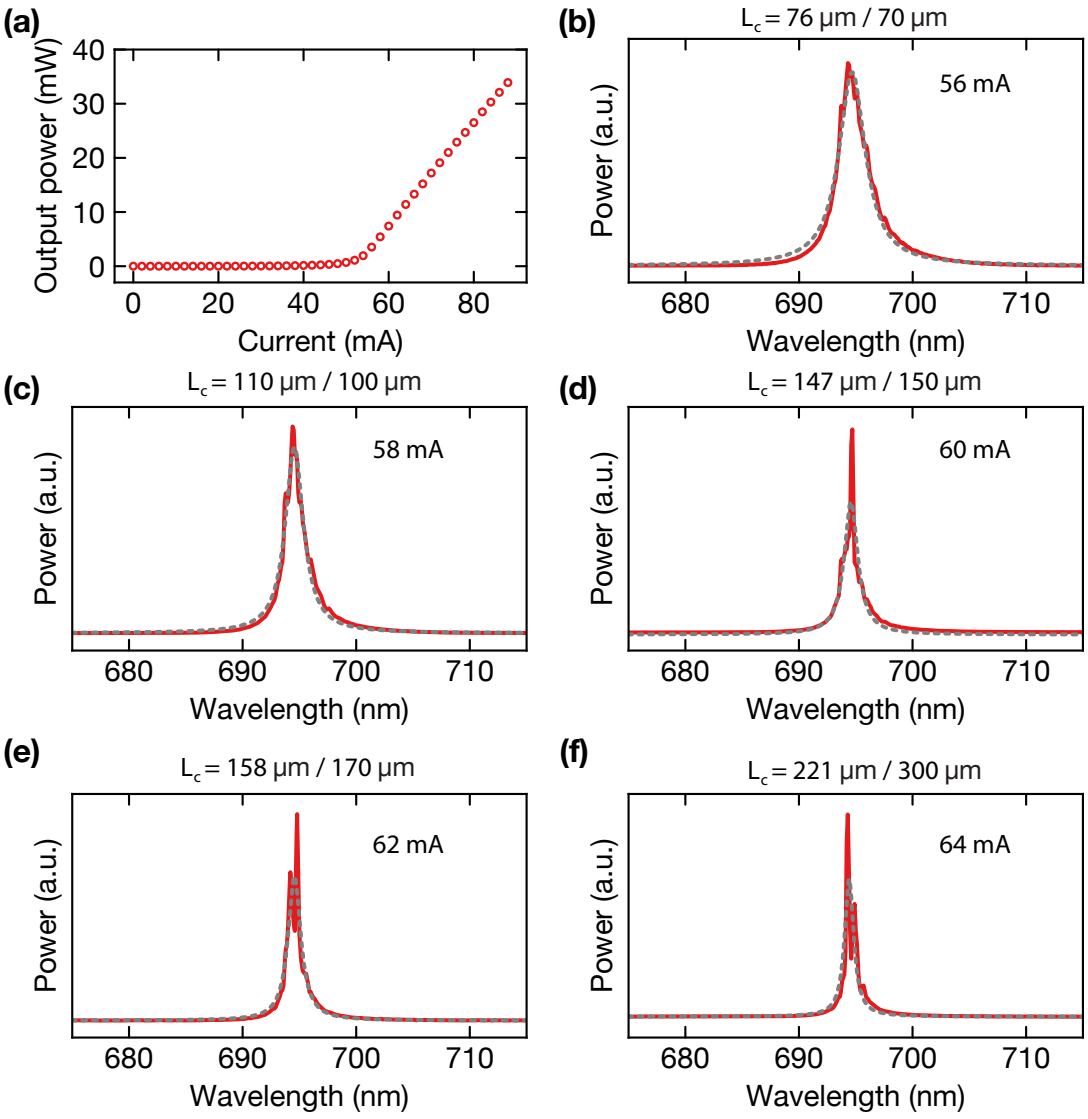

Fig. 6.3 Output power and Coherence length. (a) The output power for different diode currents is displayed. Even for high currents the diode does not lase. **(b-f)** We measured the coherence length for different diodes currents with the Michelson interferometer (right value). To evaluate this measurement we also measured the emission spectra. From a Lorentzian fit we obtain the coherence length of each spectrum (left value).

the light is polarization-cleaned and the beam waist amplified with a telescope to fill the full 35 mm free aperture of the objective. We split the light into two waves with a non polarizing beam splitter plate (*Thorlabs BSW 16*). The first interferometer arm is our reference beam. The path length of this arm can be varied in few-nm steps. For this precision we mounted the mirror back-reflecting the light on a 3-axis piezo mirror mount. In

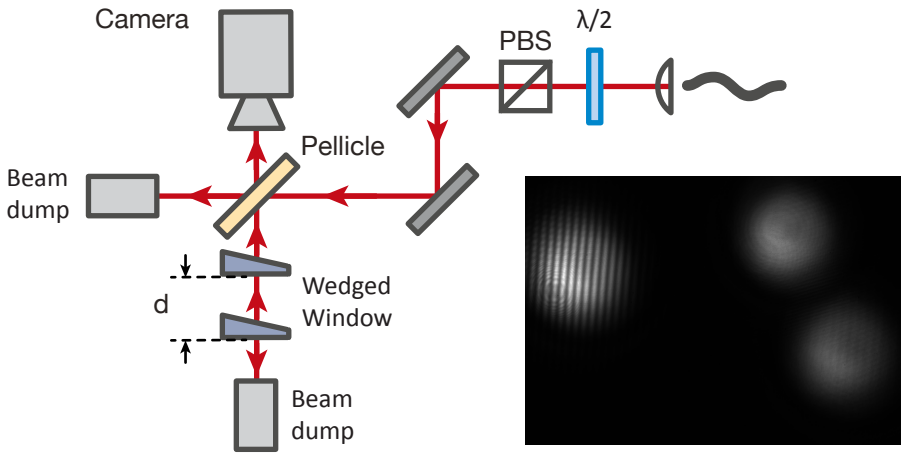

Fig. 6.4 Low NA test setup. To test the delay line we built a Fizeau interferometer. The light is split at a pellicle beam splitter before the four back reflections from two wedged windows are recombined and sent on a camera. When the path differences in the delay line setup matches the distance d between the windows interference can be observed. The inset shows the four back-reflections Two of them interfere.

the second interferometer arm we installed the objective. Since the wavefront behind the objective is spherical we also need a spherical surface from which the light can be back reflected. For this purpose we installed a Si_3N_4-sphere (*BOCA bearing company SI3N4 Ball Grade 3*) in the the focus. An additional window emulates the bucket window. Light back-reflected form the sphere then passes the objective again. It is interfered with the reference beam at the beam splitter. Another telescope shrinks the beam size again to be fully displayed on a camera.
Once we have aligned the setup we optimize the position of the sphere. The sphere should be ideally placed such that the wavefront curvature matches exactly the curvature of the sphere. For fine adjustment, the sphere is mounted on a 3-axis translation stage. From the interference between the objective arm with the reference beam we observe concentric rings on the camera [Fig. 6.5]. If we move the sphere along the optical axis, the number of rings visible increases or decreases depending on whether we move towards or away from the curvature matching point. A displacement radial to the optical axis results in a deformation of the rings. For a correct alignment of the sphere a symmetric shape with no rings can be observed.
This setup is the starting point for our wavefront distortion measurement. Since we would like to detect small phase shifts, attention was paid to only use high quality optics with high surface flatness and low wavefront distortion.

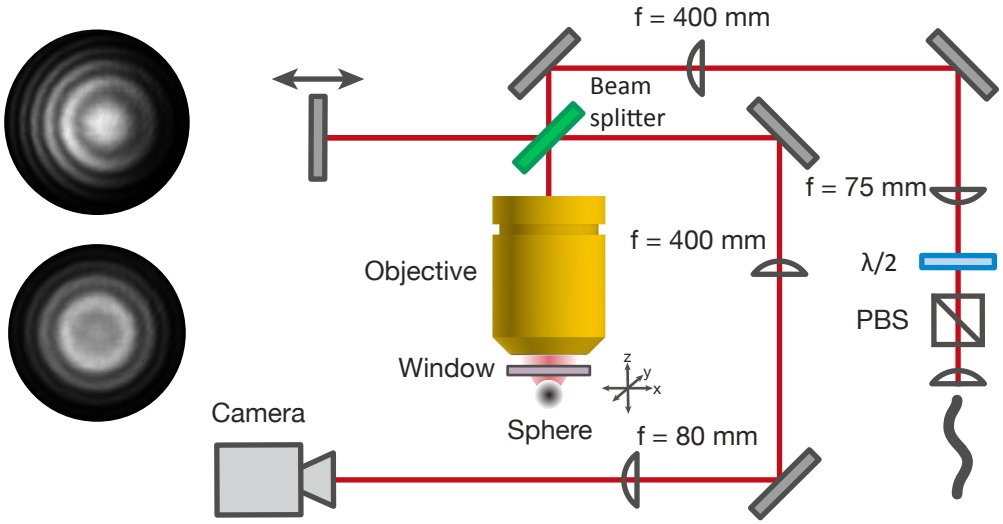

Fig. 6.5 Microscope interferometer. The beam diameter is increased with a telescope to match the back aperture of the objective. The light is split into a reference beam and the objective arm at a beam splitter. The length of the reference beam can be controlled with a piezo stage. In the objective arm the spherical wavefront after the objective is back-reflected from a Si_3N_4 sphere to match the wavefront curvature. After both arms are recombined at the beam splitter the beam is demagnified and sent on a camera. If the sphere is placed off-axis deformed rings can be seen. At a matching curvature between the wavefront and the sphere all additional rings vanish.

6.5 Phase Map and Objective Aberrations

With the microscope interferometer [Fig. 6.5] we can now determine the wavefront distortion induced by the objective. To extract the necessary phase map, it is not enough to look at a single fringe pattern. We rather want to observe how this fringe pattern changes, when we vary the optical path length of the reference beam. From this change we can then extract the phase of the wavefront at each point.
For a quantitative analysis of the fringe patterns, we can describe the wavefront of the reference beam and after the objective as

$$E_{\text{ref}} = A \cdot \exp\left(i\frac{2\pi}{\lambda}z\right), \tag{6.5}$$

$$E_{\text{objective}} = A \cdot \exp\left(i\frac{2\pi}{\lambda}(z + \Delta\varphi)\right). \tag{6.6}$$

In analogy to our earlier discussion of a Michelson interferometer we can express the resulting intensity pattern of the two interfering waves as

$$I(x,y) = I_0 + a(x,y)\exp\left[i\left(\frac{4\pi}{\lambda} + \Delta\varphi\right)\right]. \tag{6.7}$$

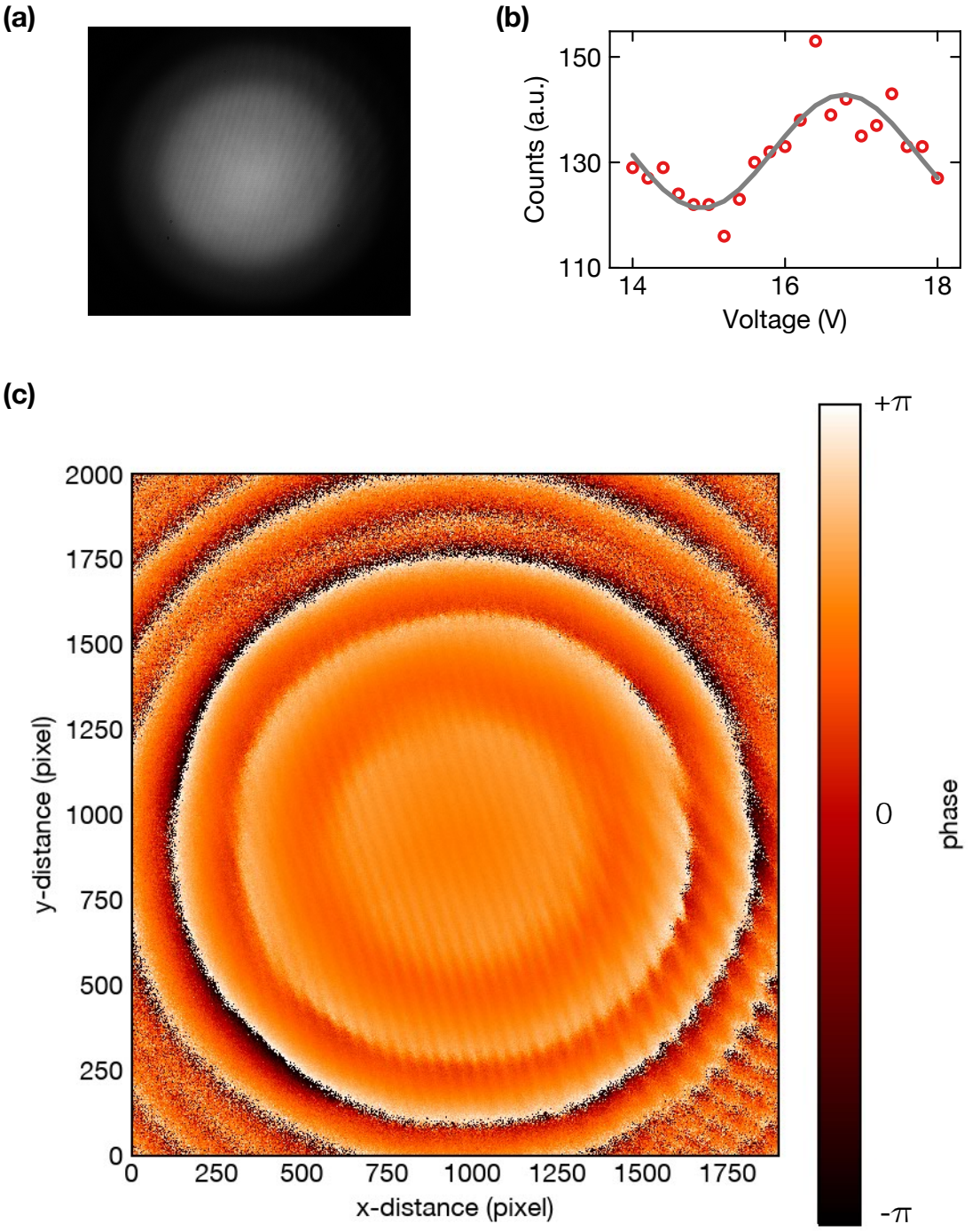

Fig. 6.6 Phase map. (a) To obtain the phase shift we measure the interference pattern for different optical path lengths. **(b)** To extract the phase at each pixel we correlate the data with a test function (gray). **(c)** The phase map shows three concentric rings which could indicate a residual defocus and spherical aberrations.

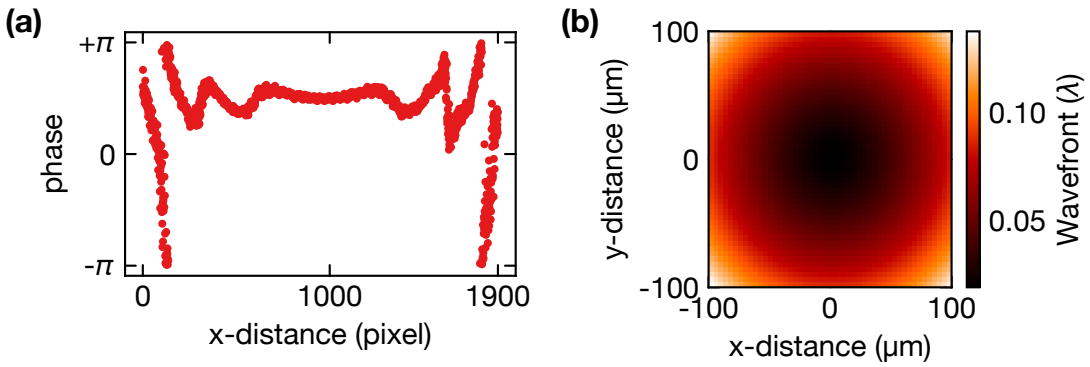

Fig. 6.7 Phase map cut. (a) A cut through the center of the phase map reviles a parabolic shape in the center. This can be an indication for defocus. In addition, also a forth order polynomial shape could be present in the system, pointing to a spherical aberration. **(b)** The simulated wavefront distortion for 698 nm in the focal plane of the objective shows wavefront distortions below 0.15 λ.

We see that the intensity profile dependence on the position, the wavelength of the light λ and the acquired phase shift $\Delta\varphi$. Since we measure only a certain intensity at each point, we can not obtain the phase $\Delta\varphi$ from Eq. (6.7) with a single measurement. To circumvent this issue the intensity profile is obtained for different path lengths between the two interferometer arms. We can then observe a periodic signal in each point [Fig. 6.6(b)]. Correlating this signal with a test function of the from

$$T = a \cdot \exp\left(i\frac{4\pi}{\lambda}z\right) \tag{6.8}$$

gives us the correlation function

$$C = \sum_{ij} I_{ij} T^*_{ij} \,. \tag{6.9}$$

Then, we find the final phase at each position by taking the argument of the correlation function, $\Delta\varphi = arg(C)$. As a phase shift of π corresponds to a wavefront distortion of $\lambda/2$, it is convenient to express our phases also in units of the wavelength λ.
In the microscope interferometer [Fig. 6.5] we vary the optical path length of the reference beam with the piezo translation stage. We made sure, that the mirror is moved orthogonally to the wavefront to not induce additional tilting. Figure 6.6(a) shows the resulting intensity pattern for a single measurement observed on the camera. We change the piezo voltage over 4 V to cover a full period of the underlying periodic signal.
Since we know the wavelength of the light, this give us enough information to extract the phase at each pixel with our correlation method. The final phase map can be seen in Fig. 6.6(c).
The phase map shows three concentric rings before the quality of the phase is reduced by noise. If we compare the extent of the phase map with the one of a single intensity

pattern, we find that at the noise region in the phase map, the intensity in the single measurement already nearly decreases to zero. Consequently, the phases in the outer region suffer from a major contribution of the noise floor. We also observe an additional fringe pattern at the lower right corner. Since the coherence length of the light source is only 150 μm, the secondary interference can not come from interference between two glass surfaces in the microscope. At the stage of writing this thesis the origin of the additional fringes ins unknown and needs further investigation.
To get a better understanding of the concentric rings we analyze a slice through the center of the phase map [Fig. 6.7(a)]. We find the expected symmetric shape from the rings. Starting from the middle, we encounter the two peaks from the first ring after $\sim$200 nm. The phase map has a parabolic shape between these two peaks. This could be an indication for residual defocus in the system since this aberration can be described by a parabola. Moving further outwards, two vales followed by the two peaks from the second ring are observed in the phase cut [Fig. 6.7(a)]. This shape could be reproduced by a forth order polynomial like spherical aberrations. If it is indeed the case that defocus and spherical aberrations are present in the system this can point to a slight displacement of the Si_3N_4-sphere. When the curvature of the wavefront and the sphere do not coincide, the reflected beam will be slightly focused or defocused after the microscope objective. This can result in concentric aberrations like defocus or spherical aberrations. Since the translation stage of the sphere only allows positioning within 500 nm steps, the phase shift due to displacement could only be reduced within 1.4 π respectively 0.7 λ. To achieve a performance of $\lambda/10$ typically specified for high quality optics the phase shift needs to be within 1/5 π which corresponds to a positioning of the sphere within 70 nm. With a piezo controlled translation stage for the sphere we could reach such a precision. Furthermore, we can compare our measured phase map to the simulated wavefront in the focal plane of the objective for a wavelength of 698 nm [Fig. 6.7(b)]. The simulated map also has a parabolic shape for the phase shifts. Indeed, here this shape comes from residual defocus and spherical aberrations with Zernike coefficients of -0.005 and 0.009 respectively. The simulated wavefront distortions are all below 0.15 λ. This supports our earlier suggestion that for a repeated measurement of the wavefront distortion the sphere should be placed on a piezo translation stage to enable fine adjustment of the positioning. Due to time constrains we were unable to repeat our measurement of the wavefront distortion. Nevertheless, with some minor improvements it should be possible to obtain a full phase map for the objective with our method. Beside a piezo translation stage for the sphere some improvements could also be made to the data analysis.
Since in general phase maps are smooth and the phase difference between two points is periodic, the phase is only defined on the interval $[-\pi, \pi]$ due to the argument operator on the phasor ($\Delta\varphi = arg(C)$). This means, that in order to extract the final phase map from our data we need to fold all the different phases back into the interval $[-\pi, \pi]$ by adding or subtracting multiples of 2π. This process is known as *phase unwrapping* [76]. In Figure 6.7(a) we already see at the corners that the phase increases strongly before it comes back. With a phase unwrapping algorithm we could fould these peaks back into the $[-\pi, \pi]$ interval.

Once a smooth phase map is achieved we could also fit Zernike polynomials to the map to obtain the different amplitudes for each residual optical aberration [15].

6.6 Outlook

We presented a method to characterize the wavefront distortion of a microscope objective. In addition we analyze our measured phase map and display a strategy to extract the optical aberrations in the system form our measurement. With small upgrades to the existing setup and a phase unwrapping algorithm it should be possible to extract the Zernike coefficients for all polynomials in the near future.

Chapter 7

Conclusion and Outlook

The main aim of this project was to construct and characterize a high resolution imaging system that is capable of imaging and addressing atoms confined in an optical lattice at the single site level.

In Ch. 5 we report on the characterization of two high resolution microscope objectives with a numerical aperture of $\mathrm{NA} = 0.66$. We first measure the reflectivity and transmission at the blue (461 nm) and red (689 nm) imaging wavelengths, the clock (698 nm) addressing wavelength and the two lattice wavelengths (813 nm and 1064 nm). The values for both objectives agree within less than 2 %. For the lattice wavelengths we adjusted the intensity sent on the objective to mimic that of a high power laser beam used in the experiment later on. We find 0.5 % differences in the reflectivity at 1064 nm. Objective I exhibits a higher reflection of 99.5 % and is therefore more suited for the experiment.
The resolution performance is characterized by measuring the point spread function of a point like target source [Ch. 5]. We receive close to diffraction-limited performance at 461 nm, 689 nm and 698 nm. The full width half maximum value of all point-spread functions except for the blue one agrees within less than 5 % with theoretical predictions for a point-like target. The blue curves show the strongest deviations from the ideal pattern of 15 %. This can be explained by the finite size of the target source. Objective I has a lower full width half maximum of 415 nm and 533 nm for both the blue imaging and the clock addressing wavelength at 461 nm and 698 nm respectively.
Since objective I is superior in both the reflection test and the resolution capabilities we will build this objective into the quantum gas microscope.

In the course of this thesis we designed and constructed a method for interferometrically determining the wavefront distortion induced by a microscope objective [Ch. 6]. We describe how a light source with tuneable coherence length can be built to supress unwanted interference in the wavefront measurement. With a Michelson interferometer the different values for the coherence length from $\sim$70-300 μm are confirmed. In a low NA test setup we use the Michelson interferometer as a delay line to distinguish between interference patterns of two wedged windows in a Fizeau interferometer. For obtaining the wavefront distortion the objective is built into a Twyman-Green interferomter. By interfering the light that is back reflected from a $\mathrm{Si_3N_4}$ sphere through the objective, with a reference beam we measure a full phase map.

We find evidence for residual defocus and spherical aberrations in the system. In addition, we lay out a strategy to improve the precision of the measurement and finally obtain the Zernike coefficients for the different optical aberrations.

In Ch. 3 we describe the design and construction of new lasers that are well isolated from external noise. Two lasers at the $^1\mathrm{S}_0 \rightarrow {}^3\mathrm{P}_0$ clock frequency are locked with a PDH-scheme to two different high finesse ULE cavities. To analyze the stability we measure the relative linewidth of both locked lasers with a heterodyne beat measurement. With this technique we can set an upper bound to the linewidth of each laser of 4(1) Hz. Additional observation of the beat signal in the time domain reveiled a coherence time of up to 4 s indicating a much narrower linewidth than obtained from the direct beat measurement.

A few future improvements of the cavity are necessary. Since we had to deal with pressure fluctuation and vacuum leakage of cavity I, we suggest to change this cavity housing from the aluminum to a steel box. This way already works for cavity II to eliminate vacuum problems. Moreover, the heaters inside the housing should be changed to vacuum compatible Peltier elements, because the old heaters were potentially outgassing and preventing us from actively temperature-stabilizing to the zero-crossing temperature. These updates should largely reduce the drift of the beat and enable a linewidth on the Hz-level for both lasers.
To eliminate noise induced by an optical fiber an active fiber-noise cancellation setup needs to be developed. With this setup the laser linewidth should be preserved in the fiber link to the main experiment.
Sending the light from the clock laser onto a spatial light modulator enables full control over the wavefront. This way, arbitrary addressing of sites in the optical lattices will become possible.

As a whole, we are confident that with the incorporation of the microscope objective into the experiment will enable single-site imaging in the near future and single-site addressing on the clock transition in the not so distant future.

Chapter 8

Appendix

Adapter Board Circuit

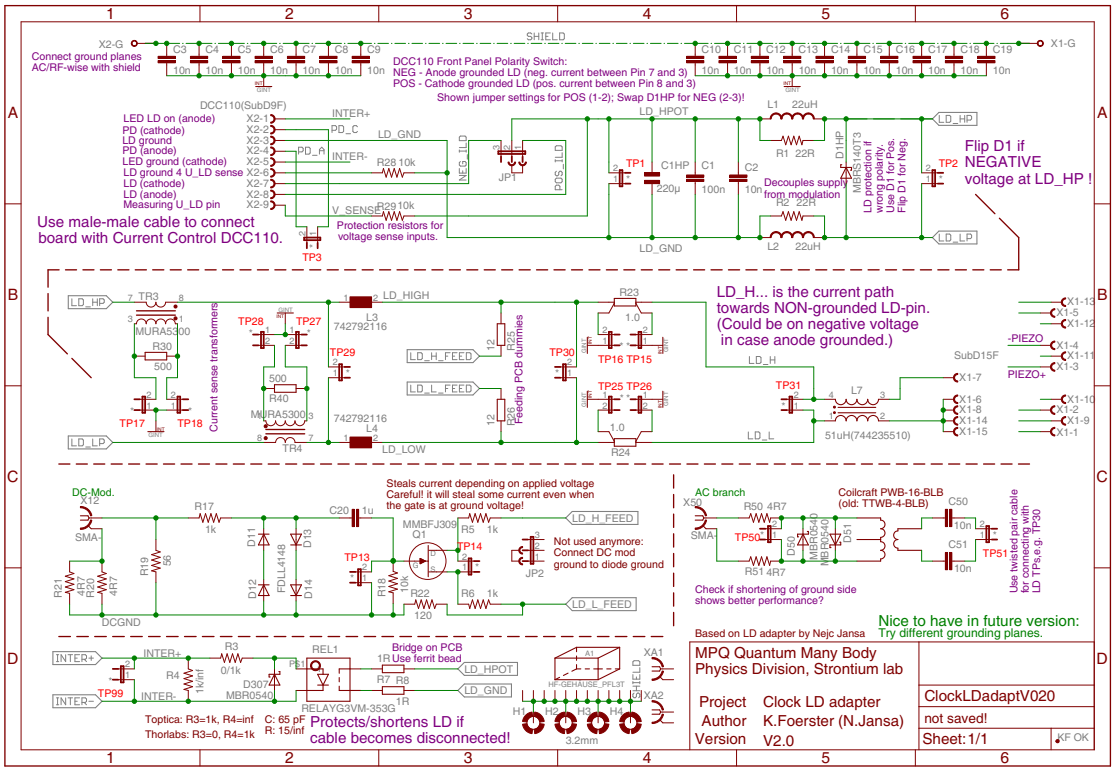

Fig. 8.1 Adapter Board Circuit. Circuit for monitoring and modulating the laser diode current. Electrical elements can be changed to filter noise to the laser current.

References

[1] A. W. Harrow and A. Montanaro. *Quantum computational supremacy*, Nature **549**, 203–209 (2017). DOI: 10.1038/nature23458.

[2] R. P. Feynman. *Simulating physics with computers*, International Journal of Theoretical Physics **21**, 467–488 (1982). DOI: 10.1007/BF02650179.

[3] P. A. Lee, N. Naoto, and W. Xiao-Gang. *Doping a Mott insulator: Physics of high-temperature superconductivity*, Reviews of Modern Physics **78**, 17–85 (2006). DOI: 10.1103/RevModPhys.78.17.

[4] J. Argüello-Luengo, A. González-Tudela, T. Shi, P. Zoller, and J. I. Cirac. *Analogue quantum chemistry simulation*, Nature **574**, 215–218 (2019). DOI: 10.1038/s41586-019-1614-4.

[5] I. Bloch, J. Dalibard, and S. Nascimbène. *Quantum simulations with ultracold quantum gases*, Nature Physics **8**, 267 (2012). DOI: 10.1038/nphys2259.

[6] R. Blatt and C. F. Roos. *Quantum simulations with trapped ions*, Nature Physics **8**, 277–284 (2012). DOI: 10.1038/nphys2252.

[7] J. Cai, A. Retzker, F. Jelezko, and M. B. Plenio. *A large-scale quantum simulator on a diamond surface at room temperature*, Nature Physics **9**, 168–173 (2013). DOI: 10.1038/nphys2519.

[8] A. Aspuru-Guzik and P. Walther. *Photonic quantum simulators*, Nature Physics **8**, 285–291 (2012). DOI: 10.1038/nphys2253.

[9] F. Arute *et al. Quantum Supremacy using a Programmable Superconducting Processor*, Nature **574**, 505–510 (2019). DOI: 10.1038/s41586-019-1666-5.

[10] D. Greif, M. F. Parsons, A. Mazurenko, C. S. Chiu, S. Blatt, F. Huber, G. Ji, and M. Greiner. *Site-resolved imaging of a fermionic Mott insulator*, Science **351**, 953–957 (2016). DOI: 10.1126/science.aad9041.

[11] J. F. Sherson, C. Weitenberg, M. Endres, M. Cheneau, I. Bloch, and S. Kuhr. *Single-atom-resolved fluorescence imaging of an atomic Mott insulator*, Nature **467**, 68–72 (2010). DOI: 10.1038/nature09378.

[12] W. S. Bakr, J. I. Gillen, A. Peng, S. Fölling, and M. Greiner. *A quantum gas microscope for detecting single atoms in a Hubbard-regime optical lattice*, Nature **462**., 74–77 (2009). DOI: 10.1038/nature08482.

[13] J. Koepsell, J. Vijayan, P. Sompet, F. Grusdt, T. A. Hilker, E. Demler, G. Salomon, I. Bloch, and C. Gross. *Imaging magnetic polarons in the doped Fermi–Hubbard model*, Nature **572**, 358–362 (2019). DOI: 10.1038/s41586-019-1463-1.

[14] C. Weitenberg, M. Endres, J. F. Sherson, M. Cheneau, P. Schauß, T. Fukuhara, I. Bloch, and S. Kuhr. *Single-spin addressing in an atomic Mott insulator*, Nature **471**, 319 (2011). DOI: 10.1038/nature09827.

[15] P. Zupancic, P. M. Preiss, R. Ma, A. Lukin, M. E. Tai, M. Rispoli, R. Islam, and M. Greiner. *Ultra-precise holographic beam shaping for microscopic quantum control*, Optics Express **24**., 13881 (2016). DOI: 10.1364/OE.24.013881.

[16] M. Greiner, O. Mandel, T. Esslinger, T. W. Hänsch, and I. Bloch. *Quantum phase transition from a superfluid to a Mott insulator in a gas of ultracold atoms*, Nature **415**, 39–44 (2002). DOI: 10.1038/415039a.

[17] A. D. Ludlow, M. M. Boyd, J. Ye, E. Peik, and P. O. Schmidt. *Optical atomic clocks*, Reviews of Modern Physics **87**, 637 (2015). DOI: 10.1103/RevModPhys.87.637.

[18] T. Bothwell, D. Kedar, E. Oelker, J. M. Robinson, S. L. Bromley, W. L. Tew, J. Ye, and C. J. Kennedy. *JILA Sr I optical lattice clock with uncertainty of 2.0 $\times$ 10^{-18}*, Metrologia **56**, 065004 (2019). DOI: 10.1088/1681-7575/ab4089.

[19] S. L. Campbell *et al. A Fermi-degenerate three-dimensional optical lattice clock*, Science **358**, 90–94 (2017). DOI: 10.1126/science.aam5538.

[20] A. Heinz. *Ultracold Strontium in State-Dependent Optical Lattices*, PhD Thesis Ludwig-Maximilian Universität München (2020). URL: https://ultracold.sr/publications/thesis_andre_heinz.pdf.

[21] A. Heinz, A. J. Park, N. Šantić, J. Trautmann, S. G. Porsev, M. S. Safronova, I. Bloch, and S. Blatt. *State-Dependent Optical Lattices for the Strontium Optical Qubit*, Physical Review Letters **124**, 203201 (2020). DOI: 10.1103/PhysRevLett.124.203201.

[22] A. González-Tudela and I. J. Cirac. *Non-Markovian Quantum Optics with Three-Dimensional State-Dependent Optical Lattices*, Quantum **2**, 97 (2018). DOI: 10.22331/q-2018-10-01-97.

[23] A. J. Daley. *Quantum computing and quantum simulation with group-II atoms*, Quantum Infromation Processing **10**, 865 (2011). DOI: 10.1007/s11128-011-0293-3.

[24] T. Nicholson *et al. Systematic evaluation of an atomic clock at 2 $\times$ 10^{-18} total uncertainty*, Nature Communications **6**, 6896 (2015). DOI: 10.1038/ncomms7896.

[25] A. Cooper, J. P. Covey, I. S. Madjarov, S. G. Porsev, M. S. Safronova, and M. Endres. *Alkaline-Earth Atoms in Optical Tweezers*, Physical Review X **8**, 041055 (2018). DOI: 10.1103/PhysRevX.8.041055.

[26] X. Xu, T. H. Loftus, J. L. Hall, A. Gallagher, and J. Ye. *Cooling and trapping of atomic strontium*, Journal of the Optical Society of America B **20**, 968 (2003). DOI: 10.1364/JOSAB.20.000968.

[27] J. A. Muniz, D. J. Young, J. R. K. Cline, and J. K. Thompson. *Cavity-QED determination of the natural linewidth of the ^{87}Sr millihertz clock transition with 30 µHz resolution*, arXiv: 2007.07855 (2020).

[28] J. E. Sansonettia and G. Nave. *Wavelengths, Transition Probabilities, and Energy Levels for the Spectrum of Neutral Strontium (Sr I)*, Journal of Physical and Chemical Reference Data **39**, 033103 (2010). DOI: 10.1063/1.3449176.

[29] M. Yasuda and H. Katori. *Lifetime Measurement of the $^3P_2$ Metastable State of Strontium Atoms*, Physical Review Letters **92**, 153004 (2004). DOI: 10.1103/PhysRevLett.92.153004.

[30] O. Onishchenko, P. Sergey, A. Urech, C.-C. Chen, S. Bennetts, G. A. Siviloglou, and F. Schreck. *Frequency of the ultranarrow $^1S_0$-$^3P_2$ transition in ^{87}Sr*, Physical Review A **99**, 052503 (2019). DOI: 10.1103/PhysRevA.99.052503.

[31] S. Falke *et al. A strontium lattice clock with 3×10^{-17} inaccuracy and its frequency*, New Journal of Physics **16**, 073023 (2014). DOI: 10.1088/1367-2630/16/7/073023.

[32] S. Snigirev, A. J. Park, A. Heinz, I. Bloch, and S. Blatt. *Fast and dense magneto-optical traps for strontium*, Physical Review A **99**, 063421 (2019). DOI: 10.1103/PhysRevA.99.063421.

[33] M. M. Boyd. *High Precision Spectroscopy of Strontium in an Optical Lattice: Towards a New Standard of Frequency and Time*, PhD Thesis University of Colorado (2007). URL: https://jila.colorado.edu/sites/default/files/2019-05/boyd_thesis.pdf.

[34] S. G. Porsev and A. Derevianko. *Hyperfine quenching of the metastable $^3P_{0,2}$ states in divalent atoms*, Physical Review A **69**, 042506 (2004). DOI: 10.1103/PhysRevA.69.042506.

[35] M. S. Safronova, Z. Zuhrianda, U. I. Safronova, and C. W. Clark. *Extracting transition rates from zero-polarizability spectroscopy*, Physical Review A **92**, 040501 (2015). DOI: 10.1103/PhysRevA.92.040501.

[36] R. Grimm, M. Weidemüller, and Y. B. Ovchinnikov. *Optical Dipole Traps for Neutral Atoms*, Advances In Atomic, Molecular, and Optical Physics **42**, 95 (2000). DOI: 10.1016/S1049-250X(08)60186-X.

[37] H. Katori, K. Hashiguchi, E. Y. Il'inova, and V. D. Ovsiannikov. *Magic Wavelength to Make Optical Lattice Clocks Insensitive to Atomic Motion*, Physical Review Letters **103**, 153004 (2009). DOI: 10.1103/PhysRevLett.103.153004.

[38] *Fundamentals of photonics*. B. E. A. Saleh and M. C. Teich, Wiley, 2007. ISBN: 978-1-119-50687-4.

[39] R. Haindl. *A Clock Laser System for Quantum Simulations with Ultracold Strontium Atoms*, Master Thesis Ludwig-Maximilian Universität München (2019). URL: https://ultracold.sr/publications/thesis_rudolf_haindl.pdf.

[40] A. Mazurenko, C. S. Chiu, G. Ji, M. F. Parsons, M. Kanász-Nagy, R. Schmidt, F. Grusdt, E. Demler, D. Greif, and M. Greiner. *A cold-atom Fermi–Hubbard antiferromagnet*, Nature **545**, 462–466 (2017). DOI: 10.1038/nature22362.

[41] M. F. Parsons, F. Huber, A. Mazurenko, C. S. Chiu, W. Setiawan, K. Wooley-Brown, S. Blatt, and M. Greiner. *Site-Resolved Imaging of Fermionic ^{6}Li in an Optical Lattice*, Physical Review Letters **114**, 213002 (2015). DOI: 10.1103/PhysRevLett.114.213002.

[42] A. Omran, M. Boll, T. A. Hilker, K. Kleinlein, G. Salomon, I. Bloch, and C. Gross. *Microscopic Observation of Pauli Blocking in Degenerate Fermionic Lattice Gases*, Physical Review Letters **115**, 263001 (Dec. 2015). DOI: 10.1103/PhysRevLett.115.263001.

[43] K. Shibata, R. Yamamoto, Y. Seki, and Y. Takahashi. *Optical spectral imaging of a single layer of a quantum gas with an ultranarrow optical transition*, Physical Review A **89**, 031601 (2014). DOI: 10.1103/PhysRevA.89.031601.

[44] M. Cheneau, P. Barmettler, D. Poletti, M. Endres, P. Schauß, T. Fukuhara, C. Gross, I. Bloch, C. Kollath, and S. Kuhr. *Light-cone-like spreading of correlations in a quantum many-body system*, Nature **481**, 484–487 (2012). DOI: 10.1038/nature10748.

[45] T. A. Hilker, G. Salomon, F. Grusdt, A. Omran, M. Boll, E. Demler, I. Bloch, and C. Gross. *Revealing hidden antiferromagnetic correlations in doped Hubbard chains via string correlators*, Science **357**, 484–487 (2017). DOI: 10.1126/science.aam8990.

[46] M. Boll, T. A. Hilker, G. Salomon, A. Omran, J. Nespolo, L. Pollet, I. Bloch, and C. Gross. *Spin-and density-resolved microscopy of antiferromagnetic correlations in Fermi-Hubbard chains*, Science **353**, 1257–1260 (2016). DOI: 10.1126/science.aag1635.

[47] P. Schauß, M. Cheneau, M. Endres, T. Fukuhara, S. Hild, A. Omran, T. Pohl, C. Gross, S. Kuhr, and I. Bloch. *Observation of spatially ordered structures in a two-dimensional Rydberg gas*, Nature **491**, 87–91 (2012). DOI: 10.1038/nature11596.

[48] D. Barredo, V. Lienhard, S. de Léséleuc, T. Lahaye, and A. Browaeys. *Synthetic three-dimensional atomic structures assembled atom by atom*, Nature **561**, 79–82 (2018). DOI: 10.1038/s41586-018-0450-2.

[49] E. Oelker *et al. Demonstration of 4.8×10^{17} stability at 1 s for two independent optical clocks*, Nature Photonics **13**, 714–719 (2019). DOI: 10.1038/s41566-019-0493-4.

[50] W. R. Milner *et al. Demonstration of a Timescale Based on a Stable Optical Carrier*, Physical Review Letters **123**, 173201 (2019). DOI: 10.1103/PhysRevLett.123.173201.

[51] E. Staub. *Developing a High-Flux Atomic Beam Source for Experiments with Ultracold Strontium Quantum Gases*, Master Thesis Ludwig-Maximilian Universität München (2019). URL: https://ultracold.sr/publications/thesis_etienne_staub.pdf.

[52] Toptica-website and personal communication with engineer. URL: https://www.toptica.com/fileadmin/Editors_English/11_brochures_datasheets/01_brochures/toptica_BR_Scientific_Lasers.pdf (visited on 07/15/2020).

[53] E. A. Donley, T. P. Heavner, F. Levi, M. O. Tataw, and S. R. Jefferts. *Double-pass acousto-optic modulator system*, Review of Scientific Instruments **76**, 063112 (2005). DOI: 10.1063/1.1930095.

[54] S. H. Wissenberg. *Stabilizing diode lasers to an ultrastable reference cavity*, Master Thesis Ludwig-Maximilian Universität München (2017). URL: https://ultracold.sr/publications/thesis_stephan_wissenberg.pdf.

[55] E. D. Black. *An introduction to Pound–Drever–Hall laser frequency stabilization*, American Journal of Physics **69**, 79 (2001). DOI: 10.1119/1.1286663.

[56] P. Gallion and G. Debarge. *Quantum phase noise and field correlation in single frequency semiconductor laser systems*, IEEE Journal of Quantum Electronics **20**, 343–349 (1984). DOI: 10.1109/JQE.1984.1072399.

[57] L.-S. Ma, P. Jungner, J. Ye, and J. L. Hall. *Delivering the same optical frequency at two places: accurate cancellation of phase noise introduced by an optical fiber or other time-varying path*, Optics Letters **19**, 1777–1779 (1994). DOI: 10.1364/OL.19.001777.

[58] T. Udem, R. Holzwarth, and T. W. Hänsch. *Optical frequency metrology*, Nature **416**, 233–237 (2002). DOI: 10.1038/416233a.

[59] A. Fleming. *On the antibacterial action of cultures of a Penicillium, with special reference to their use in the isolation of B. influenzae*, The British Journal of Experimental Pathology **10**, 226–236 (1929).

[60] G. McConnell, J. Trägårdh, R. Amor, J. Dempster, E. Reid, and W. B. Amos. *A novel optical microscope for imaging large embryos and tissue volumes with sub-cellular resolution throughout*, eLife **5**, e18659 (2016). DOI: 10.7554/eLife.18659.

[61] S. W. Hell and J. Wichmann. *Breaking the diffraction resolution limit by stimulated emission: stimulated-emission-depletion fluorescence microscopy*, Optics Letters **19**, 780–782 (1994). DOI: 10.1364/OL.19.000780.

[62] E. Betzig, J. K. Trautman, T. Harris, J. Weiner, and R. Kostelak. *Breaking the diffraction barrier: optical microscopy on a nanometric scale*, Science **251**, 1468–1470 (1991). DOI: 10.1126/science.251.5000.1468.

[63] M. J. Rust, M. Bates, and X. Zhuang. *Sub-diffraction-limit imaging by stochastic optical reconstruction microscopy (STORM)*, Nature Methods **3**, 793–796 (2006). DOI: 10.1038/nmeth929.

[64] E. Abbe. *Beiträge zur Theorie des Mikroskops und der mikroskopischen Wahrnehmung*, Archiv für Mikroskopische Anatomie **9**, 413–468 (1873). DOI: 10.1007/BF02956173.

[65] E. Betzig, G. H. Patterson, R. Sougrat, O. W. Lindwasser, S. Olenych, J. S. Bonifacino, M. W. Davidson, J. Lippincott-Schwartz, and H. F. Hess. *Imaging intracellular fluorescent proteins at nanometer resolution*, Science **313**, 1642–1645 (2006). DOI: 10.1126/science.1127344.

[66] *Advanced Optical Imaging Theory*. Min Gu, Springer, 2000. ISBN: 978-3-540-48471-4.

[67] G. Vicidomini. *Three-Dimensional Image Restoration in Fluorescence Microscopy*, PhD Thesis Istituto Italiano di Tecnologia (2008). DOI: 10.13140/RG.2.1.1784.0728.

[68] *Handbook of Optical Systems*. Herbert Gross, Wiley-VCH, 2007. ISBN: 978-3527403790.

[69] P. Schauß. *High-resolution imaging of ordering in Rydberg many-body systems*, PhD Thesis Ludwig-Maximilian Universität München (2014). URL: https://edoc.ub.uni-muenchen.de/18152/1/Schauss_Peter.pdf.

[70] G. J. A. Edge, R. Anderson, D. Jervis, D. C. McKay, R. Day, S. Trotzky, and J. H. Thywissen. *Imaging and addressing of individual fermionic atoms in an optical lattice*, Physical Review A **92**, 063406 (2015). DOI: 10.1103/PhysRevA.92.063406.

[71] L. W. Cheuk, M. A. Nichols, M. Okan, T. Gersdorf, V. V. Ramasesh, W. S. Bakr, T. Lompe, and M. W. Zwierlein. *Quantum-Gas Microscope for Fermionic Atoms*, Physical Review Letters **114**, 193001 (2015). DOI: 10.1103/PhysRevLett.114.193001.

[72] E. Haller, J. Hudson, A. Kelly, D. A. Cotta, B. Peaudecerf, G. D. Bruce, and S. Kuhr. *Single-atom imaging of fermions in a quantum-gas microscope*, Nature Physics **11**, 738–742 (2015). DOI: 10.1038/nphys3403.

[73] R. Yamamoto, J. Kobayashi, T. Kuno, K. Kato, and Y. Takahashi. *An ytterbium quantum gas microscope with narrow-line laser cooling*, New Journal of Physics **18**, 023016 (2016). DOI: 10.1088/1367-2630/18/2/023016.

[74] M. Miranda, R. Inoue, Y. Okuyama, A. Nakamoto, and M. Kozuma. *Site-resolved imaging of ytterbium atoms in a two-dimensional optical lattice*, Physical Review A **91**, 063414 (2015). DOI: 10.1103/PhysRevA.91.063414.

[75] A. A. Michelson and E. W. Morley. *On the relative motion of the Earth and the luminiferous ether*, American Journal of Science **s3-34**, 333–345 (1887). DOI: 10.2475/ajs.s3-34.203.333.

[76] *Two-dimensional phase unwrapping: theory, algorithms, and software*. Wiley, 1998. ISBN: 978-0-471-24935-1.

Acknowledgements

First of all I would like to thank **Immanuel Bloch** for giving me the wonderful opportunity to be part of his group and providing us with this exceptional research environment at the Max Planck Institut of Quantum Optics. It is something, that we way too often take for granted and do not appreciate as much as we should.

Secondly, I would like to express my gratitude to **Frank Pollmann**, who agreed on being my official supervisor from the Technical University Munich. It is never straight forward to find support from faculty for outgoing projects. I would like to especially thank you for your easy to deal with nature on all of the administrative issues, especially during the pandemic.

I want to especially acknowledge my principal investigator **Sebastian Blatt**. You taught me many things, not only about physics but also about computer science and data analysis. Thank you for also teaching me how to structure projects and how to split seemingly impossible tasks into little manageable pieces. You really made me fit for graduate school.

My special thank goes to **Valentin Klüsener** for being my partner in crime on many of the endeavors described in this thesis. The fun we had in the lab kept me motivated throughout this year. Also thank you for all the discussions we had about physics. You showed me many connections between different topics that I would otherwise never be aware of.

Another big thank you goes to **Jan Trautmann** for solving all my ”non-issues” and teaching me proper coding and data analysis. It was always entertaining and a welcome change when we did basic craftsmanship together.

Our by now senior PhD student **Annie Park** is someone who I owe a lot more thank yous than I can write down here. You were always there when we got stuck .... again even if you were busy fixing our main experiment. I wish you only the best for your upcoming Post-Doc.

My thanks also go to **André Heinz** for his support with aligning the interferometer and for many interesting discussions about lifestyle and how science is and should be done.

Further I like to express my gratitude to **Neven Santic**. Your expertise with frequency combs and the construction of very stable lasers contributed significantly to this project. Also, thank you for many Mathematica notebooks for creating beautiful figures for this

thesis. Good luck with your new lab back home in Croatia.

Another great thank you goes to my fellow master student, **Eva Casotti**. We kept us motivated during the hard times by sharing our concerns and problems. It was always nice to have someone one the same level to talk to.

I would also like to thank **Anton Maier** a lot. Your technical support on everything regarding mechanical design, especially during construction of the microscope mount is part of why MPQ is such a good place for doing experimental physics.

At the same time I want to thank **Karsten Förster** for his support on the electronic side. I would like to particularly acknowledge your patience in explaining basic circuit design to someone who had no experience to speak of in electronics.

Also another big thank you to **Kristina Schuld** and **Doreen Seidl** for their helpful assistance regard administrative concerns.

Zu guter Letzt möchte ich diese Gelegenheit nutzen um mich vorallem bei meiner **Familie** für die entlose Geduld und bedingunglose Unterstützung zu bedanken. Ohne euch wäre all Dies nicht möglich gewesen.

Erklärung

Ich versichere hiermit, dass ich die von mir eingereichte Abschlussarbeit selbstständig verfasst und keine anderen als die angegebenen Quellen und Hilfsmittel benutzt habe.

München, den 15. Dezember 2020